

Sea-ice topographic surveying using Structure-from-Motion photogrammetry conducted from small UAVs

by

Martin St-Amant

A thesis submitted to the Faculty of Graduate and Postdoctoral Affairs in partial fulfillment of the requirements for the degree of
Master of Science

in

Geography

Carleton University
Ottawa, Ontario

© 2018, Martin St-Amant

Abstract

The heterogenous topography of sea-ice is difficult to measure, monitor and predict. Recent technological improvements have enabled the development of structure from motion (SfM) surveying using small unmanned aerial vehicles (sUAVs). sUAV-SfM surveying was evaluated as a low-cost technique of obtaining sea-ice topography. Field data collection was conducted in Frobisher Bay and consisted of several sUAV-SfM surveys at the sub-kilometre- and kilometre-level spatial scale. RMSE values of 87 mm and 80 mm were obtained, respectively, for comparing the sUAV-SfM to a reference dataset and for comparing among individual sUAV-SfM surveys. The technique was successful at detecting, measuring and visualizing sea-ice features, such as pressure ridges. When compared to established techniques at similar spatial scales, sUAV-SfM was generally superior in terms of cost, simplicity, flexibility and ground resolution, but it suffered from low reliability due to accuracy issues with low-cost GPS receivers.

Acknowledgements

I'll be forever grateful for all the support I've received from multiple people and organizations throughout this thesis.

Thanks to my supervisors, Derek Mueller and Adrienne Tivy, who proposed the unexpectedly rich subject of sea-ice as a target to explore SfM, for your guidance during the preparation and post-processing, and for your invaluable support during the thesis writing. Thanks to Adam Garbo, since without your tremendous help, your UAV and fieldwork expertise and the hundreds of hours you've dedicated, both this thesis and the UAV would have had never taken-off. Thanks to the Nunavut Research Institute and their wonderful staff (Ted Irniq, Rick Armstrong, Jamal Shirley and countless others) for the fieldwork support provided and the flexibility doing so during my stay in Iqaluit. I owe a special thanks to Ted for his willingness to share his Inuit knowledge and culture. Thanks to Nick Brown for your reviewing efforts and great editing skills. Thanks to the Northern Scientific Training Program, the Canadian Foundation for Innovation, the Ontario Research Fund, and the Natural Sciences and Engineering Council of Canada for equipment and fieldwork funding. Thanks to the Canadian Armed Forces and the Mapping and Charting Establishment for sponsoring my post-graduate studies, which enabled the completion of this thesis. Thanks to fellow students and colleagues within

the *Geography and Environmental Studies Department* and the *Water and Ice Research Laboratory* for various levels of help and support.

Finalemment, un énorme merci à ma famille, Étienne, Ariane, et particulièrement à Mirian, pour votre support, vos encouragements et votre compréhension pendant les trop nombreuses heures que j'ai consacré à cette thèse. J'en suis profondément reconnaissant.

Table of Contents

Abstract.....	ii
Acknowledgements.....	iii
Table of Contents.....	v
List of Tables	vii
List of Figures.....	viii
List of Appendices	ix
1 Introduction.....	1
1.1 Research aim and objectives	3
1.2 Approach and expected outcomes.....	4
1.3 Thesis structure	6
2 Context.....	7
2.1 Sea-ice.....	7
2.2 Established techniques for sea-ice surveying.....	10
2.2.1 Relationship between freeboard, draft and full thickness surveys.....	10
2.2.2 Measurement concepts and examples of established surveying techniques	11
2.2.3 Current disadvantages of established surveying techniques	14
2.2.4 Potential advantages of sUAV-SfM.....	16
2.3 Structure from motion (SfM)	16
2.3.1 Structure from motion workflow	17
2.3.1.1 Image acquisition	17
2.3.1.2 Scale and georeference.....	18
2.3.1.3 Keypoint identification.....	19
2.3.1.4 Bundle Adjustment	19
2.3.1.5 Dense point cloud generation.....	20
2.3.1.6 Visualization	20
2.3.2 Assessing data quality of SfM surveys	21
2.3.3 GPS.....	22
2.4 UAVs	25
3 Methods	28
3.1 Field Methods.....	28
3.1.1 Research site	28
3.1.2 SfM surveys	29
3.1.3 Ground surveys	32
3.1.4 Experiment design	32
3.2 SfM data analysis	34
3.2.1 Data preparation.....	34
3.2.2 Structure from motion and point cloud preparation.....	36
3.2.3 Accuracy, precision and repeatability.....	39
3.2.3.1 Accuracy and precision	40
3.2.3.2 Repeatability	41
3.2.4 Mapping sea-ice topography.....	43
3.3 Operational performance.....	45
3.3.1 Reliability	45
3.3.2 Surveying and processing speed.....	48
3.3.3 Simplicity.....	48
3.3.4 Costs	48
4 Results.....	50

4.1	SfM survey quality	52
4.1.1	Accuracy and precision.....	52
4.1.2	Repeatability	55
4.2	Mapping sea-ice topography	59
4.2.1	Elevation maps.....	59
4.2.2	Maps of sea-ice changes	64
4.2.3	Orthophotos and transects.....	69
4.3	Operational performance of sUAV-SfM.....	73
4.3.1	Reliability	73
4.3.2	Surveying and processing speed	81
4.3.3	Simplicity.....	82
4.3.4	Costs	84
5	Discussion.....	86
5.1	Accuracy, precision and repeatability	86
5.1.1	Accuracy and precision.....	86
5.1.2	Repeatability	90
5.2	Sea-ice topography: maps, orthophotos and transects.....	91
5.3	Operational performance.....	93
5.4	Comparison to existing techniques	96
5.5	Possible improvements to the technique	104
5.6	Practical applications	107
6	Conclusion	110
7	References.....	115

List of Tables

Table 2.1.	Selection of frequently used sea-ice surveying projects and techniques.....	13
Table 3.1.	Survey parameters and environmental conditions.....	33
Table 4.1.	Details of SfM surveys 11, 12 and 13 conducted on May 13th, 2017.....	51
Table 4.2.	Z_{dist} statistics for surveys 11 to 13.....	54
Table 4.3.	Sources of vertical error due to instrumental measurements for the ground survey and sUAV-SfM surveys.....	55
Table 4.4.	Z_{dist} vector field distribution between unregistered core point clouds.....	57
Table 4.5.	Z_{dist} vector field distribution between post-SfM registered core point clouds.....	58
Table 4.6.	Instrument error for a sUAV-SfM survey-to-sUAV-SfM survey calculations...	58
Table 4.7.	Ice GPS2 reliability.....	76
Table 4.8.	UAV GPS1 reliability.....	78
Table 4.9.	Timestamping reliability of UAV GPS1.....	79
Table 4.10.	Equipment and data reliability summary.....	80
Table 4.11.	SfM survey resolution indicators.....	81
Table 4.12.	Surveying and processing speeds.....	82
Table 4.13.	Cost estimate for the equipment, training and license required to conduct and process sUAV-SfM surveys.....	85
Table 5.1.	Comparison of the characteristics of platforms used for sea-ice surveys.....	102

List of Figures

Figure 2.1.	Cross-sectional schematic of a pressure ridge formation.....	9
Figure 3.1.	Overview of the research site and experimental setup.....	31
Figure 3.2.	Visual representation of the Multiscale Model to Model Cloud Compare (M3C2) algorithm used to average and decimate the point cloud.....	38
Figure 3.3.	Schematic representing the point cloud workflow with a fictional raw point cloud.....	39
Figure 3.4.	Schematic of the sources of vertical error due to instruments for the ground survey and the sUAV-SfM surveys.....	43
Figure 4.1.	SfM output examples.....	52
Figure 4.2.	Histograms of the elevation difference (Z_{dist}) between SfM Surveys 11, 12 and 13 core point clouds and the ground survey points.....	54
Figure 4.3.	SfM survey to SfM survey Z_{dist} scalar field distribution for (a) unregistered and (b) post-SfM registered point clouds.....	57
Figure 4.4.	Elevation maps of the cropped core point clouds of SfM surveys 11, 12 and 13.	60
Figure 4.5.	Elevation map close-up from SfM survey 11.....	61
Figure 4.6.	Elevation map of the entire length of the ridge for SfM survey 14.....	63
Figure 4.7.	Z_{dist} between SfM survey pairs.....	66
Figure 4.8.	Z_{dist} map of SfM Survey 12-13.....	67
Figure 4.9.	Association between point cloud repeatability error and SfM images boundaries.....	68
Figure 4.10.	Orthophoto of the sea-ice surface from SfM Survey 11.....	70
Figure 4.11.	Elevation along a transect in the rubble ice area for SfM Surveys 11, 12 and 13.....	72
Figure 4.12.	Ice GPS1 and 2 reliability for sea-level elevation measurement for the 10 th , 11 th , 13 th and 16 th May.....	75
Figure 4.13.	Camera location error report from <i>Agisoft Photoscan</i> for SfM Survey 3 and SfM Survey 13.	77
Figure 5.1.	Spatial distribution of the ground survey compared with a cropped core point cloud area and the SfM image boundaries grid.....	88
Figure 5.2.	Example of the heterogeneous spatial distribution of points from a UAV-borne lidar survey.....	103

List of Appendices

Appendix A.	Workflow diagrams.....	126
Appendix B.	Custom R Script to correct UAV GPS1 positions.....	128

1 Introduction

Sea-ice is a very dynamic (Weeks, 2010) and complex (Bergan et al., 2010) material. Thermal and mechanical forces can converge, diverge, deform, move, generate and thaw sea-ice (Bergan et al., 2010), producing a heterogenous topography that is difficult to measure, monitor and predict (Choi et al., 2015; Haugen et al., 2011; Strub-Klein and Sudom, 2012; Zakharov et al., 2014). Sea-ice topographical measurements are useful since sea-ice topography influences the wind drag (Steiner et al., 1999), the above ice movements (Dammann et al., 2018) and can be used to estimate sea-ice thickness (Doble et al., 2011), an important sea-ice feature of importance for humans and the environment. For example, sea-ice thickness affects the risk to marine traffic (Weeks, 2010) as well as its effectiveness as a climate regulator (Eicken et al., 2009). One of the most common sea-ice features is the pressure ridge (Tan et al., 2016), a thin and long ice relief structure responsible for the thickest sections of sea-ice (Weeks, 2010). Pressure ridges are difficult to survey remotely (Strub-Klein and Sudom, 2012).

Despite the importance of sea ice topography in understanding marine geohazards and climate regulation, measurement and monitoring efforts are limited by the techniques used to collect data. Current sea-ice topography surveying techniques, such as land surveys, aerial lidar or satellite imagery, all offer trade-offs with respect to cost, speed, precision, and ease-of-use. An improved technique would facilitate the generation and access to accurate sea-ice topography data.

Structure from motion (SfM) is a progressing image-processing technique that produces digital 3D models from a series of overlapping 2D images. SfM can be conducted using images from consumer-grade cameras (Ingwer et al., 2015; Natan et al., 2014) and can be processed with affordable computers and software (Mlambo et al., 2017). Combined with increasingly popular small unmanned aerial vehicle (UAV) platforms, SfM has been demonstrated to be a valuable low-cost alternative to traditional remote-sensing surveys which typically required manned aircraft and expensive equipment (Ely et al., 2016; Uysal et al., 2015). The combination of small UAV (sUAV) with SfM post-processing may offer an improved technique of sea-ice topographic surveying.

The sea-ice environment presents unique challenges for sUAV-SfM (Dammann et al., 2018). Factors such as cold weather reduces the sUAV battery life and therefore sUAV range, or non-stationary targets and low-contrast surfaces, such as snow and ice, impede the ability of the SfM algorithms to create a 3D model. These are issues that require mitigation if successful surveys are to be achieved. However, the technique is likely feasible based on similar techniques successfully tested by the cryospheric research community.

Previous research has successfully used SfM surveys in cold regions despite these challenges. This has been demonstrated, for example, by manned aircraft-borne SfM surveys of low-contrast surfaces (snow) by Nolan et al. (2015) or of non-stationary targets (ice islands) by Crawford et al. (2018) and by successful sUAV-SfM surveys of

glaciers by Ryan et al. (2015). Some uses of SfM for surveys of sea-ice have been reported from both manned aircraft (Steer, 2017) and sUAVs (Eltoft et al., 2015; Lean, 2012; Saiset et al., 2015; Saiset, 2015). However, none of the studies using sUAV-SfM surveys of sea-ice were dedicated to the extensive testing of the technique. Consequently, the potential of sUAV-SfM surveys for mapping sea-ice has not yet been fully evaluated.

1.1 Research aim and objectives

The success of SfM surveys is determined by the specific combination of the environmental conditions, image capture parameters and equipment quality. However, unless these parameters are specifically tested, there is only a limited ability to predetermine data quality in future surveys (Smith et al., 2016). As the accuracy, precision and repeatability of sUAV-SfM over sea-ice have not been formally assessed (Saiset et al., 2015; Saiset, 2015), the aim of this thesis is to determine the quality of sUAV-SfM topographical surveys of sea-ice, as well as the associated challenges and outcomes of processing and collecting the data at a relatively low cost. This translates into the following overarching research question: Can low-cost sUAV-SfM surveys be used to measure sea-ice topography with satisfactory accuracy, precision, repeatability, spatial resolution, spatial scale, speed, and reliability to be considered a viable mapping technique? In this study, three specific objectives were met to answer this question:

Objective 1: Quantify the accuracy, precision and repeatability of sUAV-SfM surveys over sea-ice;

Objective 2: Use single and multiple sUAV-SfM surveys to detect, measure and visualize sea-ice features and changes, especially for pressure ridges; and

Objective 3: Analyze the advantages and disadvantages of sUAV-SfM as a tool to study sea-ice topography and compare it to other more established techniques.

1.2 Approach and expected outcomes

To achieve the thesis objectives, multiple sUAV-SfM surveys and a reference ground survey of sea-ice were conducted. The fieldwork and data-processing methods were adapted to mitigate some of the difficulties associated with sea-ice surveying. Specifically, GPS receivers were set up on the ice surface to record and compensate for sea-ice movements. In addition, the contrast of the images was digitally enhanced to provide the best-possible match between photos. After the sUAV-SfM surveys were nominally processed by SfM algorithms, the following approaches were used to achieve each objective.

To determine the accuracy, precision and repeatability of the measurements, point cloud outputs from individual sUAV-SfM surveys were compared to a reference ground survey and between each other. Statistical tests were performed to check whether the quality of measurements was representative of typical SfM surveys. This allowed the technique to be compared to established techniques.

The detection, measurement and visualisation of sea-ice features and changes was accomplished through point cloud operations and orthophoto analysis. The results provided an indication of the spatial resolution and the spatial scale at which the technique can resolve sea-ice features and changes.

For the advantages and disadvantages analysis, the operational performance and the cost of the technique were assessed. Factors such as the equipment and data reliability, point cloud density, surveying and processing speeds, and equipment costs were all considered. Using all the results obtained throughout the thesis, the performance of sUAV-SfM surveys was evaluated. Finally, the potential of this technique to outperform established sea-ice surveying techniques is discussed and possible gaps in surveying capability that may be filled by the technique are identified.

If the challenges of conducting sUAV-SfM surveys in cold environments can be overcome or mitigated, the technique may become the first choice for low-cost topographical surveys of sea-ice at sub-kilometre to kilometre spatial scales (Dammann et al., 2018). Such a development would also advance the state-of-the art for sUAV-SfM surveys, where guidelines currently recommend avoiding target movement, low image contrast and cold environments (Fonstad et al., 2013; Laliberté, 2016; Smith et al., 2016; Westoby et al., 2012). The results of this thesis are expected to be relevant to a large audience of potential users including sea-ice scientists and engineers, icebreaker operators and local governments in Arctic communities. Low-complexity and low-cost topographical surveys of sea-ice are of interest to many stakeholders in order to, among

other things, estimate the ice thickness (Lee et al., 2016), calculate the strength of pressure ridges (Høyland, 2002), optimize route finding for ships (Dammann et al., 2018), validate remote sensing data (Hvidegaard et al., 2015) or validate sea-ice models (Martin, 2006).

1.3 Thesis structure

A traditional format is followed for this thesis. Chapter 2 provides background information on sea-ice and the sea-ice surveying techniques used in the research. The fieldwork, data collection, and data-processing steps are described in Chapter 3 and the results are presented in Chapter 4. An analysis of the results, a comparative evaluation of sUAV-SfM against established sea-ice surveying techniques and possible improvement and outcomes to the technique are discussed in Chapter 5. Finally, Chapter 6 presents the main conclusions and provides direction for subsequent work on the subject.

2 Context

2.1 Sea-ice

Sea-ice is an important feature of polar and sub-polar seas. It is an ephemeral, mobile and ever-changing phenomenon that requires frequent and/or quick observation to understand, model and predict its physics and dynamics. Sea-ice covers on a yearly average $2.5 \times 10^7 \text{ km}^2$ – equivalent to 7% of the world's ocean surface (NSIDC, 2018). This layer acts as a physical and thermal barrier between the cold polar atmosphere and the relatively warm sea water, and has a significant influence on both local and global climates (Weeks, 2010). Many human activities are affected by sea-ice, including recreational ice fishing, maritime transport, cryospheric research and daily life for residents of Arctic coastal communities. Far from being limited to northern residents or visitors, sea-ice has far reaching geopolitical implications, exemplified by the climate change debate (Weeks, 2010) and the sovereignty controversy of an emerging ice-free Northwest Passage (Charron, 2005).

The density contrast between the sea-ice ($\sim 917 \text{ kg m}^{-3}$) and sea-water ($\sim 1026 \text{ kg m}^{-3}$) (Herzfeld et al., 2015) causes a small portion of the sea-ice to float above the surface of the water (the height of which is measured by the freeboard) while the remainder of the ice remains submerged (the depth of this is indicated by the ice draft). Assuming hydrostatic equilibrium and a constant ratio between freeboard and draft, sea ice thickness can be estimated by measuring the freeboard (Eicken et al., 2009). However, the bulk density of sea ice can vary significantly due to snow cover or to

changes in sea-ice temperature, salinity and porosity (Weeks, 2010) so the accuracy of this technique is somewhat limited.

Thermal forces, mostly determined by the oceanic and atmospheric heat fluxes (Thorndike et al., 1975) and mechanical forces, such as winds and currents causing nonuniform movements of the ice (Thorndike et al., 1975; Weeks, 2010), defines sea-ice topography as they influence the thickness of sea-ice; thermal forces are responsible for the creation and elimination of sea-ice through freezing and melting, while mechanical forces are responsible for sea-ice deformation. Both thermal and mechanical forces typically act on the ice simultaneously which makes it difficult to model the evolution of sea ice cover over time (Thorndike et al., 1975). While thermal forces can generate relatively thick areas of undeformed (level) sea-ice, mechanical forces are responsible for generating the thickest ice through deformation (Thorndike et al., 1975; Williams et al., 2015).

Sea-ice deformation occurs when an applied force is greater than the bearing capacity, causing single or repeated structural failures within the ice (Weeks, 2010). Multiple types of sea-ice deformation exist. Pressure ridges, are the most common type of deformation (Tan et al., 2016) and are relevant to this thesis. Ridges account for 40% (Leppäranta, 2011) to 50% (Xin Miao et al., 2016) of the total sea-ice volume in the Arctic. They commonly form at the edge of ice floes in response to convergence (Weeks 2010); as pressure builds up, the uneven floe edge geometries will tend to force one ice floe below the other. If this pressure overcomes the sea-ice strength, sections of the

weaker ice floes are broken-off, rotated, and pushed either over or under the opposing floe (Figure 2.1). This process will repeat itself if the compressive force between the ice floes remains stronger than their structural capacity (Weeks, 2010). As the ridge forms, pieces of ice will accumulate in a rubble pile located above (the sail) or below (the keel) the waterline (Parmerter and Coon, 1972). Ridges are of great scientific and economic interest (Weeks, 2010). They can become obstacles to surface and maritime transport (Leppäranta and Hakala, 1992), gouge the sea-floor (Barnes et al., 1987) and influence the longevity of sea-ice (Rigor and Wallace, 2004).

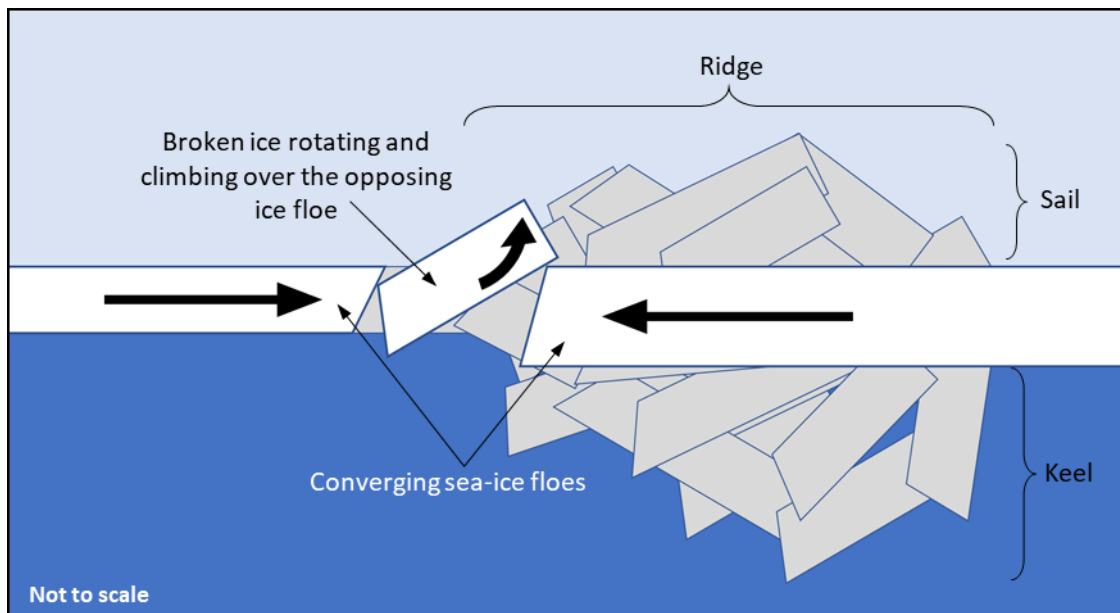


Figure 2.1. Cross-sectional schematic of a pressure ridge formation.

Two converging sea-ice floes forced one against the other. The built-up pressure forces one floe above the other, until a piece breaks off. The converging floes push and rotate broken pieces either above or below the water, forming either a sail or a keel. The process is repeated as long as the floe convergence force is stronger than the structural capacity of the weaker ice floe.

Sketch adapted from figures by Weeks (2010).

2.2 Established techniques for sea-ice surveying

2.2.1 Relationship between freeboard, draft and full thickness surveys

No ideal sea-ice surveying technique currently exists to measure ice topography, thickness or volume (Leppäranta, 2011). sUAV-SfM surveys of sea-ice can provide direct measurements of the sea-ice topography. Sea-ice topography is defined here as both the configuration of the sea-ice surface relief and the relative elevation and position of sea-ice features above sea level (freeboard elevation). As stated above, topography can be used to indirectly estimate sea ice thickness and volume. For context, sUAV-SfM is compared with established surveying techniques used to either directly or indirectly estimate sea ice volume and thickness. Indirect estimates rely on the relationships between the sea-ice freeboard, the draft, the total sea-ice thickness and the sea-ice volume, and have a higher degree of uncertainty (Doble et al., 2011; Eicken et al., 2009; Melling et al., 1995). Despite these uncertainties, indirect estimates may be preferred to direct surveys based on the advantages and disadvantages of each technique. For example, while drilling through the ice is considered to be the most precise ice thickness measurement technique (Leppäranta, 2011), ice thickness estimates from airborne lidar (a topographical surveying technique) are preferable for surveys of large spatial scales. As such, it is valuable to also compare sUAV-SfM to established draft and full-thickness surveying techniques (Table 2.1). The established surveying techniques are currently used for multiple purposes, such as navigation (Weeks, 2010), structural engineering impacts of sea-ice (Melling et al., 1995) and modelling of sea-ice topography impact on atmospheric drag (Castellani et al., 2014; Petty et al., 2017).

2.2.2 Measurement concepts and examples of established surveying techniques

Draft can be measured (Doble et al., 2011) with upward looking sonars (ULS) (Strub-Klein and Sudom, 2012), mounted on military submarines or attached to the sea floor (Ekeberg et al., 2015). Full sea-ice thickness can be calculated by adding the draft to the freeboard. Drilling through the ice enables direct measurements to be made of the full thickness (draft + freeboard) with simple instruments (Eicken et al., 2009).

Electromagnetic surveying, such as the Airborne Electromagnetic Method (AEM), uses electromagnetic fields, where the return signal strength from the conductive sea-water can be used to measure the average draft or ice thickness (Leppäranta, 2011) by subtracting it from either the sea-level or the freeboard (Haas, 1998; Haas et al., 2009; Multala et al., 1996). Ground penetrating radars (GPR) works similarly, except that the return signals from radar pulses are used to detect the depth of the sea-ice to sea-water interface (Holt et al., 2009). Thermal imagery can also be used under cold air conditions to estimate the ice thickness, as thicker ice will better insulate the warmer water (Light et al., 2012), and therefore will emit less thermal radiation than thinner ice.

Topographical surveying techniques are the most commonly used sea-ice surveying techniques, especially for sea-ice thickness measurements, and are conducted either from the ice surface, from aerial platforms or from space. These include: surface surveys, where traditional surveying equipment such as theodolites, levels or GPS receivers are used (Strub-Klein and Sudom, 2012), stereophotogrammetry, where pairs of overlapping images are used to extract topographical data (Divine et al., 2016), lidar, where the flight time of laser pulses is used to measure distances between the sensors and

the sea-ice (or snow) surface (Eicken et al., 2009), and radar ranging (including synthetic aperture radar – SAR), where microwaves are used to penetrate air, clouds or snow, with return signal timing providing freeboard elevation (Eicken et al., 2009). The *National Aeronautics and Space Administration's* (NASA) *ICESat* (2003-2010) and *ICESat-2* (2018 planned launch), and *European Space Agency's* (ESA) *CryoSat-2* are dedicated ice thickness measurement satellites, with lidar used for the NASA satellites and SAR for ESA. Each space agency also conducted extensive airborne and ground measurement campaigns linked to their satellite missions, *Operation IceBridge* (Zell, 2017a) and *CryoVEx* Program (ESA, 2014) respectively. These efforts are the most extensive sea-ice thickness measurement programs ever conducted (Zell, 2017a), and they mostly used radar and lidar for ice thickness collection (Table 2.1). In addition, interferometric SAR (InSAR) measurements can also be made from multiple SAR products, where the interferometric measurements from the SAR return signal can be used to survey sea-ice surface topography (Dierking et al., 2017) or to measure topographical changes (Berg et al., 2015).

Table 2.1. Selection of frequently used sea-ice surveying projects and techniques.

This non-exhaustive list combines the available data from a variety of ice-thickness surveying and research projects. Blank spaces indicate unavailable data.

Technique	Instrument name	Measure			Platform/location					Capture parameters					Capture rate		Production rate		Data quality		References		
		Draft	Freeboard	Total thickness	Sea-floor	Underwater vehicle	Surface	Ship	sUAV	Large aircrafts*	Orbit	Sensor resolution	Sensor altitude (m)	FoV (m)	GSD (m)	Footprint (m)	Images per second	Points per second	Area per hour (km ²)	Points per hour		Precision (m)	Qualitative
ULS	Ice-profiling sonar	X			X						20	-50	40		1	1/30		1800		0.001	Good	a c	
	ASL Environmental Sciences Ice Profiler, IPS 5	X			X						1	-18	0.5		0.5		1	3600			Good	a d	
Drilling	Traditionnal	X	X	X		X					1	0	0		0			5 - 20			Excellent	a b	
GPR	Unnamed		X			X					1	0	0		2.5		5000				Poor	a e	
Ground Surveying	Traditionnal		X			X					1	0	0		0			30 - 120			Good	a b	
Stereophotogrammetry	ICE stereocamera system		X					X			2.1 x 10 ⁷	40	60	0.01	0.01	1	2.1 x 10 ⁷	2	7.6 x 10 ¹⁰			f	
Electromagnetic	Geonics EM31		X			X					1	4			0.4		50	0.02	1.8 x 10 ⁵			Good	a g
	AWI EM bird		X					X			1	20					10	3.6 x 10 ⁴			Good	a h	
	Unnamed		X					X			1	60		12.5	100		4	18	1.4 x 10 ⁴	0.2		Good	a i
	Ice Pic		X			X		X			1	22		5	50		10	9	3.6 x 10 ⁴			Good	a j
	Geonics EM31		X			X					1	0									0.2		Good
Thermal and infrared	IceBridge - Airborne Topographic Mapper - FLIR A655sc		X					X			3.1 x 10 ⁵	800					50		5.5 x 10 ¹⁰			Fair	a l
	IceBridge - Airborne Topographic Mapper - FLIR A325sc		X					X			7.7 x 10 ⁴	800										Fair	a l
	IceBridge - Airborne Topographic Mapper - KT-19 Pyrometer		X					X				800	28 m					20				Fair	a l
Lidar	IceBridge - Airborne Topographic Mapper (ATM)		X					X			1	500	300	5	2		5000	200	7.2 x 10 ⁴	0.1		Fair	a l m n
	IceBridge - Land, Vegetation and Ice Sensor (LVIS)		X					X			1	10000	2000		15		1000	1400	3.6 x 10 ⁶	0.06		Fair	a m o
	IceBridge - UTIG LiDARs		X					X			1		400				2.0 x 10 ⁶	300	7.2 x 10 ⁹			Fair	a p
	IceBridge - UAF Airborne Scanning LiDAR		X					X			1	500	250				1.0 x 10 ⁴	175	3.6 x 10 ⁷	0.08		Fair	a q
	ICESat - Geoscience Laser Altimeter System		X						X		1	6.0 x 10 ⁵	50	172	60		40	400	1.4 x 10 ⁵	0.02		Fair	a n r
	ICESat-2 - Advanced Topographic Laser Altimeter System		X						X		1	5.0 x 10 ⁵	45	0.7	17		1.0 x 10 ⁴	2500	3.6 x 10 ⁷	0.1		Fair	a n s
	CryoVEx - Airborne Laser Scanner (ALS)		X						X		1	500	300				1.0 x 10 ⁴					Fair	a t
Radar	IceBridge - CReSIS's snow radar		X					X															u
	IceBridge - Ku-Band Radar Altimeter		X					X															v
SAR	CryoSat-2 - Synthetic Aperture Interferometric Radar Altimeter		X					X			1	7.2 x 10 ⁵		250	250		2.0 x 10 ⁴	3.8 x 10 ⁵	7.2 x 10 ⁷			Poor	a
InSAR	CryoVEx - Airborne SAR Interferometric Radar System		X					X			1	300			3 - 10			200					t
	CryoSat-2 - Synthetic Aperture Interferometric Radar Altimeter		X					X			1	7.2 x 10 ⁵	300				2.0 x 10 ⁴		7.2 x 10 ⁷				w
	Cosmos-SkyMed		X					X				7.5 x 10 ⁵	4.0 x 10 ⁴	3									x
	TanDEM-X		X					X				7.5 x 10 ⁵			12						0.5		y

*Large aircraft refers to manned aircraft and UAVs larger than sUAVs

Sources: a: Leppäranta, 2011, b: Strub-Klein and Sudom, 2012, c: Melling et al., 1995, d: Obert and Brown, 2011, e: Holt et al., 2009, f: Divine et al., 2016, g: Haas, 1998, h: Haas et al., 2009, i: Multala et al., 1996, j: Peterson et al., 2008, k: Worby et al., 1999, l: NASA, 2017, m: Yi et al., 2015, n: Farrell et al., 2011, o: NASA, 2018a, p: Zell, 2017b, q: Larsen, n.d., r: Zwally, 2016, s: NASA, 2018b, t: Di Bella et al., 2018, u: Zell, 2017c, v: Zell, 2017d, w: ESA, 2013, x: Berg et al., 2015 and y: Dierking et al., 2017.

2.2.3 Current disadvantages of established surveying techniques

For each of the previously described measurement techniques, there are trade-offs between cost, spatial resolution, spatial scale, speed, accuracy, dependability, flexibility and complexity. Some of the main disadvantages of current sea-ice surveying techniques are as follows:

Most techniques are limited to a single measurement per capture cycle per sensor (single pixel resolution each time the sensor is used). Unless the ground sampling distance (GSD – distance between pixel centres) is equal to the ground resolution (or footprint size) of the pixel, this will either cause measurement gaps (if the footprint is smaller than GSD) or smoothing (if GSD is smaller than the footprint) of the topography. Most of these techniques have footprints larger than the GSD, which will underestimate surface roughness and ridge elevations (Farrell et al., 2011), and are sub-optimal considering small-scale ice surface characteristics are important for a better understanding of the larger-scale properties of sea-ice (Vihma, 2014). For non-scanning, single pixel resolution surveying techniques requiring the displacement of the sensor for each measurement, such as ULS, drilling, GPR, ground surveying and electromagnetic techniques, the limited dimensionality (linear surveying) and spatial resolution (determined by the sensor's speed of travel) will limit the number of survey points captured.

Bottom mounted, upward-looking sonars depend on the movement of sea-ice for one-dimensional ice surveys (Melling et al., 1995) or require expensive underwater

vehicles if a specific 2D area must be surveyed. Drilling and ground surveys are labour intensive and slow (Leppäranta, 2011). Stereophotogrammetry instruments are large and require manned aircraft as platforms (Divine et al., 2016). Airborne electromagnetic surveys are limited to a maximum flight elevation above sea-level (30 to 60 m, depending on the instrument set-up and ice conditions) due to the rapid degradation of the signal-to-noise ratio (Haas et al., 2009; Multala et al., 1996). This flight elevation limit would be ideal missions for sUAVs if the payload (over one hundred kg) weighted a hundred times less. Thermal and infrared surveying accuracies degrade with thicker ice (Leppäranta, 2011) and are negatively affected by snow-cover (Light et al., 2012). The large size of most scanning lidar systems for sea-ice surveying require manned aircraft or large UAVs (NASA, 2017), while sUAV-lidar generally suffers from poor accuracy (Chiang et al., 2017). Satellite-based SAR signals have large ground footprints, and InSAR requires specific orbital conditions for the satellites, minimal ice movement and complicated data manipulation (Berg et al., 2015; Dierking et al., 2017).

Most remote-sensing surveys also require precise real-time sea-level elevation. If no ground instruments are available to provide this data, these surveying techniques have to rely on sea-level modelling or remote measurements of sea-level from leads (a large sea-ice fracture with open sea-water), adding complexity and uncertainty for these measurements (Wernecke and Kaleschke, 2015). Several of these instruments are highly specialized and are often custom-made, which incurs high-costs. For remote-sensing platforms, satellite-based instruments incur extremely high capital costs, while manned-aircraft often have high operation costs.

2.2.4 Potential advantages of sUAV-SfM

sUAV-SfM has the potential to alleviate some of these issues by providing sea-ice topographical surveying capability up to the kilometre-level spatial scale with lower capital investment (UAV and instruments) and operation costs, location independence (as opposed to inflexible satellite orbits or fixed ULS), full surface coverage without gaps or averaging (since GSD is equal to ground resolution), centimetre-level ground resolution, and area surveying (as opposed to linear surveying). However, these improvements are speculative and require a rigorous comparison with existing techniques, especially those with similar outputs, such as stereophotogrammetry, lidar and InSAR.

2.3 Structure from motion (SfM)

SfM is a photogrammetric topography surveying technique used to generate 3D models from 2D imagery. SfM began to develop as a geoscientific technique in the late 2000's. Even as late as 2012, it was still defined as a new revolutionary tool for geoscience applications (Westoby et al., 2012). SfM requires a set of overlapping images taken from different perspectives. Every surface for which a 3D model is desired must be photographed from a minimum of three different angles, and a continuous overlap must be maintained between photos (Smith et al., 2016). The accuracy of SfM is equivalent to other techniques, such as traditional photogrammetry, but surveys can be conducted at a fraction of the cost and complexity (Ely et al., 2016; Thomson and Copland, 2016; Uysal et al., 2015). At the most rudimentary level, SfM can be conducted by a non-specialized user equipped only with a modern smartphone (Micheletti et al., 2015). This increased flexibility and accessibility is key to understanding the appeal of SfM. It is increasingly

used for general geoscience surveys on firm land (Brunier et al., 2016; Dietrich, 2016; Ely et al., 2016; Lucieer et al., 2014; Mancini et al., 2013; Smith and Damià, 2015; Westoby et al., 2012) and it is also used for snow-depth surveys (Nolan et al., 2015) and ice island surveys (Crawford et al., 2018). However, it has been rarely used to survey sea-ice, although a few examples can be found (ACUASI, 2015; Dammann et al., 2018; Saiet et al., 2015; Saiet, 2015; Steer, 2017).

2.3.1 Structure from motion workflow

The data acquisition and processing steps for an SfM survey are as follows:

2.3.1.1 Image acquisition

All portions of the study area must be observed with a minimum of three images from different perspectives (Westoby et al., 2012). Additional photographs can be used to enhance optimal scene reconstruction although this comes at the cost of greater effort, longer flight times during the capture phase, and greater computational demands during data-processing (Westoby et al., 2012). The characteristics of the target and the photograph acquisition parameters influences the digital model quality (Westoby et al., 2012), but there is no clear consensus on the precise relationship between the surveying parameters and the results (Smith et al., 2016). The variously cited surveying parameters are as follows:

1. Extrinsic camera parameters (or flight parameters) (Rock et al., 2012; Smith et al., 2016), such as overlap ratio (intersecting area between two photographs along the flight line) and sidelap ratio (intersecting area between two photographs in adjacent flight lines), spatial scale, speed, altitude, attitude and positional accuracy;
2. Intrinsic camera parameters (Smith et al., 2016), such as sensor pitch size (density of pixels on the sensor), spatial resolution, field of view, bit depth and lens distortion. SfM can accommodate lens distortions, common in lower-end cameras, as these distortions will be minimized in further steps, enabling low capturing costs (Mosbrucker et al., 2016); and
3. Environmental parameters (Crawford et al., 2018; Nolan et al., 2015), such as atmosphere transparency, cloud cover, sun angle, sun intensity, ground reflectivity, ground homogeneity and GCPs.

2.3.1.2 Scale and georeference

Scaling and georeferencing is of high importance when SfM is used for geophysical applications as it enables measurements to be made from the 3D model plus the model can be referenced to geographic coordinates (Westoby et al., 2012) if geospatial data are employed. To do so, photos can be geotagged (direct georeferencing) and/or the surveyed target can be marked by ground control points (GCP) with known

coordinates and elevation (indirect georeferencing) (Smith et al., 2016; Turner et al., 2014; Vander Jagt et al., 2015). If the SfM target is in motion, as may be the case with sea-ice, there is added complexity to scaling and georeferencing since each coordinate must be adjusted in relation to a datum fixed to the target.

2.3.1.3 Keypoint identification

On all images, unique features, known as keypoints, common to multiple images, must be identified to enable the bundle adjustment (see the next step below). Low contrast areas, such as snow-covered landscapes may fail to produce keypoints (Lowe, 2004). Keypoints from different images are then compared with scale-, orientation- and perspective-invariant algorithms to compensate for parallax and scale differences between images (Lowe, 2004) and to log similarities. Similar keypoint pairs are then filtered by considering the 3D geometry between all keypoints, and erroneous matches are filtered until the remaining matches are considered accurate within a 95% probability (Smith et al., 2016).

2.3.1.4 Bundle Adjustment

The rough keypoint cloud generated is then geometrically refined through bundle adjustment (Westoby et al., 2012), a relatively complex visual reconstruction refinement algorithm (Triggs et al., 2000). Bundle adjustment is the main step separating SfM from classical photogrammetry techniques (Smith et al., 2016). The keypoint positions, camera positions, lens calibration models, and georeferencing data (if available) are

iteratively refined to determine a jointly optimal three-dimensional structure for the scene (Smith et al., 2016). Once done, the structure is composed of a rough scaled and georeferenced point cloud of matching keypoints interconnected with camera positions and lens calibration parameters (Smith et al., 2016).

2.3.1.5 Dense point cloud generation

Once the general geometry of the scene is resolved, a multi-view stereo image matching algorithm, common to other photogrammetry techniques, is applied. The pixels from all images are projected, and the intersection of these projections is analyzed. When there is a strong enough match between pixels or groups of pixels, a point is generated in a 3D space, generating a dense point cloud (Smith et al., 2016). As with keypoints, low contrast surfaces may generate difficulties at this step (Nolan et al., 2015). Since the conditions for the generation of points is more permissive than those used for keypoint generation, erroneous or inaccurate points will be generated at a greater ratio (Smith et al., 2016). Point cloud manipulation algorithms may be employed to eliminate statistical outliers (Westoby et al., 2012).

2.3.1.6 Visualization

From the final point cloud, further visual representations are possible (Westoby et al., 2012). Surfaces can be created by joining the points with wire meshes and membranes. The original images can then be projected and stitched on the surfaces,

generating photo-realistic 3D models. Finally, the photo-realistic 3D models may be projected on a horizontal surface, generating orthophotos.

2.3.2 Assessing data quality of SfM surveys

The isolation of the error sources from SfM surveys is challenging due to the number of variables that affect the accuracy (Mallalieu et al., 2017). For the outputs, two types of errors can be distinguished: systematic errors (due to referencing, target and camera geometry, and bundle adjustment errors) and local surface quality errors (due to multi-view stereo image matching) (Eltner et al., 2016). Eltner et al. (2016) propose two ways to measure SfM output errors depending on the availability of a secondary dataset.

1. When a reference dataset is available that can be trusted as a standard, the mean error value between the SfM survey and the reference is preferred as a measure of accuracy. Since the positive and negative errors tend to cancel out, an alternative is to use the root-mean-square error (RMSE), or to consider the precision (the variability or statistical distribution of errors). The spatial distribution of the errors must also be considered to better understand the nature of the errors (Eltner et al., 2016); and
2. When secondary, overlapping SfM surveys are available, another measure of precision (repeatability) can be measured by calculating the distance between each SfM dataset (Eltner et al., 2016). To avoid nomenclatural confusion between the different precision measurements, this thesis will refer to the

precision error relative to a reference dataset as *precision* while *repeatability* will be used to describe the inter-SfM survey distance.

The absolute error values for SfM surveys can be converted to scale-independent relative error values through a ratio with the SfM surveying range (the distance between the SfM target and the acquisition sensor). There is a relatively linear relationship between the absolute error and the range to targets (Eltner et al., 2016; Smith and Damià, 2015). Consequently, the relative error can be used to determine if the quality falls within expected margins. RMSE values are typically used for these calculations (instead of the means and variability), and the RMSE:range ratios are typically between 1:625 (Micheletti et al., 2015; Smith and Damià, 2015) and 1:1000 (James M. R. and Robson S., 2012; Mallalieu et al., 2017).

2.3.3 GPS

GPS receivers are commonly used to scale and/or georeference SfM surveys (Crawford et al., 2018; Nolan et al., 2015; Smith et al., 2016). The mean accuracy of consumer-grade, single-frequency (L1), GPS receivers, which uses code (binary signals) pseudorange measurements for triangulation, is about 5 metres (van Diggelen and Enge, 2015). This level of accuracy is insufficient for georeferencing sUAV-SfM surveys of sea-ice topography, which requires sub-metre level accuracies or better.

Several techniques are available to improve the accuracy of GPS measurements to the sub-decimetre level and better (Leick et al., 2015), such as Differential GPS (DGPS),

Real-Time Kinematic (RTK), Post Processing Kinematic (PPK) and Precise Point Positioning (PPP). Among these, PPK and PPP were post-processed techniques used in this thesis. RTK, PPK and PPP usually require commercial-grade GPS receivers since most consumer-grade receivers are not dual-frequency (L1/L2) receivers (mandatory for PPP) and do not record the carrier-phase (mandatory for PPP, RTK and PPK). These techniques also make use of corrected products (explained below)

Carrier-phase measurements uses the phase of the GPS signals, instead of the binary code for distance measurements. This can achieve much higher accuracies than code pseudorange measurements since the fraction of wavelengths from the GPS signal can be measured, instead of the number of full wavelengths between satellite and receiver (ESA, n.d.). A carrier-phase measurement adds the total number of full wavelengths (an integer) and the fractional wavelength (a fraction) (ESA, n.d.) to accurately measure the distance between the satellite and the receiver. The main issue of this measurement method is the difficulty in determining the total number of full wavelengths, known as the *carrier-phase ambiguity* (ESA, n.d.). The complex process used to fix the ambiguity goes beyond the scope of this thesis, but when this ambiguity is solved, the high accuracy positions are said to have a *fix* quality, while unsolved ambiguity positions are said to have a *float* quality, which is of lower accuracy (ESA, n.d.).

Dual-frequency GPS receivers can better model and compensate for GPS signal disturbances, such as the *ionospheric delay*, since both signals are modified by the atmosphere in a slightly different manner (ESA, n.d.), enabling higher accuracies.

However, dual-frequency receivers require more hardware (ESA, n.d.), thus more weight and costs.

Post-processing GPS signals benefits from the availability of corrected products, such as satellite ephemerides, satellite clocks, earth rotation parameters and atmospheric parameters (ESA, n.d.), which are more accurate versions of the data broadcasted to the GPS receiver during data capture. Each of these corrected products is iteratively distributed and re-distributed online with increasing accuracies, with lowest accuracy products available within hours, while the final, highest accuracy products available up to four weeks post-capture (IGS, n.d.).

RTK and PPK are a post-processing technique used to augment the positional accuracy of a roving GPS up to a centimetre-level accuracy receiver by pairing it to an accurately georeferenced base-station GPS receiver (Takasu and Yasuda, 2009). The position of each receiver is processed using carrier-phase measurements and corrected products (if available). Since the base-station coordinates are known to a high accuracy, positional corrections can be used to calculate the rover position to a higher accuracy (Takasu and Yasuda, 2009). The accuracy of RTK/PPK measurements is therefore directly impacted by the accuracy of the base station position. RTK requires constant communication between the base and roving receivers, which is not always practical. PPK can be used when real-time precise positioning is not required (Everett, 2017), which is typically the case for post-processed aerial SfM surveys. Receivers that support

RTK/PPK are either single- or dual-frequency thus the accuracy, weight and costs trade-offs must be considered for low-cost UAV operations.

PPP is a post-processing technique to augment the positional accuracy of a GPS receiver independently from any reference monument. Available globally, it uses the advantages of dual-frequency receivers, carrier-phase measurements and corrected products (ESA, n.d.). In static mode, PPP can provide sub-centimetre position solutions (ESA, n.d.). In areas where survey markers are inaccessible or impracticable, PPP can be used to georeference base stations with high accuracy, from which the roving receiver positions can be calculated accurately with PPK (NRCan, 2013). In order to achieve the highest level of accuracy in static mode, PPP requires long occupation times (Krzan et al., 2017). National Resources Canada (NRCan) provides an online tool, called CSRS-PPP, to compute PPP solutions from RINEX files¹ (NRCan, 2013).

2.4 UAVs

The emergence of SfM coincided with the popularization of sUAVs. Combined, they greatly increase aerial surveying capacity, particularly where conditions would have otherwise been more difficult, dangerous, expensive, complicated, impracticable or impossible. Multiple studies have successfully used sUAV-SfM (Clapuyt et al., 2016;

¹ Receiver Independent Exchange Format (RINEX) is the de facto data format standard for raw satellite navigation system data management, analysis and exchange (Hatanaka, 2008). This format removes interoperability restrictions commonly found by receiver-specific data formats (Hatanaka, 2008; RINEX Working Group and RTCM-SC104, 2015).

Ely et al., 2016; Lucieer et al., 2014; Mancini et al., 2013; Ryan et al., 2015; Smith and Damià, 2015; Tilly et al., 2016).

UAVs come in various designs and sizes for various functions. sUAVs are defined here as UAVs weighing less than 25 kg, which is the maximum weight at which UAVs can be flown for non-recreational purpose under an Special Flight Operations Certificate (SFOC) exemption from in Canada (Transport Canada, 2018a). Two of the main advantages of sUAVs over their heavier counterparts are lower costs and lower logistical complexity (Laliberté, 2016). For instance, sUAVs can be transported as checked-luggage on commercial aircraft (except for the lithium-ion batteries, which may generally be brought as carry-on, if under 100 Wh (IATA, 2018)) and are easy to transport on sea-ice. Fixed-wing sUAVs are well suited for aerial surveying due to their greater range (Dammann et al., 2018) while multi-rotor sUAVs provide simpler piloting and landing (Laliberté, 2016). sUAVs are generally battery-powered, but these are known to lose their effectiveness at low temperatures, which can be an issue in cold climates (Dammann et al., 2018; Laliberté, 2016).

There are multiple Canadian laws and regulations in effect that restrict the use of UAVs in Canadian airspace. In general, greater flexibility for UAV use requires greater resources to obtain permits and formal training. At the time of writing, the best compromise was to operate under a Transport Canada SFOC exemption status for UAVs weighting between 2 and 25 kg. This exemption status allows UAV flights beyond 5 nautical miles of an airport, and at heights below than 300 ft. (91 m) above ground level.

The UAV had to be operated in good weather, by a pilot with a Pilot Ground School Program certification (Transport Canada, 2016).

3 Methods

3.1 Field Methods

3.1.1 Research site

Research was conducted at Frobisher Bay near Iqaluit, Nunavut (Figure 3.1 a). This location was selected for this research based on reports that the landfast ice there had significant topographic variation. The tide in Iqaluit is semi-diurnal and has an amplitude between 7 and 11 m, the landfast sea-ice was expected to display vertical motion during surveys. This was ideal for testing SfM surveys in non-static landscape, and for witnessing ice deformation processes while safely avoiding drifting ice.

An area near Qaiqsuq Point, approximately 14 km from Iqaluit was chosen as the research site to examine two deformation features. Ground reconnaissance was used along with a high resolution RADARSAT-2 satellite image to identify a suitable field site. A small pressure ridge, with a prominence of approximately 25 cm above the surrounding surface, ran for approximately 4 km in a northeast to southwest direction from an unnamed islet near the shore towards the centre of Frobisher Bay (Figure 3.1c). This pressure ridge was formed within an otherwise unbroken expanse of landfast sea-ice, not a typical ridge formed by moving sea ice (see Section 2.1 on ridge formation). There was also an area of tide-deformed sea-ice adjacent to the islet. Here, the ice was broken into pieces ranging from 2 to 20 m where the sea-ice rested on the sea-bed at low tide and became free-floating again at high tide. This generated an ever-evolving rubble icefield.

3.1.2 SfM surveys

Fieldwork was conducted from May 10-16, 2017. SfM surveys were captured by a payload consisting of a low-cost, L1, carrier-phase recording GPS receiver (*Emlid Reach*; named UAV GPS1 henceforth) and a gimble-mounted *Sony α6000* 24.3 megapixels digital camera equipped with a *Sony E PZ* lens with a focal length of 16-50 mm (24-77 mm in 35 mm equivalent focal length). The payload was mounted on a modified *DJI S800* sUAV, controlled through a *PX4 Pixhawk 4 Autopilot* flight controller with integrated *ICM-20689* and *BMI055* inertial measurement units (IMU)s and navigated with a dedicated *u-blox Neo-M8N* L1 GPS receiver (named UAV GPS2 here) (Figure 3.1d). *Mission Planner* software by *Ardupilot*, version 1.3.50, was used to plan surveys and provided the flight path and shutter activation instructions to the flight controller. The sUAV flew autonomously in a precise ‘lawnmower’ pattern over the survey area until all the planned images were recorded.

A *Topcon HiPer V* L1/L2 GPS receiver located on the nearby islet (hereafter referred to as Land GPS) was used as a PPK base station (Figure 3.1b). Two additional GPS receivers, a *Topcon HiPer V* and a *Emlid Reach* (Ice GPS1 and Ice GPS2, respectively) were located on the ice surface to continuously record changes in sea-level. These data were subsequently PPK-processed using data from the Land GPS. A measured offset from the water surface through an adjacent hole in the ice up to each GPS receiver was subtracted from the GPS elevation data for accurate sea-level measurements. These were then used to calculate the elevation of survey points above sea level throughout the study. Four 27 cm x 27 cm markers were placed near the corners

of the survey area and were used as GCPs after being surveyed (see below). Although it is generally recommended to use as many GCPs as possible to obtain the most accurate SfM surveying results (Agisoft LLC, 2017), one objective of this research was to determine the accuracy of an SfM solution unaided by GCPs (via indirect georeferencing). The presence of multiple high-contrast GCPs on the sea-ice surface would not test the ability of SfM to generate keypoints and conduct bundle adjustments from a pristine sea-ice surface, so the use of GCPs was minimized.

The camera settings were chosen manually before each survey to optimize image quality by maximizing shutter speed (to reduce blur), widening the aperture (since depth of field is not a concern) and setting the ISO low nominally, with a sensitivity to allow the ISO to rise in response to low light conditions without underexposing the images. During the SfM surveys, the camera shutter was activated at specific time or distance intervals (depending on the survey plan) by the flight controller. The shutter interval was chosen to provide sufficient side- and overlap based on the flight path, elevation and camera focal length. The time that the camera shutter signal was sent (timestamp) was recorded in the UAV flight controller log file, which also contained the UAV attitude information provided by the *PX4 Pixhawk 4 Autopilot* IMUs, and the UAV GPS2 position and time data. A hot shoe adapter on the camera sent a signal to UAV GPS1 at the exact moment the camera shutter was opened, where it was recorded in the form of a timestamp and a position. A schematic of this workflow is presented in Appendix A1.

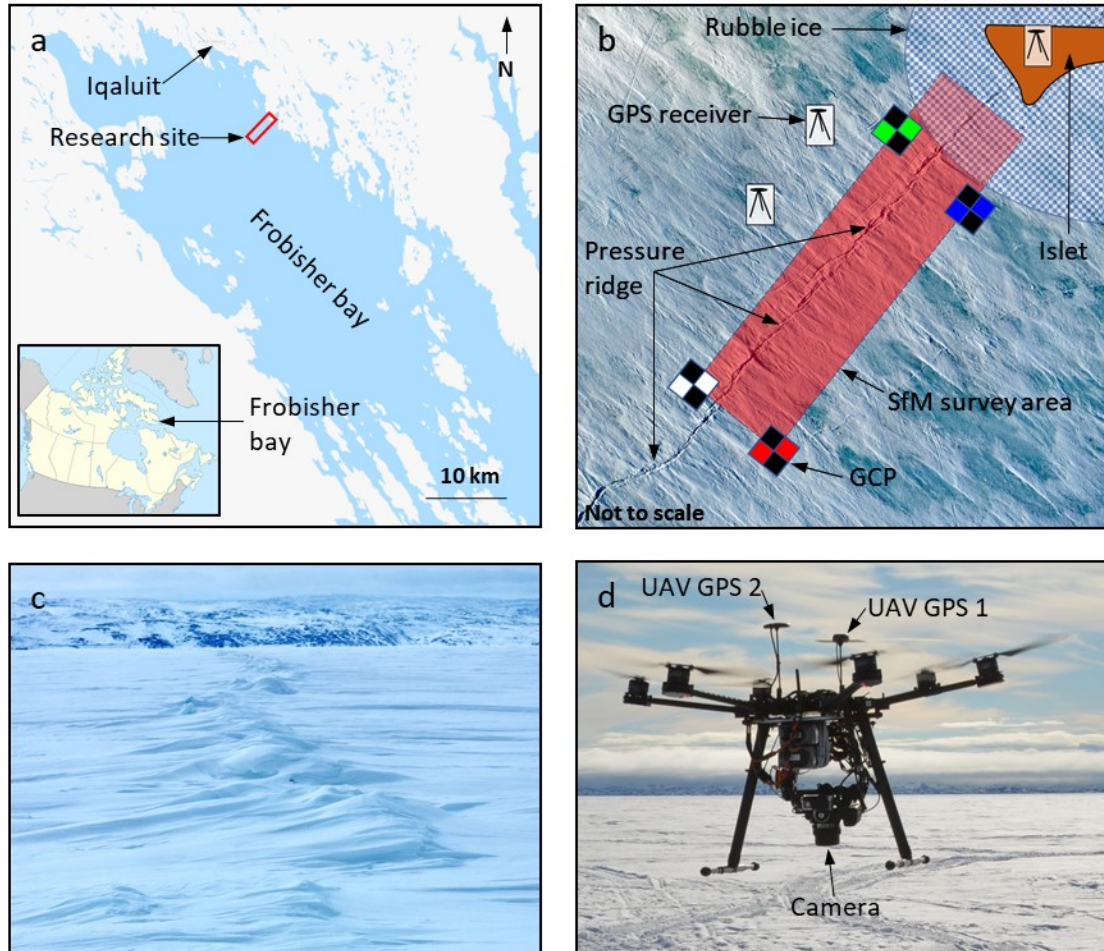


Figure 3.1. Overview of the research site and experimental setup.

The (a) general position of the research site within Frobisher Bay, marked with a red boundary. A (b) generic site sketch of a SfM survey area. The SfM survey area and position of GCPs varied between surveys. The (c) pressure ridge as it appeared from eye-level. The ridge had a prominence of approximately 25 cm above the surrounding surface. The (d) main components of the sUAV, including the payload (camera and UAV GPS 1).

Sources: Canada map by Styx on Wikimedia Commons (CC BY-SA 3.0), Frobisher bay map by © OpenStreetMap contributors (ODbL).

3.1.3 Ground surveys

A ground survey covering 5000 m² of the study area (approximately 40% of the area surveyed by SfM Surveys 1, 2 or 3) was conducted on May 10th to provide a topographical reference dataset for accuracy calculations. Ice GPS1 was mounted on a survey pole and points were measured up from the surface (ice or snow). A total of 65 evenly-spaced points were manually recorded over a level section of sea-ice using a *Topcon Tesla* tablet computer. The GCP positions were also recorded. The elevation of these survey points was adjusted to sea level using the data from Ice GPS2.

3.1.4 Experiment design

To meet the objectives of this thesis, several SfM surveys were conducted (Table 3.1). These included three surveys conducted in quick succession with identical² survey parameters (Table 3.1; SfM Surveys 1-3). These three surveys were designed to calculate the accuracy, precision and repeatability of the technique by comparing the results to each other and to the reference ground survey (Objective 1). SfM Surveys 4 to 8 were variations of SfM Surveys 1-3. They were designed to evaluate the overall impact of variations in the survey parameters such as UAV altitude (SfM Surveys 4 and 7) atmospheric and lighting conditions (SfM Survey 5), focal length (SfM Survey 6), and spatial scale (SfM Survey 8) (Objective 3). The next five surveys (SfM Surveys 9-13) had identical surveying parameters and were conducted to observe sea-ice deformation over a tidal cycle. Coincidentally, they were conducted at the lunar perigee, which

² The only non-identical parameter was the focal length, which was mistakenly set to 16 mm for SfM Survey 1.

generated the greatest tidal amplitude of the lunar month. This should therefore correspond the maximum extent of ice deformation in the study area (Objective 2). SfM Surveys 14 a and b were conducted to map the entire length of the ridge (4 km), with Survey 14a on the northwest side of the ridge and Survey 14b on the southeast. This experiment was conducted to determine if this expedient way of surveying ridges was achievable and yielded acceptable results (Objective 3). No GCPs were used for SfM Survey 14.

Table 3.1. Survey parameters and environmental conditions.

Survey name	Date	Focal				Atmospheric conditions	Sea-ice condition	Images captured	Area surveyed (m)
		Altitude (m)	length (mm)	Overlap ratio	Sidelap ratio				
SfM Survey 1	10 May	45	16	0.875	0.875	Overcast	Wet snow	376	100 x 100
SfM Survey 2	10 May	45	20	0.875	0.875	Overcast	Wet snow	385	100 x 100
SfM Survey 3	10 May	45	20	0.875	0.875	Overcast	Wet snow	379	100 x 100
SfM Survey 4	10 May	90	16	0.875	0.875	Overcast	Wet snow	413	100 x 100
Ground survey*	10 May	N/A	N/A	N/A	N/A	N/A	N/A	66*	50 x 100
SfM Survey 5	11 May	45	20	0.875	0.875	Sunny	Wet snow	284	100 x 100
SfM Survey 6	11 May	45	40	0.75	0.75	Sunny	Wet snow	385	100 x 100
SfM Survey 7	11 May	90	20	0.875	0.875	Sunny	Wet snow	186	100 x 100
SfM Survey 8	11 May	90	16	0.75	0.75	Sunny	Wet snow	146	300 x 300
SfM Survey 9	11 May	90	16	0.75	0.75	Sunny	Wet snow	91	150 x 500
SfM Survey 10	13 May	90	16	0.75	0.75	Overcast	Water puddles	92	150 x 500
SfM Survey 11	13 May	90	16	0.75	0.75	Variable	Water puddles	92	150 x 500
SfM Survey 12	13 May	90	16	0.75	0.75	Overcast	Water puddles	92	150 x 500
SfM Survey 13	13 May	90	16	0.75	0.75	Low light	Water puddles	92	150 x 500
SfM Survey 14**	16 May	90	16	0.875	Variable	Overcast	Fresh snow	579	100 x 4000

*The ground survey differs from all other surveys listed as it is not an SfM survey. The number listed in the *Images captured* column represent the amount of survey points taken of the sea-ice surface.

**SfM Survey 14 combines sub-surveys 14a and b, which were conducted in succession.

3.2 SfM data analysis

3.2.1 Data preparation

A schematic of the data preparation workflow is presented in Appendix A2. Each GPS file was converted to the RINEX file format using proprietary software from the manufacturers (*Topcon Link* version 8.2 for the *Topcon HiPer V* receivers and *RTKCONV* version 2.4.3 Emlid b28 for the *Emlid Reach* receivers). The Land GPS RINEX files were PPP-processed using the online *NRCan CSRS-PPP* tool. The *Canadian Geodetic Vertical Datum of 2013* (CGVD2013) was used for elevation. The corrected Land GPS positions were subsequently used as temporary surveying monuments and as base stations for PPK. The remaining RINEX files corresponding to the UAV flights, the ground survey and the ice position were then PPK-processed.

The *RTKLIB* software (version 2.4.2 for *Topcon HiPer V* files and version 2.4.3 Emlid b28 for *Emlid Reach* files) used the matching Land GPS RINEX file PPP-calculated position for the base station data, and the *International GNSS Service* (IGS, n.d.) highest-accuracy corrected products for satellite ephemerides, earth rotation and atmospheric parameters to calculate the positions of UAV GPS1, Ice GPS1 and 2 with a high accuracy. The resulting geographical coordinates were then projected to the Universal Transverse Mercator (UTM) coordinate system (zone 19N) to simplify subsequent calculations. Elevations were converted from the land-based CGDV2013 datum to a real-time sea level datum using Ice GPS1 and/or 2 data.

On the sUAV, the camera optical centre was offset from UAV GPS1 location by several cm (Fig 3.1d). This was corrected by accounting for the distance between the two instruments in Cartesian coordinates ($\Delta X_0 = 0.152$ m, $\Delta Y_0 = -0.103$, $\Delta Z_0 = -0.406$ m) and the rotation of the sUAV airframe. Attitude data was obtained from the GPS-timestamped UAV log files, recorded every 100 ms and spline-interpolated to 1 ms intervals using a custom R script, presented in Appendix B (the results were examined visually to eliminate the possibility of interpolation errors). Roto-translational offsets were then computed using Equations 1, 2 and 3 and applied to the position of UAV GPS1 so that it represented camera position:

$$\Delta X_1 = \left(\Delta X_0 \cos(\theta) - (-\Delta Y_0 \sin(\varphi) + \Delta Z_0 \cos(\varphi)) \sin(\theta) \right) \cos(\psi) \quad \text{Equation 1}$$

$$- (\Delta Y_0 \cos(\varphi) + \Delta Z_0 \sin(\varphi)) \sin(\psi)$$

$$\Delta Y_1 = \left(\Delta X_0 \cos(\theta) - (-\Delta Y_0 \sin(\varphi) + \Delta Z_0 \cos(\varphi)) \sin(\theta) \right) \sin(\psi) \quad \text{Equation 2}$$

$$+ (\Delta Y_0 \cos(\varphi) + \Delta Z_0 \sin(\varphi)) \cos(\psi)$$

$$\Delta Z_1 = \Delta X_0 \sin(\theta) + (-\Delta Y_0 \sin(\varphi) + \Delta Z_0 \cos(\varphi)) \cos(\theta) \quad \text{Equation 3}$$

Where ΔX_0 , ΔY_0 , and ΔZ_0 represented the nominal position of the camera along the x, y and z axis, ΔX_1 , ΔY_1 and ΔZ_1 corresponded to the attitude-corrected position, and φ , θ , and ψ represented roll, pitch and yaw (the attitude), as per aeronautical convention. The position of the camera at every shutter trigger event logged by UAV GPS1 was extracted and associated with each image taken during the surveys. These positions were logged to a *comma-separated values* (CSV) file.

In the raw images captured by the camera, the contrast of the sea-ice surface was poor. This was an anticipated challenge for SfM analysis of sea ice (Fonstad et al., 2013; Smith et al., 2016; Westoby et al., 2012), especially for keypoint identification and matching and multi-view stereo image matching. As suggested by Nolan et al. (2015) the contrast was increased in every raw image file. Using the camera-bundled *Phase One* software (version 10.1.2) by *Capture One Express*, Gaussian stretches to approximately three standard deviations were manually performed on the image histogram after a white balance was applied. The image modifications were applied identically within each SfM survey, ensuring uniformity between photos. All images were then converted to the JPEG file format with a quality setting of 100 to reduce data storage and processing time for the next step, while minimizing data loss due to compression.

3.2.2 Structure from motion and point cloud preparation

SfM survey photos, image positions and GCP positions (when available) were processed using *Agisoft Photoscan* (version 1.3.4) on a high-end desktop computer (*Intel Core i7-5820K* 3.3 GHz CPU, 32 GB of RAM, three *ADM Radeon R9 200* GPU and a 1 TB SSD) to derive point clouds and orthophotos. JPEG images were aligned using the ‘highest accuracy’ setting and then a dense point cloud (named raw point cloud here) was built with the ‘high accuracy’ setting and without depth filtering. Depth filtering was omitted due to proprietary filtering algorithms used by the software (Agisoft LLC, 2017) and because manual filtering was conducted in a later step. Orthophotos were exported with a pixel size of 2 cm for all surveys to facilitate registration and comparison between

surveys. The large number of SfM surveys conducted, the time required to prepare and process each survey, and significant GPS reliability issues (discussed in Section 4.3.1) precluded the processing of every survey. Therefore, only SfM Surveys 1-3 and 9-14 were processed.

Raw point clouds were modified and visualized using the *CloudCompare* version 2.9 open-source software. The raw point clouds generated by *Agisoft Photoscan* had between 8×10^7 to 4×10^8 points, which slowed down the processing and visualisation. In addition, high frequency noise in the point positions made the surface boundary appear diffuse (the boundary appeared as a layer of points 5 to 10 cm thick). Raw point cloud decimation and averaging were conducted using a method proposed by Dimitri (2015). The *Multiscale Model to Model Cloud Compare (M3C2)* plugin was used to generate a 'core point' point cloud (named core point cloud here), which reduced the number of points by one to two orders of magnitude and sharpened the estimated sea-ice surface boundary. Core points are uniformly spaced and represent the mean position of all the original points located within a cylinder of a specific diameter and height, which is oriented normal to the point cloud surface of a larger subsampled section of the point cloud (Figure 3.2). The core point clouds covered an area much larger than the planned surveying area, since *Agisoft Photoscan* generated points everywhere there was sufficient overlap of images. This larger area (named raw area) was then cropped to the SfM survey boundaries (named cropped area) prior to further analysis (Figure 3.3).

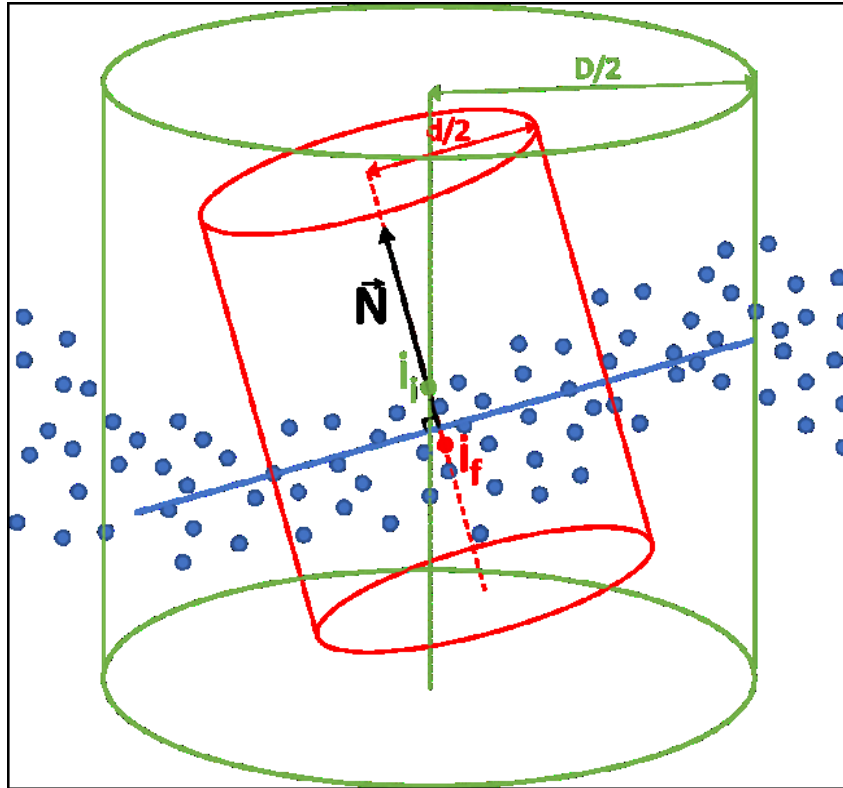


Figure 3.2. Visual representation of the *Multiscale Model to Model Cloud Compare* (M3C2) algorithm used to average and decimate the point cloud.

A vertical cylinder (green) of diameter D centered on evenly-spaced initial core points i_i isolated a portion of the point cloud. The best-fitting plane through this cylinder (blue line, represented in 2D here) was calculated along with a surface normal vector (N). A second cylinder (red) of diameter d centred on i_i and aligned with N was used to define the local surface. The mean position of points along the cylinder's main axis was used to define the final core point position i_f . Values of $D=40$ cm and $d=20$ cm were used in this study.

Sketch adapted from figures by Lague (2013).

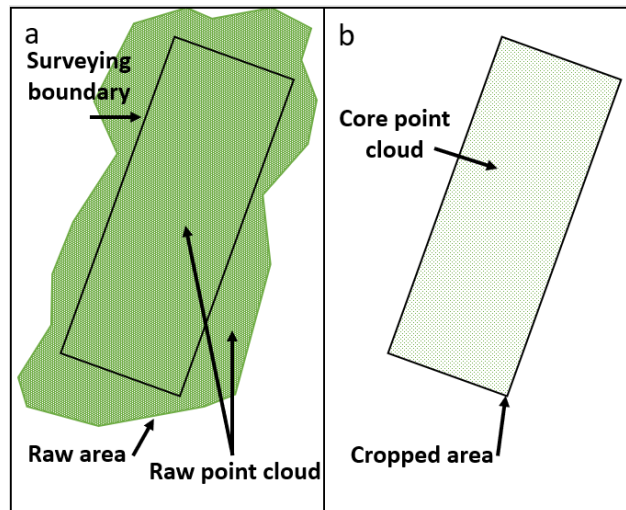


Figure 3.3. Schematic representing the point cloud workflow with a fictional raw point cloud.

(a) The output from *Agisoft Photoscan* is a raw point cloud covering a raw area wider than the original surveying boundaries. (b) The point cloud averaging, decimating and cropping operations results in a core point cloud spatially limited to the cropped area.

3.2.3 Accuracy, precision and repeatability

The *Cloud-to-Cloud Distance* tool from *CloudCompare* was used to quantify the distance and direction between a *reference* point cloud and a *compared* point cloud. For a hypothetical *compared* point cloud A and a *reference* point cloud B, the nearest neighbour in A of every point in B is found, and vectors corresponding to the distance and direction between those neighbouring points are assigned to every point in B (CloudCompareWiki, 2015). The result of the assignment of vector values to points clouds is referred to as *vector field* (i.e. “cloud of vectors”)

Horizontal registration between mostly flat point clouds is difficult (Nolan et al., 2015) and so only the vertical component of the distance vectors (Z_{dist}) was extracted and

used in subsequent analyses. This approach is widely used to assess SfM quality (Fonstad et al., 2013; Girod et al., 2017; Smith and Damià, 2015), either through point cloud operations or Digital Elevation Models (DEM). As the Z_{dist} is a scalar value applied to points in a point cloud, the resulting entity is referred to as a *scalar field*. For Z_{dist} scalar fields, positive Z_{dist} values indicates that a *reference* point cloud B is at a higher elevation than *compared* point cloud A and, conversely, negative values represent areas where point cloud B is at a lower elevation than point cloud A ($Z_{\text{dist}} = B - A$).

Shapiro-Wilk tests were performed to determine if the Z_{dist} distributions were normally distributed. The accuracy, precision, and repeatability values were then derived from the Z_{dist} normal distributions using parametric statistics.

3.2.3.1 Accuracy and precision

To measure the accuracy and precision of sUAV-SfM, the ground survey was used as a reference dataset. The Z_{dist} between each ground survey point and SfM core point were calculated. As per the convention previously stated, a positive Z_{dist} value indicates that the ground survey is at a higher elevation than the SfM survey, while a negative value indicates the opposite. The mean, standard deviation and RMSE were subsequently calculated for the Z_{dist} distributions. The effects of the measurement errors from the various instruments (Figure 3.4) were also calculated and evaluated against the Z_{dist} distributions. These errors were either estimated in the case of manual measurements or were provided by the PPP and PPK files for GPS measurements. Root

mean square (RMS) additions (Equation 4) was used to account for error propagation between the instruments (Taylor, 1997).

3.2.3.2 Repeatability

To measure repeatability, two surveys that measure identical surfaces are required. Thus, the rubble ice area was cropped (due to significant tidal-induced topographical changes between the surveys). The remaining sea-ice topography was assumed to be unchanged between surveys. This assumption may not be valid at the pressure ridge area, however, the small areal extent of the ridge (approximately 2-3% of the study area), and the magnitude of vertical change observed (approximately 3 mm) suggested that the impact of the temporal variability is negligible. Once the areas containing rubble ice were cropped, the different core point clouds were assembled in pairs (each possible pair was formed) and for each, the *Cloud-to-Cloud Distance* tool was used to generate Z_{dist} scalar fields. Again, the mean, standard deviation and RMSE were calculated for the Z_{dist} distribution. In addition, the sources of instrumental error (Figure 3.4) and their impacts were measured. The sources of instrumental error for sUAV-SfM survey-to-sUAV-SfM survey distance calculations were equivalent to the RMS addition of the instrumental error (Equation 4) of two sUAV-SfM surveys.

$$\delta q = \sqrt{(\delta a)^2 + (\delta b)^2 + (\delta c)^2 + \dots + (\delta j)^2} \quad \text{Equation 4}$$

Where δa , δb , δc , (...) and δj represented the measurement errors from each instrument while δq corresponded to the total instrument source of error.

The above repeatability steps were then repeated, but after a fine post-SfM registration of each point cloud pairs were conducted. This was accomplished using the *Iterative Closest Point* tool in *CloudCompare*, which iteratively minimizes the root mean square point to point distance between two point clouds through translations and rotations (CloudCompareWiki, 2015). This allowed for a better differentiation between systematic errors and local surface quality when compared with the previous *unregistered* SfM survey pairs, as per Nolan et al (2015). Improved post-SfM registration was also important for detecting topographical change.

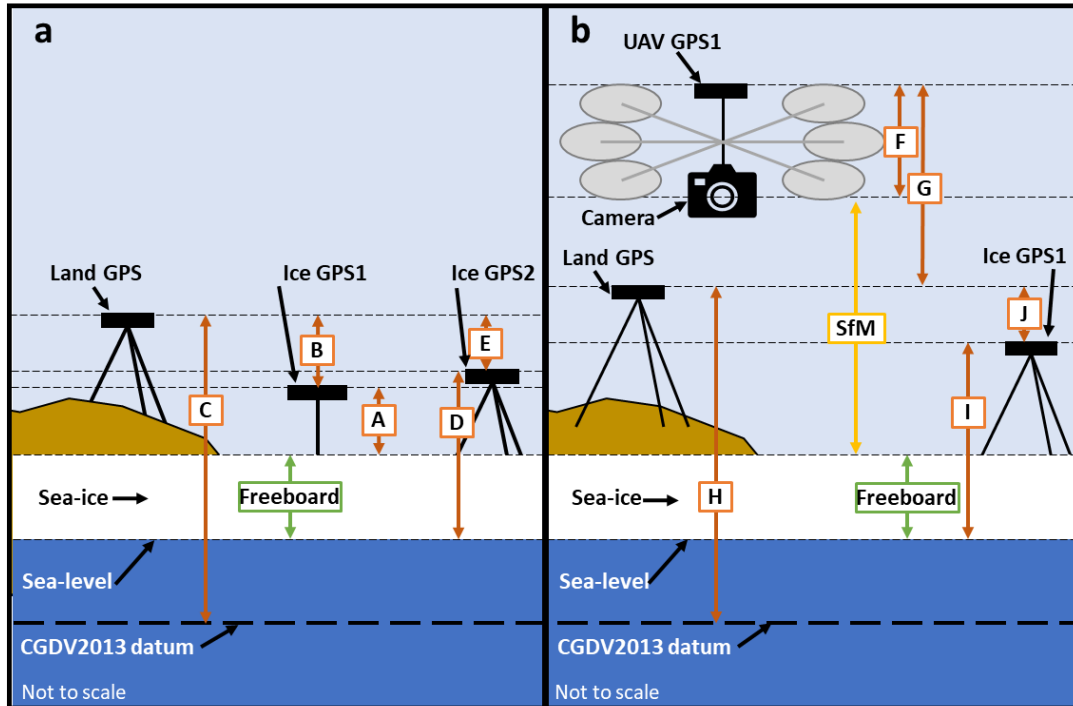


Figure 3.4. Schematic of the sources of vertical error due to instruments for the (a) ground survey and (b) the sUAV-SfM surveys.

Sources of instrumental measurement error: (A) ice surface to Ice GPS1 (mounted on a surveying pole), (B) Ice GPS1 to Land GPS, (C) Land GPS to the CGDV2013 vertical datum, (D) Ice GPS2 to sea-level, (E) Ice GPS2 to Land GPS, (F) camera to UAV GPS1, (G) UAV GPS1 to Land GPS, (H) Land GPS to the CGDV2013 vertical datum, (I) Ice GPS1 to sea-level and (J) Ice GPS1 to Land GPS.

3.2.4 Mapping sea-ice topography

Core point clouds were mapped to show elevation and Z_{dist} scalar values, providing a visualization of the sea-ice topography, shape and texture, as well as topographical changes, and spatial distribution of errors. Orthophotos were used as an independent dataset to observe and interpret the sea-ice topography and features, and, when used in conjunction with point clouds, to interpret the point cloud data.

Point cloud-based digital elevation models (DEMs) were checked for artifacts such as below sea-level surface elevations, and tilts, waves, bulges or bowls which provided additional information about the data quality of the core point clouds.

Visual analysis of the Z_{dist} maps was conducted to study the spatial distribution of the repeatability errors and distinguish these errors from topographical changes. In areas where topographical changes were detected, statistical analysis of the Z_{dist} distributions within and outside the areas where topographical change was observed were conducted to quantify the magnitude of the change. When repeatability errors were suspected, their spatial distribution, spatial scale and shape were used to narrow down the underlying causes.

The orthophotos were visually inspected to determine which sea-ice surface features were detectable by the topographic data. Orthophotos were also used to interpret point cloud transects across the rubble ice area. These transects were conducted to visualize the changes in ice topography over time across this area experiencing metre-scale vertical movement due to tides. The transect orientation was selected to maximize transect length, while traversing a high diversity of ice elevations and types. The elevations were plotted relative to a fixed, land-based vertical datum, instead of the sea-level based vertical datum that was used for the previous analyses.

3.3 Operational performance

The operational performance was determined by evaluating four factors which determine the ability of sUAV-SfM to be a valuable sea-ice surveying technique: reliability, surveying and processing speed, simplicity and cost.

3.3.1 Reliability

Reliability was defined here as the ability to consistently collect the required data without equipment failure (equipment reliability) and then process it reliably (data reliability). It was quantified by calculating the fraction of field time when equipment was fully operational as well as the percentage of data that was useable. The equipment's availability throughout fieldwork, the GPS receivers data and the ability of sUAV-SfM to resolve snow and sea-ice topography were evaluated.

The main pieces of equipment (Land GPS, Ice GPS1 and 2, and UAV GPS1, camera, UAV and flight controller) were first assessed for their reliability during fieldwork, regardless of data quality.

The GPS receiver data reliability measurement was based on the specific use of the instrument.

1. For the Land GPS, reliability was calculated per data file, by evaluating the vertical accuracy as calculated in the PPP correction process. Vertical

accuracies of less than 4 cm were considered reliable, based on results from Krzan et al. (2017).

2. For Ice GPS1 and 2, reliability was calculated per time, by measuring the frequency with which the GPS-calculated sea-level elevations diverged from the expected tidal movement.

3. For UAV GPS1, the reliability was calculated using two different criteria. Reliability was first calculated for each SfM survey by identifying unreliable GPS data from the post-SfM reports generated by *Agisoft Photoscan*. The software calculated a camera location error estimate during the bundle adjustment step for each SfM survey (Agisoft LLC, 2017). A threshold for visible systemic quality issues was chosen to be a camera location error of less than 25 cm. This value was selected based on a natural break in camera location error between SfM surveys of relatively good quality (with camera location errors of up to 21.4 cm) and SfM surveys of lower quality (with camera location errors of 33.4 cm and up). Further details on SfM survey quality are provided in Section 4.

Reliability was also calculated based on image timestamps, by counting the number of shutter activation timestamps recorded by the receiver over the total amount of images captured, and by calculating how many SfM surveys had all their images timestamped.

The reliability for sUAV-SfM to resolve low contrast surfaces was calculated for each survey, using two criteria:

1. As low-contrast surfaces are known to prevent the SfM software to generate points over metre-size patches and larger under certain circumstances (e.g. Crawford et al., 2018), the first criterion to measure the low-contrast resolving reliability of sUAV-SfM was to visually verify the point clouds within the cropped area and observe if metre-sized gaps could be found; and
2. The raw point cloud density (not the core point cloud) was compared to two data density measures: the ground resolution (i.e. GSD) and the total number of photographpixels used to generate the point cloud. The latter was calculated by multiplying the *ground resolution* with the *effective overlap* (the effective overlap indicated the average number of times every point within the surveyed location was captured by an image over the survey – this value was provided by the SfM report by *Agisoft Photoscan*). If low-contrast surfaces were to have an impact on the generation of points or keypoints, more data would be required per point generated. Therefore, low-contrast environments, such as with SfM Survey 14 (which had a new snow cover and overcast conditions), were compared with similar surveys of greater contrast, such as SfM Survey 11 (which had melting snow with sunny weather).

3.3.2 Surveying and processing speed

Speed was the second factor considered in the operational performance. It was evaluated for the data collection phase and sUAV-SfM data-processing phase, by comparing either the flight time of the UAV or the computer-processing time to generate a raw point cloud to the area surveyed and the number of points collected for each survey.

3.3.3 Simplicity

Simplicity was the third evaluated factor for operational performance. Survey simplicity was defined here as ease of the tasks required to prepare and operate the equipment and to post-process the data. Although most of the results were subjective (i.e. advantages and disadvantages), time was also used as a quantifiable means of expressing the simplicity of certain tasks, since complex tasks usually require more time to complete.

3.3.4 Costs

For the cost calculations, a series of assumptions had to be made. The calculated costs had to be representative of the equipment and licenses used during this thesis to conduct the surveys (sUAV-SfM and ground surveys) and fully process the data. As such, this thesis does not analyze the costs of other sUAV-SfM equipment or licences, which can vary greatly. But by providing a cost breakdown for the major research items used for this thesis, subsequent comparisons to other current or future sUAV-SfM systems are simplified. When the cost of an item was unknown, the cost of an equivalent

item was used instead. The maintenance costs were ignored since the number of SfM surveys conducted was not large enough to properly estimate the equipment failure rates. The logistical costs of the fieldwork (transport, food, lodging, clothing, etc.) were also excluded as the impacts of the duration and location of the fieldwork on the costs were unlikely to be representative for most potential users of the technique. As the surveying and data-processing didn't require consumables except for the electricity required to charge the batteries and run the computers, the associated electricity costs for surveying and data-processing were also ignored.

The remaining costs included the surveying equipment, the UAV pilot certification, the data-processing equipment and software license. These were separated into two categories based on the expected usage of the item for a typical sUAV-SfM surveyor. The *exclusive-usage items* category contained items expected to be purchased and used solely for sUAV-SfM surveying of sea-ice, while the *shared-usage items* category contained items that could be used for other purposes when not being used for sUAV-SfM surveys and would likely be available to most individuals/organisations interested in conducting sea-ice surveys. This separation was done to better represent the expected costs for a typical user. All cost calculations were conducted using Canadian dollars.

4 Results

Over four days of fieldwork, the fourteen SfM surveys yielded a total of 3592 images. The nine processed SfM surveys represented a total (overlapping) surveyed area of 1.32 km² (raw area), covered by a total of 1.34×10^9 points (raw point clouds), for an average of 1019 points per m². In all processed surveys, the ridge and rubble field were identifiable topographical features (Figure 4.1).

There were data quality issues for Surveys 1 to 4, 9, 10 and 14 which became apparent during post-processing, rendering these surveys unusable for the purposes of this thesis (in addition to SfM Surveys 5 to 8, which were not processed). To address the objective of determining the accuracy, precision and repeatability, SfM Surveys 11, 12 and 13 (Table 4.1) were analyzed and the quantitative results were interpreted. The results from the other surveys, the related data quality issues and the overall outcomes from these issues are provided in section 4.3.

Table 4.1. Details of SfM Surveys 11, 12 and 13 conducted on May 13th, 2017.

SfM Survey		11	12	13
Start of flight	Time (UTC)	21:27:49	22:58:04	00:52:29
	Tide elevation* (m)	-12.37	-9.31	-6.52
End of flight	Time (UTC)	21:36:17	23:05:02	00:59:27
	Tide elevation* (m)	-12.11	-9.08	-6.44
Flight total	SfM survey duration	00:08:28	00:06:58	00:06:58
	Tidal motion (m)	0.26	0.23	0.07
Raw point cloud	Raw area (m ²)	119 000	118 000	127 000
	Number of points	82 503 749	81 524 960	80 386 320
	Point density (per m ²)	693	691	633
Core point cloud	Cropped area (m ²)	48 686	48 686	48 686
	Number of points	2 827 023	2 869 149	2 980 500
	Point density (per m ²)	58	59	61

*The elevation datum used was the Canadian Geodetic Vertical Datum of 2013 (CGVD2013)

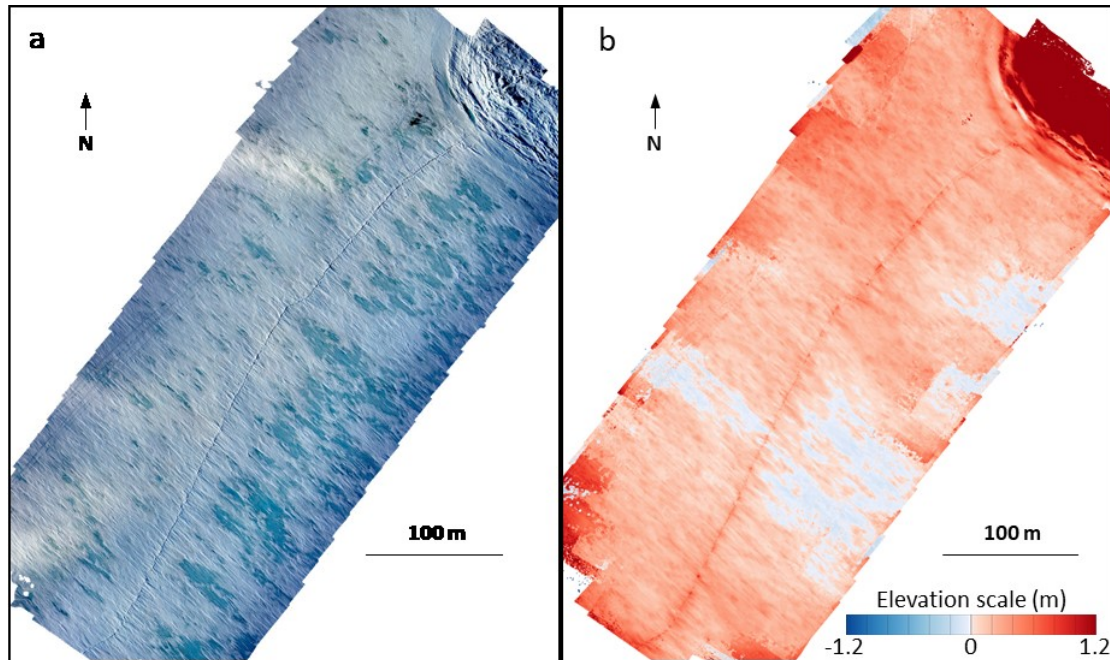


Figure 4.1. SfM output examples.

SfM Survey 11 was conducted on May 13 near the lunar month's tidal minimum. The SfM survey collected 92 images (4 rows of 23 images each) at an altitude of 90 m, a focal length of 16 mm and a side- and overlap ratio of 0.75. The survey area was approximately 150 x 500 m and was centred on the pressure ridge. The data was processed with *Agisoft Photoscan*, which generated (a) a mosaicked orthophoto of the raw area, and (b) a core point cloud of the raw area (subsequently decimated and averaged with the *CloudCompare M3C2* plugin). Three distinct sea-ice features can be observed in both outputs: the ridge (main central linear feature), the rubble field (northeast corner) and level ice. For scale, two snowmobiles and a qamutik (a traditional Inuit sled) are visible in the orthophoto as a dark spot near the rubble field. These are also faintly visible as dark red spots on the point cloud.

4.1 SfM survey quality

4.1.1 Accuracy and precision

The May 10th ground survey was supposed to be compared with SfM Surveys 1, 2 and 3, conducted earlier on the same day. Since these SfM surveys were unusable due to

the data quality issues described above, the SfM Surveys 11, 12 and 13 conducted on May 13th were used instead. The main consequences of this modification were twofold. Only a partial overlap existed between the ground survey (36 of the 66 points overlapped) and the SfM surveys (4% of the surface overlapped)³, and the sea-ice surface experienced an un-quantified amount of melt and disturbance between the ground and SfM surveys, which may have generated inconsistencies between the surveys.

The Z_{dist} values (Figure 4.2) between the ground survey and the core point clouds of SfM Surveys 11, 12 and 13 were evaluated with a Shapiro-Wilk test, which determined that for each SfM survey, all values were normally distributed (p-values were 0.59, 0.34 and 0.66, respectively). Parametric statistics were therefore used to calculate the Z_{dist} accuracy and precision for each SfM survey (Table 4.2). The average of the three SfM surveys yielded an accuracy of 56 ± 14 mm (95% confidence interval – CI), a precision of 40 mm, a RMSE of 69 mm and a RMSE:range ratio of 1:1265. For the contribution of the instrument sources of errors to the Z_{dist} RMSE, each individual instrument source of error is listed in Table 4.3. The RMS additions of these instrument sources of error is 35 mm. This accounted for approximately 14 % of the 69 mm average Z_{dist} RMSE. Overall, this suggests that the instrumental error can be considered a small source of error.

³ This was a result of the significantly smaller areas surveyed (Table 3.1) and an incomplete overlap between SfM Surveys 1, 2 and 3 when compared with SfM Surveys 11, 12 and 13.

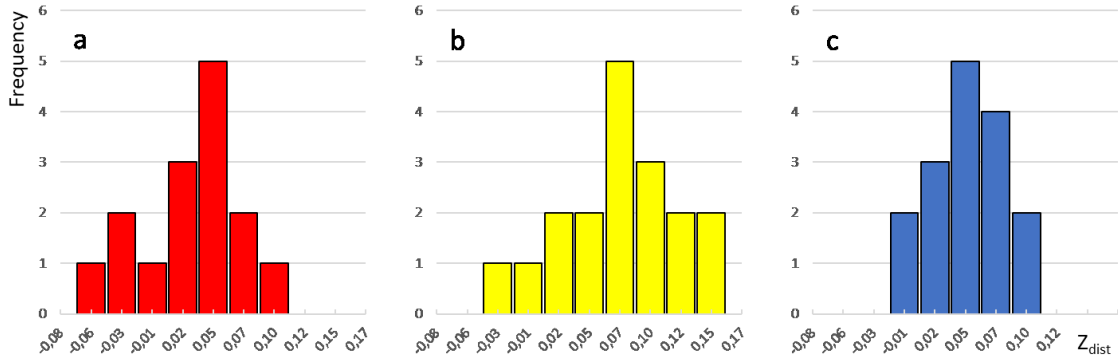


Figure 4.2. Histograms of the elevation difference (Z_{dist}) between SfM Survey 11 (a), 12 (b) and 13 (c) core point clouds and the ground survey points (n=36).

These distributions were not significantly different from normal ($p=0.59, 0.34$ and 0.66 , respectively).

Table 4.2. Z_{dist} statistics for SfM Surveys 11 to 13.

The mean, standard deviation, standard error (SE), RMSE and RMSE:range ratio were calculated for SfM Survey 11, 12 and 13, and were averaged in the last column to provide a representative value for the technique. The positive Mean Z_{dist} indicates that the SfM surveys were consistently biased to a lower elevation than the ground survey.

Survey name	Survey 11	Survey 12	Survey 13	Average
Mean Z_{dist} (m)	0.041	0.066	0.062	0.056
Standard error of Z_{dist} (m)	0.006	0.009	0.005	0.007
Standard deviation of Z_{dist} (m)	0.035	0.055	0.029	0.040
RMSE of Z_{dist} (m)	0.053	0.085	0.069	0.069
RMSE:range ratio	1:1632	1:1028	1:1275	1:1265

Survey name	Survey 11	Survey 12	Survey 13	Average
Mean Z_{dist} (m)	0.041	0.066	0.062	0.056
Standard deviation of Z_{dist} (m)	0.035	0.055	0.029	0.040
Standard error of Z_{dist} (m)	0.006	0.009	0.005	0.007
RMSE of Z_{dist} (m)	0.053	0.085	0.069	0.069
RMSE:range ratio	1:1632	1:1028	1:1275	1:1265

Table 4.3. Sources of vertical error due to instrumental measurements for the ground survey and sUAV-SfM surveys. The total instrument source of error was calculated using RMS additions.

List of instrument errors	Results per survey			Average
Ground survey instrument error	Ground survey			
Sea-ice surface to Ice GPS1 error* (m)	0.010			0.010
Ice GPS1 to Land GPS error (m)	0.006			0.006
Land GPS to vertical datum error (m)	0.008			0.008
Ice GPS2 to sea-level error* (m)	0.010			0.010
Ice GPS2 to Land GPS error* (m)	0.010			0.010
Ground survey RMS sum of errors (m)	0.020			0.020
SfM survey instrument error	Survey 11	Survey 12	Survey 13	
Camera to UAV GPS 1 error* (m)	0.010	0.010	0.010	0.010
UAV GPS1 to Land GPS error (m)	0.027	0.013	0.017	0.019
Land GPS to vertical datum error (m)	0.006	0.006	0.017	0.009
Ice GPS1 to sea-level error* (m)	0.010	0.010	0.010	0.010
Ice GPS1 to Land GPS error* (m)	0.010	0.010	0.010	0.010
SfM surveys RMS sum of errors (m)	0.033	0.022	0.030	0.028
Total instrument source of error (m)	0.038	0.030	0.036	0.035

* Estimated values

4.1.2 Repeatability

The Shapiro-Wilk test values for the Z_{dist} distributions of the core point clouds associated with the unregistered surveys (the *unregistered distributions*) of SfM Survey pairs 11-12, 11-13 and 12-13 (Figure 4.3), using a 600-point sample from each distribution, determined that the distributions were normal with p-values of 0.94, 1.0 and 1.0 for each respective SfM survey pair. These high p-values combined with a visual comparison between the unregistered and post-SfM registered distributions (i.e. the

distributions associated with the post-SfM registered surveys) (Figure 4.3) were sufficient to determine that the post-SfM registered distributions were also normally distributed. Overall, the unregistered distributions were mostly centered on zero, with an average mean Z_{dist} over all three surveys of 20 mm. The post-SfM registration only minimally improved the alignment of the distributions (Figure 4.3), indicating that the unregistered point clouds generated by *Agisoft Photoscan* already had a high level of registration. The unregistered point cloud pairs had an average Z_{dist} standard deviation of 77 mm and a RMSE of 80 mm (Table 4.4), while for the post-SfM registered pairs, the average standard deviation was 69 mm (equal to the RMSE due to the mean Z_{dist} of zero – Table 4.5). The 95% confidence interval for all the mean values was less than a millimetre due to the large distribution size (>2 million). The total instrumental error was 40 mm, which accounted for 13% and 19% of the total error for the unregistered and the post-SfM registered point cloud distributions, respectively (Table 4.6) and can be considered to be a small proportion of the total error.

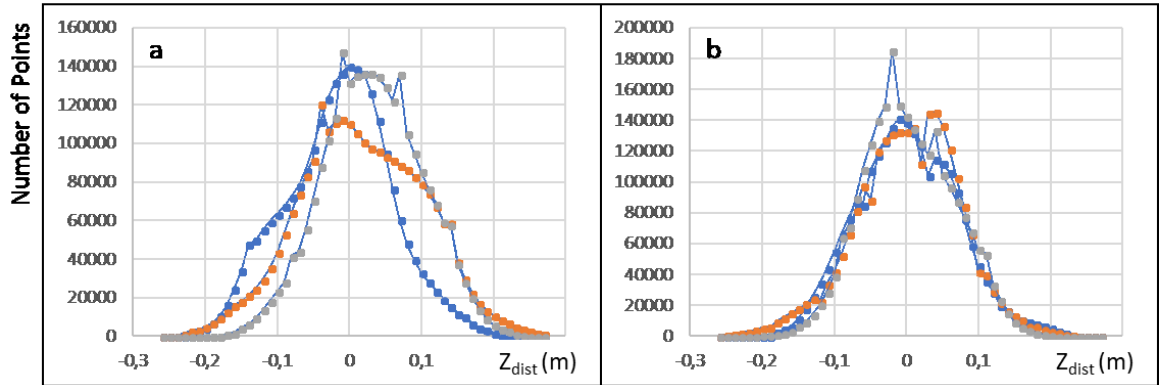


Figure 4.3. SfM survey to SfM survey Z_{dist} scalar field distribution for (a) unregistered and (b) post-SfM registered point clouds. SfM Survey pair 11-12 is blue, SfM Survey pair 11-13 is orange and SfM Survey pair 12-13 is grey. The distributions were not-significantly different from normal.

Table 4.4. Z_{dist} vector field distribution between unregistered core point clouds.

SfM Survey pairs	11 vs 12	11 vs 13	12 vs 13	Average
Mean Z_{dist} (m)	0.016	0.015	0.030	0.020
Standard error of Z_{dist} (m)	0.000	0.000	0.000	0.000
Standard deviation of Z_{dist} (m)	0.074	0.070	0.087	0.077
RMSE of Z_{dist} (m)	0.076	0.089	0.076	0.080
RMSE:range ratio	1:1149	1:986	1:1155	1:1087

SfM Survey pairs	11 vs 12	11 vs 13	12 vs 13	Average
Mean Z_{dist} (m)	0.016	0.015	0.030	0.020
Standard deviation of Z_{dist} (m)	0.074	0.070	0.087	0.077
Standard error of Z_{dist} (m)	0.000	0.000	0.000	0.000
RMSE of Z_{dist} (m)	0.076	0.089	0.076	0.080
RMSE:range ratio	1:1149	1:986	1:1155	1:1087

Table 4.5. Z_{dist} vector field distribution between post-SfM registered core point clouds.

SfM Survey pairs	11 vs 12	11 vs 13	12 vs 13	Average
Mean Z_{dist} (m)	0.000	0.000	0.000	0.000
Standard error of Z_{dist} (m)	0.000	0.000	0.000	0.000
Standard deviation of Z_{dist} (m)	0.070	0.073	0.064	0.069
RMSE of Z_{dist} (m)	0.070	0.073	0.064	0.069
RMSE:range ratio	1:1240	1:1188	1:1363	1:1260

SfM Survey pairs	11 vs 12	11 vs 13	12 vs 13	Average
Mean Z_{dist} (m)	0.000	0.000	0.000	0.000
Standard deviation of Z_{dist} (m)	0.070	0.073	0.064	0.069
Standard error of Z_{dist} (m)	0.000	0.000	0.000	0.000
RMSE of Z_{dist} (m)	0.070	0.073	0.064	0.069
RMSE:range ratio	1:1240	1:1188	1:1363	1:1260

Table 4.6. Instrument error for a sUAV-SfM survey-to-sUAV-SfM survey calculations.

List of instrument errors	Results per survey			Average
	Survey 11	Survey 12	Survey 13	
Single SfM survey				
Camera to UAV GPS 1 error* (m)	0.010	0.010	0.010	0.010
UAV GPS1 to Land GPS error (m)	0.027	0.013	0.017	0.019
Land GPS to vertical datum error (m)	0.006	0.006	0.017	0.009
Ice GPS1 to sea-level error* (m)	0.010	0.010	0.010	0.010
Ice GPS1 to Land GPS error* (m)	0.010	0.010	0.010	0.010
Single SfM survey instrument source of error (m)	0.033	0.022	0.030	0.028
Survey pair instrument source of error (m)	0.046	0.032	0.042	0.040

*Estimated values

4.2 Mapping sea-ice topography

4.2.1 Elevation maps

The elevation maps (i.e. DEM images) for SfM Surveys 11, 12 and 13 (Figure 4.4) display three distinctive topographical features: rubble ice, a pressure ridge and undeformed, level ice. Elevations are relative to the dynamic sea-level, and therefore represents the freeboard elevation. The tidal height increased by 3.0 m between SfM Survey 11 and 12, and by 2.7 m between SfM Survey 12 and 13. The sea-ice ridge can be clearly distinguished on all the point clouds despite its small size and low prominence above the surrounding level ice, with approximate elevations of 30 cm for the level ice and 55 cm for the ridge (25 cm prominence). From the elevation maps, there are no indications of topographical changes occurring at the ridge or on level ice. The rubble-ice area displays metre-scale vertical movement and can be observed going from resting on the sea-floor (SfM Survey 11) to floating (SfM Survey 13) in response to a 5.7 m tide between surveys as measured by Ice GPS1 and 2. The rubble ice appears to drop in elevation relative to the level ice between surveys due to the sea-level-based vertical datum. The surface texture of the undeformed sea-ice area is observable in Figure 4.5, which shows topographical details of small features, such as snowmobile tracks or a fracture in the ridge's centre and snow drifts.

In general, the elevation maps do not present significant quality issues, as the point elevations are generally consistent with visual observations made on the ground. There are no noticeable tilts and the relief is representative of reality. However, there were some errors, notably in areas where the surface elevation was below sea-level. The

errors were more pronounced in SfM Surveys 11 and 12 than for Survey 13 which had 7%, 11% and 1% of their total surface area with negative elevations. The distribution of the affected points was restricted to a 100 to 200 m long patch near the southwestern end of the survey area (Figure 4.4a and b). The shape of these patches was very similar between SfM Surveys 11 and 12, which suggests that the underlying cause of the error is common to all surveys. This is explored further in Section 4.2.3.

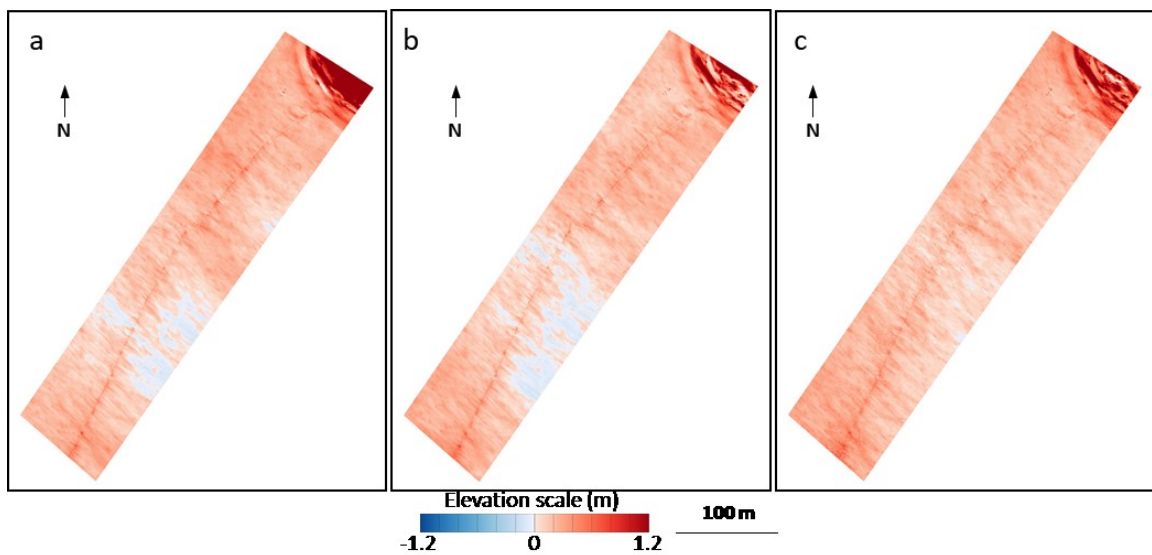


Figure 4.4. Elevation maps of the cropped core point clouds of SfM Surveys 11 (a), 12 (b) and 13 (c). Similarities (ridge) and differences (elevation of the rubble ice area and extent of below-sea-level elevation areas) can be observed between the SfM surveys.

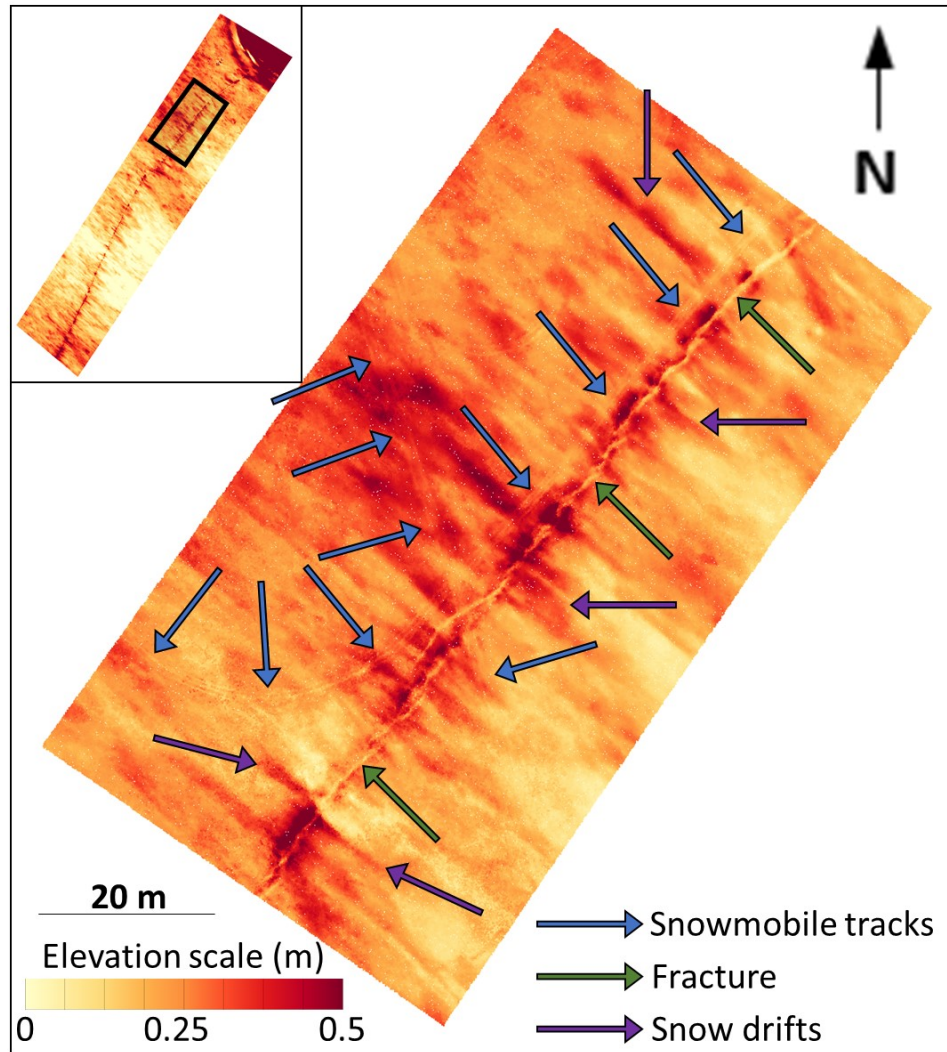


Figure 4.5. Elevation map close-up from SfM Survey 11.

Faint topographical details can be observed, such as snowmobile tracks, a fracture in the ridge's centre and snow drifts. Note that a different colour scale from Figure 4.4 was used to highlight elevation differences. The inset map shows the complete survey area and close-up area for reference.

The expedient method used for SfM Survey 14 (no GCPs and only two rows of images) seemed to have caused some localized data quality issues that are visible on the corresponding elevation map (Figure 4.6.). Since no GCPs were used, the elevation of

the ice surface was derived solely from the tide-corrected camera positions. When compared with Figure 4.4, which uses the same elevation colour scale, coarser results can be observed, such as wavier topography and a generalized tilt seemingly hinged to the ridge (exemplified by the numerous areas with below sea-level elevations to the southeast of the ridge). Despite these issues, features such as snow drifts and the ridge remain easily discernible, and the ridge elevation is remarkably constant despite the large area over which the survey was conducted and the absence of GCPs. Also, at the southernmost extreme of the ridge, the ridge prominence weakens progressively until it disappears, which matches ground observations.

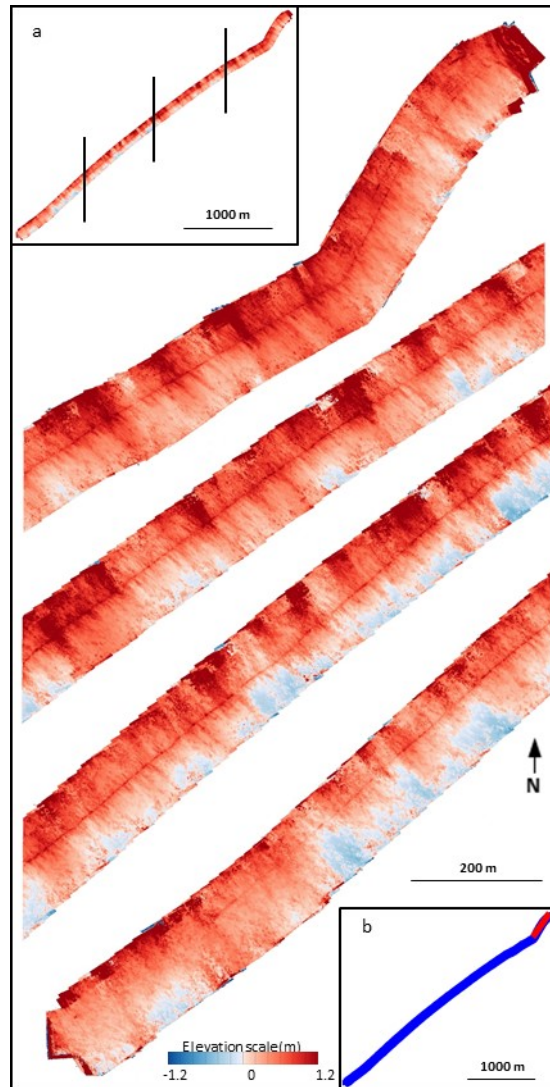


Figure 4.6. Elevation map of the entire length of the ridge (SfM Survey 14 – a and b).

Inset map (a) displays the entire point cloud, with black lines indicating where the cuts were made on the main figure. Inset map (b) shows the extent of SfM Survey 14 (blue) along with the extent of SfM Surveys 11 – 13 (red). Survey 14 was conducted to test an expedient method of surveying large-scale ice features, such as ridges. The entire length of the ridge (4 km) was surveyed with two linear sub-surveys conducted, one on each side of the ridge.

4.2.2 Maps of sea-ice changes

Z_{dist} maps calculated from the core point clouds of each Survey pair 11-12, 11-13 and 12-13 (Figure 4.7) displayed what appears to be a combination of vertical repeatability errors and topographical changes. The SfM survey pairs are presented in both unregistered and post-SfM registered versions. The ridge and rubble ice were dynamic areas where topographical change was expected, while the level ice areas were assumed to have remained static (relative to sea-level) between the SfM surveys. The darker red and blue areas therefore indicate the intensity and direction of the vertical error between surveys. There are very few differences between the maps of post-SfM registered data (Figure 4.7d-f) and their counterparts with unregistered data (Figure 4.7a-c) indicating that the SfM surveys already had a high level of alignment prior to post-SfM registration.

Apparent downward movement is clearly visible for the rubble ice area, which is consistent with the influence of the tidal cycle. For SfM Survey pairs 11-13 and 12-13, a faint depression is visible along the ridge area (Figure 4.8), which, indicates a relative topographical change at high tide. For SfM Survey pair 12-13, a $250 \text{ m} \times 4 \text{ m}$ area along this depression had a mean Z_{dist} of $12.5 \pm 0.2 \text{ mm}$ (standard error – SE), while reference areas on each side of the depression had a mean Z_{dist} of $15.7 \pm 0.3 \text{ mm}$ (SE). Therefore, the ridge deflated between Survey 12 and 13 by an average $3.2 \pm 0.7 \text{ mm}$ (95% CI).

The spatial distribution, spatial scale and the shape of the errors in the level ice areas in Figure 4.7 do not appear to be random. Instead, they are patchy, with affected

areas of approximately $33\text{ m} \times 22\text{ m}$ aligned in a grid. Since this patch size matched the dimensions of the grid pattern formed by the overlapping images of the SfM surveys, the two were compared visually (Figure 4.9). A strong association is visible between the image grid and the vertical errors which suggests that these errors are systematic, with image alignment issues likely to be the root cause.

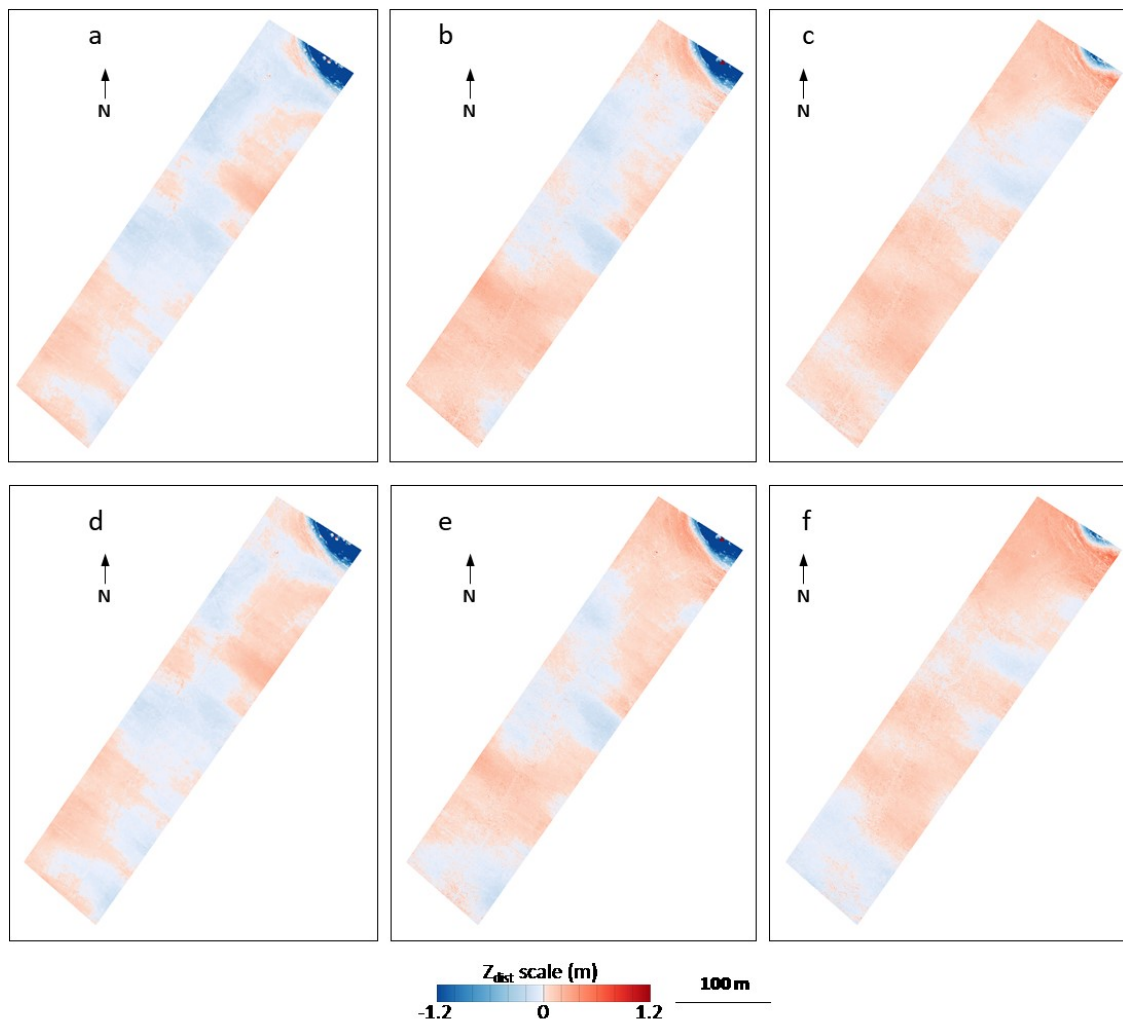


Figure 4.7. Z_{dist} between SfM survey pairs.

The SfM Survey pairs 11-12 (a)(d), 11-13 (b)(e) and 12-13 (c)(f) each had their Z_{dist} calculated twice, without registration (a to c) and with registration (post-SfM) (d to f). Negative Z_{dist} values are represented in blue and indicate a downward movement between successive SfM surveys.

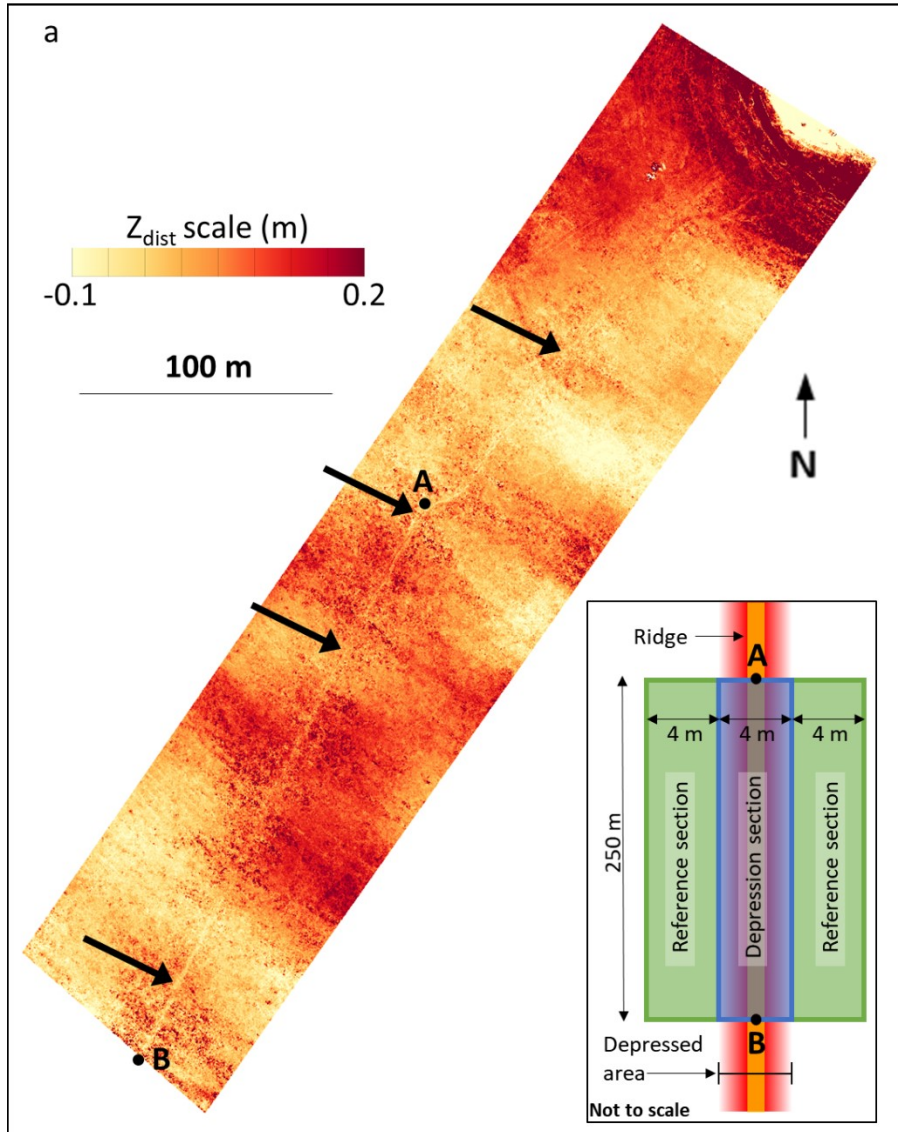


Figure 4.8. Z_{dist} map of SfM Survey pair 12-13.

The colour scale was adapted to highlight a 4 m wide area of downward movement detected along the ridge (indicated with black arrows). Marker A and B denote three 4 x 250 m sections of the scalar field that were isolated to quantify the magnitude of the change through statistical analysis (insert). The middle section (blue rectangle) was centred directly on the 1 m-wide ridge itself, while the adjacent sections (green rectangles) to the west and east acted as reference Z_{dist} values.

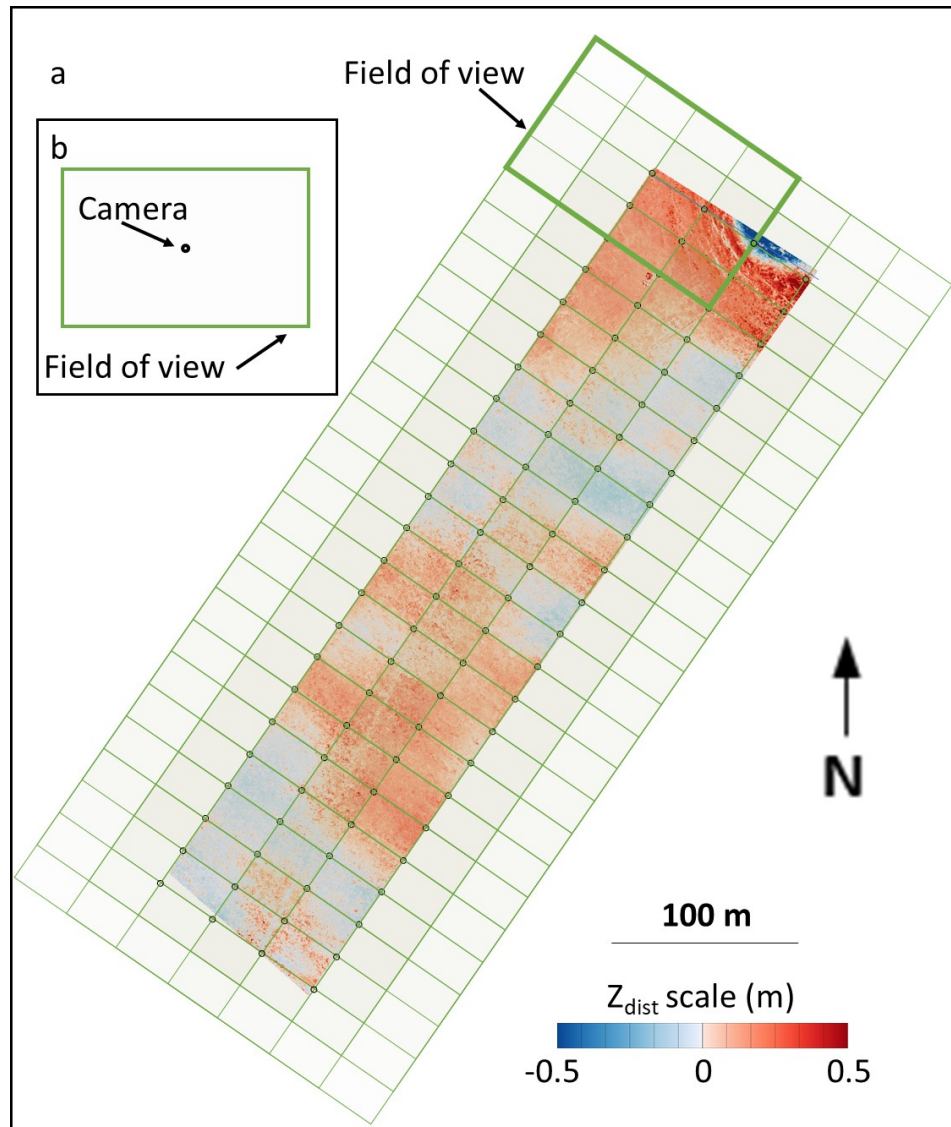


Figure 4.9. Association between point cloud repeatability error and SfM images boundaries.

SfM Surveys 12 and 13 were each composed of 92 images (4 rows of 23 images) with a 75% sidelap and overlap. The camera positions (open circles) were similar for both surveys. The Z_{dist} map between both surveys is overlain with the trace of each image boundary (green lines). Each *grid cell* was imaged in 16 different photos. An example of the field of view from a single image is shown, to scale, in the inset. The pattern of Z_{dist} values appears to be associated with image boundaries since *grid cells* generally appear to be either completely red or completely blue. This association suggests image alignment issues may contribute to this systemic error.

4.2.3 Orthophotos and transects

The visual inspection of the orthophotos revealed that other ice features were detectable with the point cloud elevation maps in addition to the topographical features. Melt ponds, fractures and snow were all easy to identify from the orthophoto (Figure 4.10).

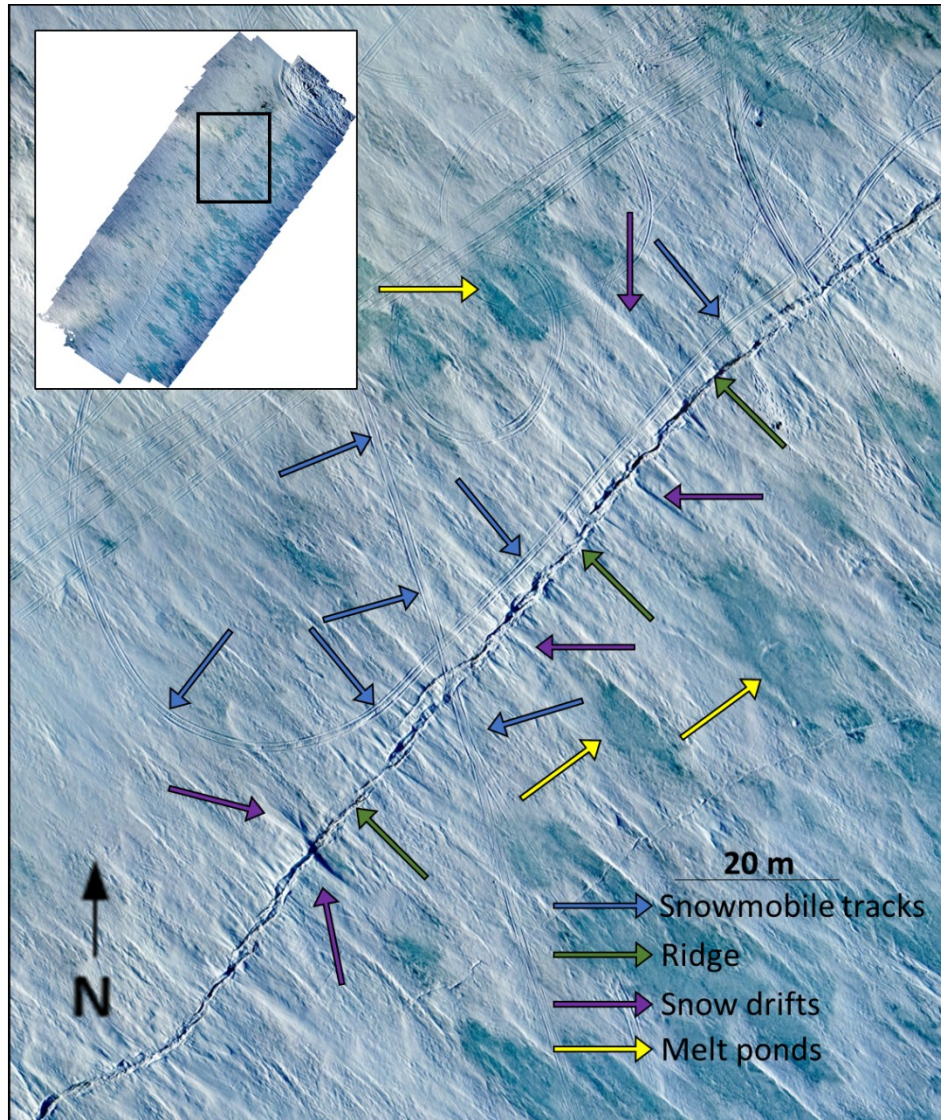


Figure 4.10. Orthophoto of the sea-ice surface from SfM Survey 11.

The area displayed is the same as for the elevation map in Figure 4.5. As in Figure 4.5, multiple topographical features can be observed. In addition, orthophotos can also detect non-topographical features, such as melt ponds, fissures and snow. The inset map shows the complete survey area and close-up area for reference.

Transects of point clouds across the rubble ice area and the related orthophotos (Figure 4.11) provided information about the ice dynamics in the intertidal zone and illustrated how the tides and sea-floor influenced the sea-ice topography. Alignment of elevations along the transect (Survey 11 and 12 between approximately 25 and 70 m on the horizontal axis of Figure 4.11c), indicates an absence of tide-induced movement during the inter-survey period. In contrast, the discrepancy between SfM Survey 13 and the other surveys indicates that all the ice across the transect was floating to some degree. This interpretation is supported by the orthophotos. Although some of the changes between the orthophotos were due to variability in lighting conditions, the effects of the rising tide on the sea-ice is clearly discernible: the ice became progressively flatter, water ponds gradually appeared, and the width of ice fractures changed.

Some of the data artifacts along the point cloud transect, such as underwater ice surfaces (SfM Surveys 12 and 13) and topographic inconsistencies between surveys (SfM Survey 12 between 60 and 65 m on the horizontal axis), could be difficult to interpret based on the point cloud data alone. However, the orthophotos enable a better interpretation. The underwater ice surfaces on the point cloud transect may correspond to the bottom of water ponds visible on the orthophotos since SfM is able to resolve submerged surfaces through an air-to-water interface (Lane et al., 2010). A possible explanation for the inconsistent topography between surveys is that the rising tide may slightly rotate and shift ice blocks (visible in Figure 4.11 b to d, as width changes in the ice fractures).

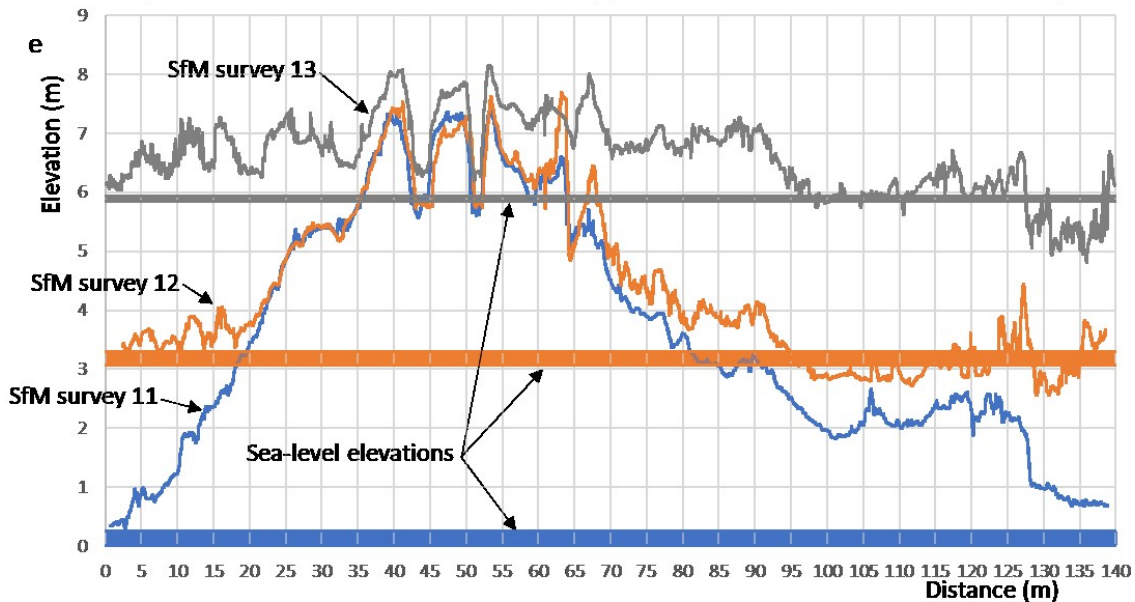
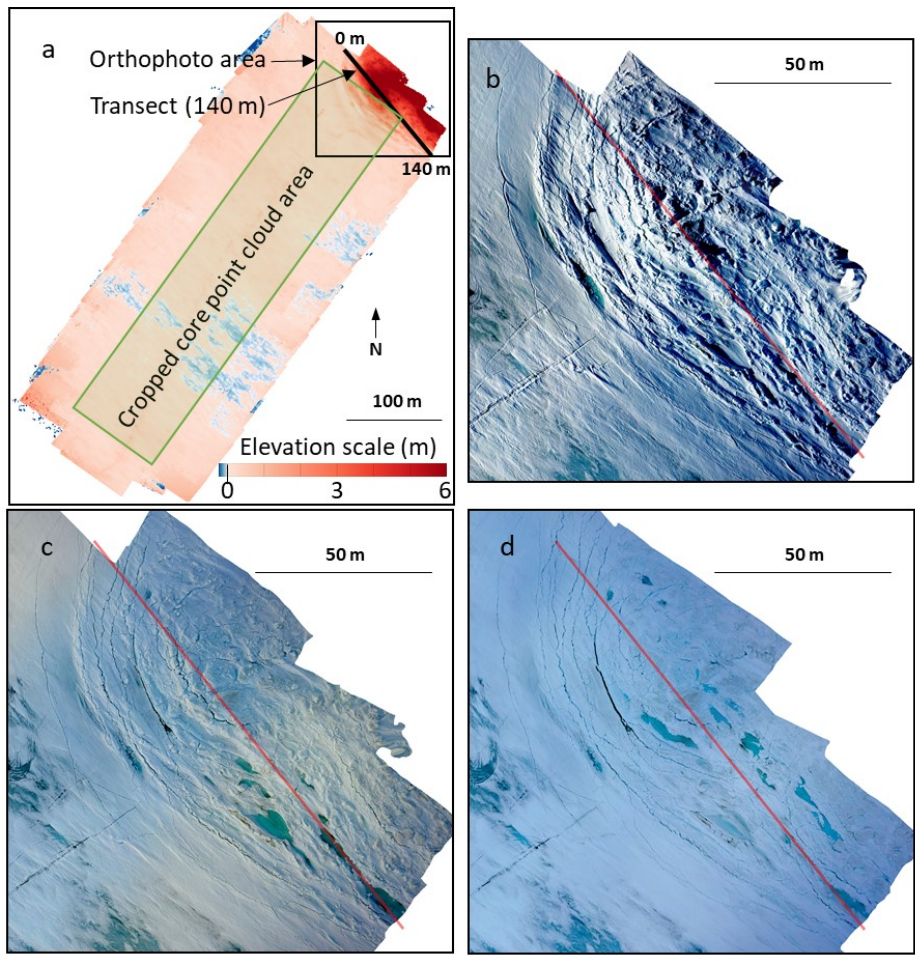


Figure 4.11 (previous page). Elevation along a transect in the rubble ice area for SfM Surveys 11, 12 and 13.

(a) The location of the 140 m transect relative to the uncropped point cloud (SfM Survey 11 displayed here). The uncropped core point clouds were used since the cropped point clouds had minimal rubble ice areas available. (b, c and d) Orthophotos of the rubble ice from SfM Surveys 11, 12 and 13, respectively, with the transect position indicated in red. (e) The elevation along the three transects, adjusted to an arbitrary land-fixed vertical datum, displaying both the topography and the relative elevation for each SfM survey (blue is SfM Survey 11, orange is SfM Survey 12 and grey is SfM Survey 13). The thickness of the sea-level elevation line is representative of the vertical movement of the sea-level during the conduct of each SfM survey.

4.3 Operational performance of sUAV-SfM

4.3.1 Reliability

The GPS receivers, the camera and the UAV were operational throughout the fieldwork and therefore had an equipment reliability ratio of 100%. Only preventative maintenance was required on the UAV. Severe cold temperatures ($< -20\text{ }^{\circ}\text{C}$), which were expected to affect battery performances, were not encountered during fieldwork. Daily mean temperatures of -6.3 , -4.6 , -0.5 and 4.6°C were encountered on the 10, 11, 13 and 16 May, respectively. The UAV batteries, which were kept next to a heat source before and between flights, performed similarly to under temperate climate conditions, therefore the cold was never a limiting factor for SfM surveys.

The flight controller failed to log the flight data for SfM Survey 4. Therefore, UAV attitude data was unavailable to properly calculate the images coordinates, which

made SfM Survey 4 unreliable. With a total of 15 SfM surveying flights (SfM Survey 14 had two flights), the flight controller equipment reliability was 93%.

The Land GPS (*Topcon HiPer V*) reliability maintained a data accuracy of 100% as the vertical accuracies for all the data files ranged from 1.1 to 3.3 cm. Ice GPS1 and 2 reliability sea-level measurements throughout fieldwork are shown in Figure 4.12. Ice GPS1 (*Topcon HiPer V*) data appeared to be accurate, as the plotted curves matched the expected tidal cycle. The estimated reliability of Ice GPS1 is therefore 100%. However, Ice GPS2 (*Emlid Reach*) data appeared unreliable for extended periods of time. A *fix* quality, which represents the highest possible data quality achievable on the unit, did not always coincide with accurate measurements and Ice GPS2 was reliable only 56% of the time (Table 4.7).

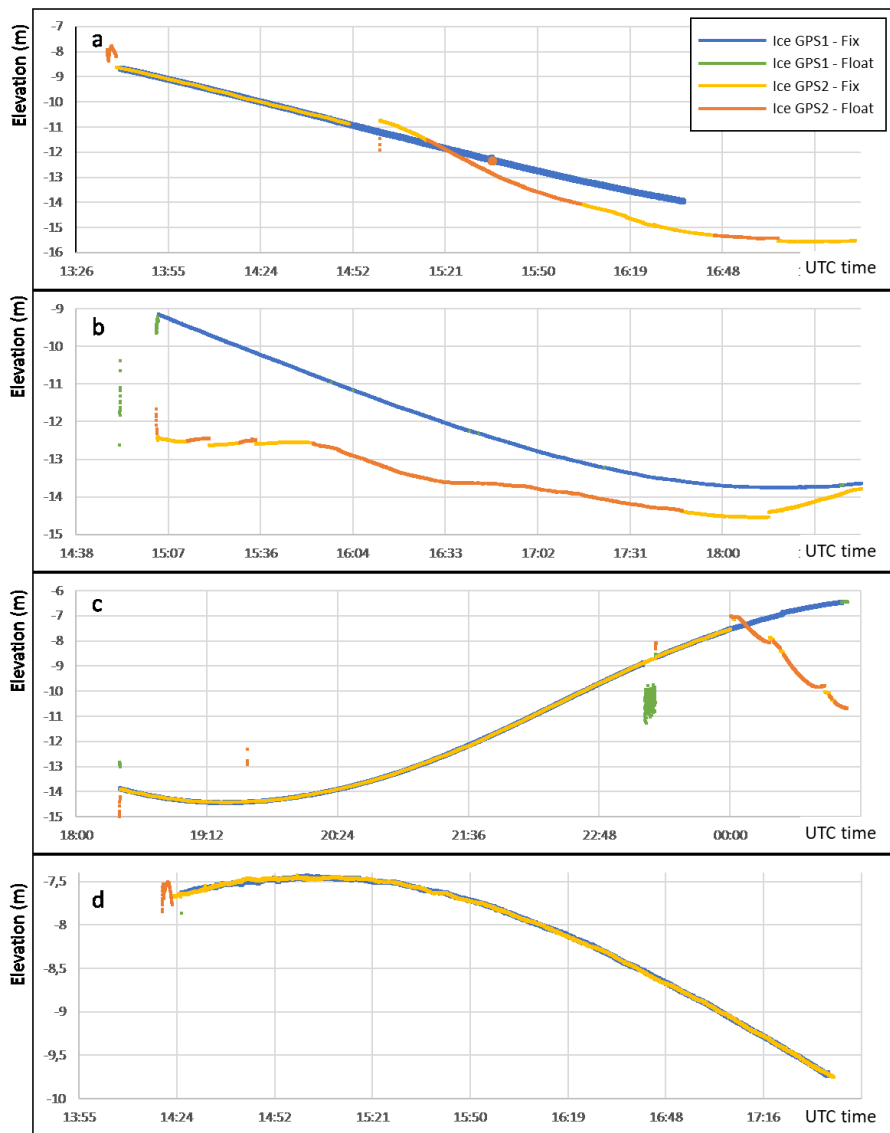


Figure 4.12. Ice GPS1 and 2 reliability for sea-level elevation measurement for the 10th (a), 11th (b), 13th (c) and 16th (d) May.

The Ice GPS1 fixed measurements are representative of tidal motion and are considered to be 100% reliable. Ice GPS2 measurements that differed from Ice GPS 1 were considered to be unreliable.

The vertical movement errors are correlated to horizontal movement errors (not shown here).

Table 4.7. Ice GPS2 reliability.

Reliable time denotes the period during which the sea-level measurements of Ice GPS2 matched the reliable Ice GPS1 data.

Date	Total observation time	Reliable time	Reliability ratio
10 May	03:40:44	01:12:35	33%
11 May	04:18:47	00:00:00	0%
13 May	06:39:33	05:35:30	84%
16 May	03:14:43	03:14:43	100%
Total/Average	17:53:47	10:02:48	56%

Correcting the Ice GPS2 inaccuracies was not successful. Therefore, it was difficult to determine when the receivers returned accurate data. While the Ice GPS2 data could be validated with the Ice GPS1 data (as both were conducting the same measurements), this was impossible with UAV GPS1, since the adjacent UAV GPS2 expected accuracy was at the metre-scale. Therefore, as described in the methods, the analysis of the *Agisoft Photoscan* reports (Figure 4.13.) provided the level of validation required to accept or reject SfM surveys, based on the reported camera positional accuracy (Table 4.8). The camera positions calculated by UAV GPS1 for SfM Surveys 1, 2, 3, 9 and 14 were found to be unreliable. As such, UAV GPS1 had a reliability ratio of 44% (over a total of 9 SfM surveys). A surprising result from the reliability results of Ice GPS2 and UAV GPS1 (whose raw data was processed with PPK in an identical manner), was that the receivers reliabilities were not synchronized. This was exemplified in SfM Survey 13, in which UAV GPS1 was accurate while Ice GPS2 returned inaccurate data. During SfM Survey 14, the opposite occurred.

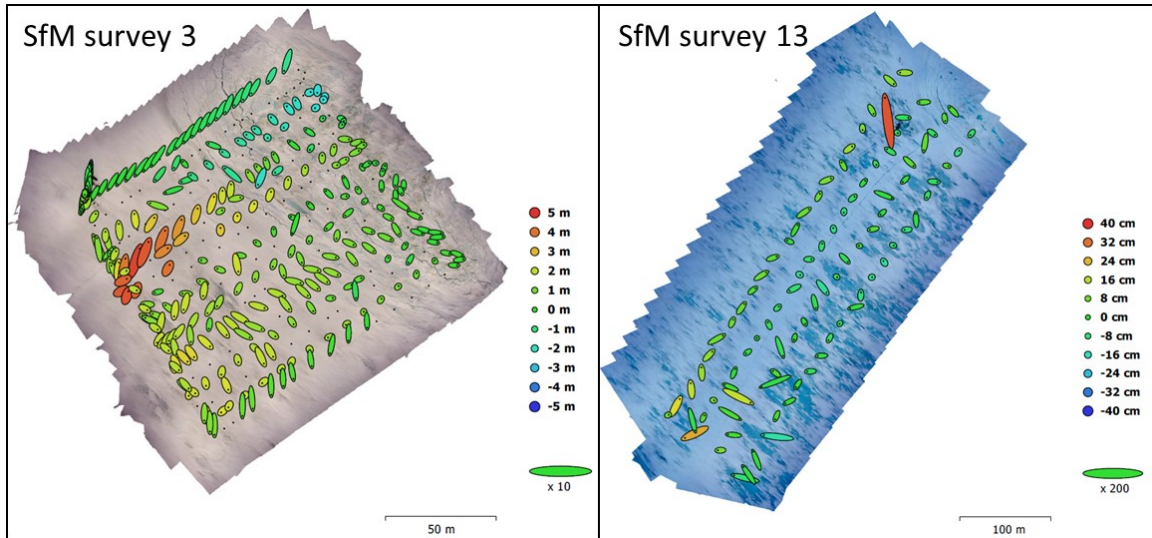


Figure 4.13. Camera location error report from *Agisoft Photoscan* for SfM Survey 3 and SfM Survey 13.

The vertical errors are represented by the colour of the ellipses (different scales for each survey) while the horizontal errors are represented by the ellipse shape, size and scale (also different for each survey). The average camera errors were 1.67 m and 0.10 m respectively for SfM Surveys 3 and 13. As such, the UAV GPS1 data for SfM Survey 3 was considered inaccurate and unreliable, while the opposite was considered for SfM Survey 13.

Table 4.8. UAV GPS1 reliability.

The camera location error was calculated by *Agisoft Photoscan*. UAV GPS1 data was considered reliable when the total camera location error was less than 0.25 m.

SfM Survey	Camera location error (m)			Total	Reliable ?
	X	Y	Z		
1	0.198	0.305	0.871	0.944	No
2	0.318	0.342	1.278	1.361	No
3	0.254	0.449	1.593	1.675	No
9	0.142	0.183	0.238	0.332	No
10	0.115	0.142	0.097	0.207	Yes
11	0.110	0.150	0.106	0.214	Yes
12	0.070	0.103	0.074	0.145	Yes
13	0.044	0.045	0.082	0.103	Yes
14	0.480	0.354	0.170	0.620	No

Image timestamping by UAV GPS1 failed numerous times for SfM Surveys 1 to 4 and 10 (Table 4.9). The timestamping reliability ratio was 89% for the 3572 images captured, and 64% for the 14 SfM surveys conducted. For these issues, the *Emlid Reach* GPS receivers were considered unreliable, and of all the SfM surveys processed, only SfM Surveys 11, 12 and 13 were considered sufficiently viable (Table 4.10) to be used in the analysis.

Table 4.9. Timestamping reliability of UAV GPS1.

The reliability was calculated in two different manners; by the percentage of images with a timestamp and the percentage of SfM surveys with a timestamp for every image.

SfM Survey	Quantities of:			Reliability	
	Images	Timestamps	Missing timestamps	%	Absolute
1	376	311	65	83%	No
2	385	313	72	81%	No
3	379	250	129	66%	No
4	411	336	75	82%	No
5	282	282	0	100%	Yes
6	372	372	0	100%	Yes
7	183	183	0	100%	Yes
8	145	145	0	100%	Yes
9	92	92	0	100%	Yes
10	92	51	41	55%	No
11	92	92	0	100%	Yes
12	92	92	0	100%	Yes
13	92	92	0	100%	Yes
14	579	579	0	100%	Yes
Total	3572	3190	382	89%	64%

Table 4.10. Equipment and data reliability summary.

SfM survey	Equipment reliability							Data reliability						Viable SfM survey?
	Land GPS1	Ice GPS1	Ice GPS2	UAV GPS1	Camera	UAV	Flight controller	Land GPS1	Ice GPS1	Ice GPS2	UAV GPS1			
											SfM report	Timestamp %	Timestamp absolute	
1	100%	100%	100%	100%	100%	100%	100%				0%	83%	0%	No
2	100%	100%	100%	100%	100%	100%	100%				0%	81%	0%	No
3	100%	100%	100%	100%	100%	100%	100%	100%	100%	33%	0%	66%	0%	No
4	100%	100%	100%	100%	100%	100%	0%				N/A	82%	0%	N/A
5	100%	100%	100%	100%	100%	100%	100%				N/A	100%	100%	N/A
6	100%	100%	100%	100%	100%	100%	100%				N/A	100%	100%	N/A
7	100%	100%	100%	100%	100%	100%	100%	100%	100%	0%	N/A	100%	100%	N/A
8	100%	100%	100%	100%	100%	100%	100%				N/A	100%	100%	N/A
9	100%	100%	100%	100%	100%	100%	100%				0%	100%	100%	No
10	100%	100%	100%	100%	100%	100%	100%				100%	55%	0%	No
11	100%	100%	100%	100%	100%	100%	100%	100%	100%		100%	100%	100%	Yes
12	100%	100%	100%	100%	100%	100%	100%			84%	100%	100%	100%	Yes
13	100%	100%	100%	100%	100%	100%	100%	100%	100%		100%	100%	100%	Yes
14	100%	100%	100%	100%	100%	100%	100%	100%	100%	100%	0%	100%	100%	No
Total	100%	100%	100%	100%	100%	100%	93%	100%	100%	56%	44%	89%	64%	44%

None of the processed point clouds contained visible gaps which implies that the sUAV-SfM data was reliable enough for low-contrast surface reconstruction. The ratio of image data density per point (Table 4.11) indicates a similar reliability to generate points between surfaces of differing contrast. For example, SfM Survey 14, which had the lowest surface contrast, had similar values to other SfM surveys. While numerous surveying parameters can affect these values, the results indicate that low contrast surfaces did not appear to be an important issue for point generation.

Table 4.11. SfM survey resolution indicators.

The highlighted results represent the highest and lowest values for each indicator. The high contrast and low contrast surfaces of SfM Surveys 11 and 14 respectively did not generate anomalous values, which indicates that the low contrast surfaces were not a significant issue in these surveys.

SfM Survey	Images				Point clouds			Resolution indicators	
	Resolution per pixel (cm)	Resolution per m ² (pixels/m ²)	Effective overlap *	Effective pixels per m ² † (pixels/m ²)	Raw area (m ²)	Points per area (points/m ²)	Pixels per point ‡	Effective pixels per point §	
	1	1.0	9 803	14.9	146 106	113 486 422	34 700	3 271	3.0
2	0.8	17 730	10.9	193 411	165 647 460	27 900	5 937	3.0	32.6
3	0.8	17 222	13.3	228 710	158 259 191	27 600	5 734	3.0	39.9
9	1.9	2 770	6.2	17 239	91 268 259	106 000	861	3.2	20.0
10	2.1	2 268	6.7	15 254	81 637 414	119 000	686	3.3	22.2
11	2.1	2 289	7.1	16 232	82 503 749	119 000	693	3.3	23.4
12	2.1	2 246	5.7	12 860	81 524 960	118 000	691	3.3	18.6
13	2.1	2 246	4.4	9 919	80 386 320	127 000	633	3.5	15.7
14	2.0	2 475	5.4	13 473	485 271 017	636 000	763	3.2	17.7

* The *Effective overlap* indicates the average number of times a surveyed location was captured by an image during the survey. The values were provided by the SfM reports from *Agisoft Photoscan*.

† The *Effective pixels per m²* is the product of the *Resolution per m²* and the *Effective overlap*. The values reflect the total number of pixels captured by the camera (including overlapping pixels) per every square metre of the raw survey area.

‡ The *Pixels per point* values were calculated by dividing the *Resolution per m²* by the *Points per m²*. It indicates the ratio between the ground resolution and the raw point cloud density.

§ The *Effective pixels per point* is the result of the division of the *Effective pixels per m²* by the *Points per m²*. The values indicates the total sum of distinct image pixels from multiple images required to generate a single point in the raw point cloud.

4.3.2 Surveying and processing speed

The time required for the sUAV-SfM surveys and data-processing (Table 4.12) varied significantly between SfM surveys. The most significant difference between surveys was the processing times: SfM Surveys 1 to 3 required significantly longer processing times per unit area (up to 110 times more) and per point (up to 27 times more) than SfM Surveys 9 to 14. The most substantial surveying parameter differences between

these survey groups were the overlap and sidelap ratios (0.875 for SfM Surveys 1 to 3 and 0.75 for SfM Surveys 9 to 13). These values corresponded to an effective overlap of 64 (i.e. every point in this area was captured by 64 different images) in the cropped surveying area for SfM Surveys 1 to 3, compared to 16 for SfM Surveys 9 to 13. This large difference between effective overlap may have generated the computing bottlenecks shown in Table 4.12.

Table 4.12. Surveying and processing speeds.

The survey times represented the flight time of the UAV for each survey. The processing times were obtained through the SfM reports generated by *Agisoft Photoscan*. The highest and lowest values for each of the speeds are highlighted in grey, and the ratio between these values were calculated. For most of the speeds, SfM Surveys 1 to 3 values differs significantly from SfM Surveys 9 to 14.

SfM Survey	Raw area (m ²)	Images	Raw points	Maximum effective overlap	Survey time (min)	Processing time (min)	Surveying time speed (per sec)			Processing time speed (per sec)		
							Raw area (m ²)	Images	Raw points	Raw area (m ²)	Images	Raw points
1	34 700	376	113 486 422	64	13	1286	44	0.48	144 938	0.4	0.005	1 471
2	27 900	385	165 647 460	64	14	601	32	0.45	191 722	0.8	0.011	4 595
3	27 600	379	158 259 191	64	13	577	35	0.48	202 377	0.8	0.011	4 571
9	106 000	92	91 268 259	16	16	38	112	0.10	96 682	47	0.04	40 153
10	119 000	92	81 637 414	16	9	42	217	0.17	148 702	47	0.04	32 319
11	119 000	92	82 503 749	16	10	41	194	0.15	134 371	48	0.04	33 241
12	118 000	92	81 524 960	16	8	42	255	0.20	176 080	47	0.04	32 506
13	127 000	92	80 386 320	16	14	43	156	0.11	98 876	49	0.04	31 182
14	636 000	579	485 271 017	18	41	361	258	0.24	197 104	29	0.03	22 375
Ratio between highest and lowest value							8	5	2	110	8	27

4.3.3 Simplicity

The fieldwork preparation was relatively lengthy and complicated. In terms of equipment, the customized UAV and a purpose-built SfM payload were difficult to integrate. Iterative modifications to the camera, the high-precision UAV GPS receiver

and the UAV flight controller were required, as each of the originally selected components, consisting of the proprietary *DJI* flight controller, a *Samsung NX 2000* camera and a *Swift Navigation Piksi* GPS receiver, were found to be incompatible with one another. The equipment preparation required an estimated 250 hours of work. For UAV regulations, the *Pilot Ground School Program* certification required by Transport Canada for all UAV research flights also added to the fieldwork preparation time and complexity. This certification, requiring approximately 75 hours to complete, was required for an SFOC exemption (thus avoiding the need for an SFOC request (Transport Canada, 2018b), which would have required additional time and work and risked being refused by the authorities).

The sUAV-SfM surveys themselves were relatively simple and fast to conduct. The setup of the Land and Ice GPS receivers and the placement of the GCP markers was straightforward, as was the generation of the flight plan and transfer to the UAV. The UAV flights and the ground surveys of the GCPs were also relatively simple to conduct.

Data-processing was initially complex due to the customized scripts and calculations required to include the ice movements offsets between the camera and UAV GPS1. The subsequent processing in *Agisoft Photoscan* and *CloudCompare* were relatively straightforward. The post-processing steps between the raw data assimilation and the core point cloud production became increasingly rapid as the thesis work progressed through a combination of enhanced user experience and the automation of some of the workflow. A current impediment to very fast fieldwork-to-point cloud

processing times were the week-long delays for the highest accuracy GPS corrected products to be available for PPP and PPK accuracy augmentation (satellite ephemerides, clocks, etc), but this high accuracy positioning is less critical if the absolute position of the ice is not required.

4.3.4 Costs

The cost of the equipment is provided in Table 4.13. The costliest pieces of equipment belonged to the *shared usage items* category, with the two high-end GPS receivers accounting for over 45% of the total cost. However, since items in this category would not typically be purchased strictly for SfM surveying, the estimated cost of conducting SfM surveys similar to those in this thesis is \$6000.

Table 4.13. Cost estimate for the equipment, training and license required to conduct and process sUAV-SfM surveys.

The *exclusive usage items* category contains items expected to be purchased and used for dedicated sUAV-SfM surveys for a typical user, while the *shared usage items* category indicates items expected to be available via rental or on loan. This cost estimate is chiefly based on the set up for this research. Note that these techniques are in rapid development and new sUAV platforms, cameras and software at various price-points are becoming available on the market.

Exclusive usage items	
Items	Costs
UAV*	2 000.00 \$
Radio controller*	430.00 \$
UAV batteries (x8)*	500.00 \$
Battery chargers	220.00 \$
Flight controller	150.00 \$
Low-cost, PPK-able GPS receivers (x2)	710.00 \$
Camera	780.00 \$
Camera cables	160.00 \$
UAV pilot certification	300.00 \$
SfM software license (academic)	750.00 \$
Sub-total	6 000.00 \$
Shared usage items	
Items	Costs
High-end GPS receivers (x2)*	10 000.00 \$
Field laptop*	2 000.00 \$
High-end desktop*	4 200.00 \$
Sub-total	16 200.00 \$
Grand total	22 200.00 \$

*Estimated costs

5 Discussion

5.1 Accuracy, precision and repeatability

5.1.1 Accuracy and precision

SfM Surveys 1-3 and the ground survey on May 10th were designed to assess SfM accuracy and precision. However, due to GPS data quality issues on that day, SfM Surveys 11-13 on May 13th replaced SfM Surveys 1-3 for this purpose instead. The three-day time gap between the reference ground survey and SfM Surveys 11, 12 and 13 likely affected the outcome of the accuracy and precision determination. The surface conditions went through two types of change within this period. Footsteps made in the snow during the ground survey depressed the surface next to most measurement points to a depth of millimetres to centimetres. Spring weather and clear skies between the surveys also partially melted the snow cover on the sea-ice surface. These changes are unquantified, but it can be assumed that, overall, the surface elevation was reduced. The mean Z_{dist} values calculated between the ground survey and the SfM surveys were positive, signifying that the average SfM surface elevations were lower than the ground survey. It is likely that some fraction of these mean Z_{dist} values represent an element of change due to melt and anthropogenic disturbance. The main consequence of this is that the calculated SfM accuracy and precision values may be underestimated (i.e. the error values are overestimated) at the positions surveyed by the ground survey.

Spatial conditions also affected the accuracy and precision calculations (Figure 5.1). As demonstrated by the spatial distribution of the repeatability errors (Figure 4.9), spatial scale had an impact on the homogeneity of the error distribution, specifically at

the scale of the *grid cells* formed by the overlapping image boundaries (i.e. there is a spatial scale at which the spatial distribution of the error displays a clear pattern).

Because the *grid cells* matched an error pattern observed on point cloud-to-cloud Z_{dist} maps, the error distribution within a single *grid cell* is likely to be more homogenous than between different *grid cells*. Therefore, the spatial distribution of the ground survey requires measurements across multiple *grid cells* to be highly representative.

Considering that only five out of 63 *grid cells* were sampled during the ground survey (and four were only partially sampled), the ground survey should not be considered representative of accuracy and precision over the whole area (Figure 5.1).

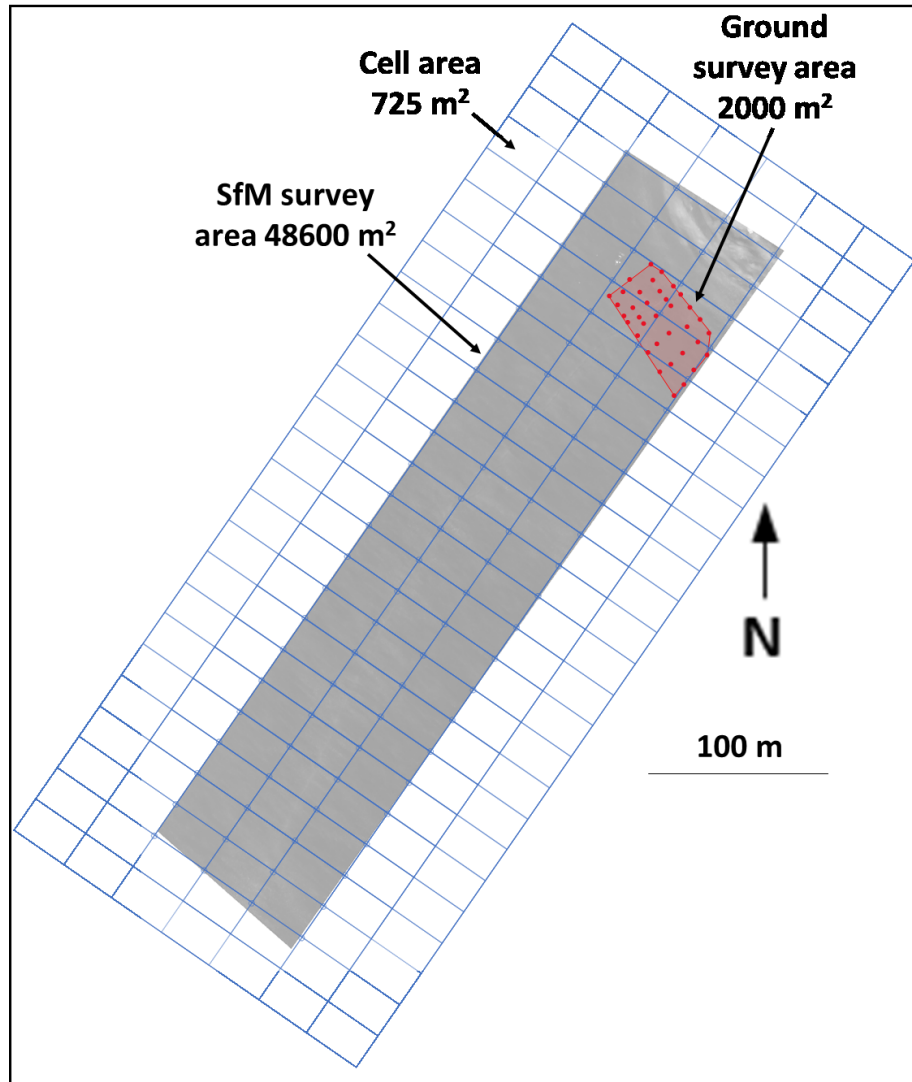


Figure 5.1. Spatial distribution of the ground survey compared with a cropped core point cloud area (SfM Survey 13 shown here) and the SfM image boundaries grid. As with Figure 4.9, the SfM images were overlapping and side lapping with a ratio of 0.75, therefore, the resulting image boundary grid was composed of *grid cells* with 1/16th of the area of a single image. The ground survey points were distributed across only five *grid cells*. This poor spatial distribution resulted in a low representativeness for the ground survey of the entire area.

Published values for typical SfM RMSE:range ratios are between 1:625 and 1:1000 (Eltner et al., Smith et al., 2016). This corresponds to an RMSE of 87 to 140 mm at the altitude flown during this study, which is close to the mean accuracy value of 69 mm obtained herein. While not representative of the full SfM survey area, the mean RMSE value of 69 mm is representative of the immediate area surrounding the ground survey for SfM Surveys 11, 12 and 13. With a mean RMSE:range ratio of 1:1265, this specific section of SfM Surveys 11, 12 and 13 outperforms the commonly cited RMSE:range ratios by 27% to 102%, which is an impressive result. Furthermore, since the calculated mean RMSE value are likely overestimated by melting and surface disturbances, it is reasonable to assume that the actual value for the calculated RMSE:range ratio could even be lower (i.e. the range value would be even higher than the RMSE).

However, due to the uncertainty generated by the poor overlap between the compared SfM and ground surveys, it is estimated that the accuracy of sUAV-SfM to survey sea-ice would be represented at a higher confidence level by a more conservative RMSE:range ratio of 1:1000, as this ratio is known to be achievable by SfM according to published results. Once converted, this RMSE:range ratio represents a RMSE value of approximately 87 mm. Although this value cannot be separated into distinct mean and standard deviation values, it still provides a range within which these values are likely to be. Furthermore, the initially anticipated difficulties associated with UAV-borne SfM surveying of sea-ice, such as low surface contrast and ice movements, did not end up having a measurable impact on the quality of the results, considering a RMSE:range ratio

of 1:1000 is better than most SfM surveys conducted over easier-to-survey stationary and high-contrast landscapes (Eltner et al., 2016; Smith et al., 2016).

5.1.2 Repeatability

The repeatability error measures have a more constrained confidence limit than both the accuracy and precision results primarily due to the number of points compared (more than 2 million vs. 66 survey points) and the number of *grid cells* covered (63 cells vs. 5, as per Figure 5.1). Overall, the relatively small differences between the distributions associated with the unregistered surveys and those associated with the post-SfM registered surveys demonstrated a high level of pre-existing registration between unregistered point clouds. This suggests that, for change detection, the post-SfM registration step could be omitted since the loss of precision is not substantial. This is an important finding, since point clouds of flat topographies are difficult to finely register along horizontal axes.

A portion of the repeatability error is considered to be systematic due to shape and size patterns of the patches found in Figure 4.7. The total repeatability error is composed of this systematic error as well as any local surface errors. It follows that, for a nominal total repeatability error value, the local surface quality error value will be inversely proportional to the systematic error value. By ignoring (as much as possible) the systematic errors, which is feasible when the systematic error patterns are known, the remaining errors, mostly composed of local surface errors, have a lower amplitude than the overall repeatability error. When doing so, the ability of the technique to detect small

topographical details and local change is even greater than what the repeatability RMSE value would initially suggest. This was demonstrated by Figure 4.6, where despite significant systematic errors visible in the elevation map of SfM survey 14 (a strong tilt of the sea-ice surface model), the local topography near the pressure ridge remained an excellent indicator of the shape and size of the ridge along its full length. Therefore, overall, the accuracy, precision and repeatability values indicate that sea-ice surveying can be conducted with a quality equivalent to that of SfM surveys conducted over static landscapes.

5.2 Sea-ice topography: maps, orthophotos and transects.

The elevation maps demonstrated the ability of SfM to represent fine topographical details of the sea-ice (Figure 4.5) such as snow drifts, snowmobile tracks and shallow ridges. As previously stated, even with significant systematic errors (Figure 4.6), these fine topographical details are clearly distinguishable. Therefore, through visual interpretation, some of the systematic errors can be identified and ignored by the map user, since the local topography was still representative of the true sea-ice topography.

The point cloud-to-point cloud distance maps demonstrated the ability of SfM to not only detect changes visually but also to quantify them. Although the metre-scale changes in the rubble-ice area represented in the maps were expected based on observations made during the fieldwork, the millimetre-scale downward movement (relative to the surrounding sea-ice) during the rising tide detected along the ridge was

too faint to be visually observed during fieldwork. Also, because the effect of tidal movements on the ridge topography was unknown, this localized subsidence was unexpected. The high point density generated by sUAV-SfM and the small-scale footprint of each point made it possible to detect change along a narrow (approximately 4 m) and long feature at the millimetre-scale (with a sub-millimetre confidence interval), in spite of a calculated repeatability value (mean Z_{dist} between point clouds) approximately six times larger than the amplitude of the detected change.

The transect graph enabled the visualisation of the intertidal zone sea-ice topography changes across multiple SfM surveys (Figure 4.11). The interaction between the sea-ice, sea-floor and ocean was discernible while the tide was changing. The location of the hinge point, ponds and ice blocks could all be determined from the transects and the high density of the point cloud enabled fine topographical details to be observed.

The orthophotos also provided useful information about the ice topography and enabled the easy identification of surface cover, such as ice, snow and water (Figure 4.10). When used in conjunction with point cloud maps, they enhanced the interpretation and identification of the topographical features observed with the point clouds. They also enabled the observation of details which would have been difficult to find with point cloud data alone, such as the identification of fractures (Figure 4.11).

Overall, the results for SfM Surveys 11 to 14, in the form of maps, transects and orthophotos provided valuable information about the sea-ice topography and detection of topographical changes associated with the tidal cycle.

5.3 Operational performance

The main operational performance issues that were encountered were the reliability difficulties with the two *Emlid Reach* GPS receivers. The PPK-processed Ice GPS2 data demonstrated that the *Emlid Reach* data, despite reporting *fix* positioning quality indicator (the indication that the carrier phase ambiguity is solved, which should have resulted in centimetre-level accuracy), still had inaccuracies of up to the metre-scale. This made the *fix* or *float* data quality indicators an unreliable predictor of the expected positional accuracy for the *Emlid Reach* data, making it even harder to independently assess the quality of UAV GPS1 data. This highlighted an unexpected advantage of the SfM algorithms, which is the ability to provide an independent measurement of the georeferencing accuracy of the images through the bundle adjustment step and provide some level of corrections to the faulty data. Despite these corrections, unreliable georeferencing of images still generated low point cloud accuracies, as demonstrated with SfM Surveys 1-3, 9, 10 and 14.

However, this level of unreliability is typical for low-cost, single frequency GPS receivers capable of PPK corrections. Jackson et al. (2018), in a review of low-cost GPS receivers including the *Emlid Reach*, stated that the single frequency receivers were not well-suited to dynamic applications. In the same study, the *Emlid Reach*, when paired

with a low-cost GPS antenna and used in RTK mode, had a 30 cm horizontal accuracy (95% CI) and had a *fix* quality 70% of the time when its position remained static, which is sub-optimal when compared with the sub-decimetre level accuracies achievable by sUAV-SfM. When used in a dynamic mode, these values changed to 45 cm and 15% of the time respectively, indicating a significant drop in both quality and value for sUAV-SfM. As such, some of the accuracy and reliability issues with the *Emlid Reach* GPS receivers during fieldwork were typical of the capability of this type of receiver. However, the Jackson et al. study provided no explanations for the unreliability of the *fix* positioning quality indicator.

The remainder of the equipment generally performed as expected and collected reliable data. *Agisoft Photoscan* encountered no discernible issues for generating keypoints and points from the contrast-enhanced images. The speeds at which the sUAV-SfM surveys could be conducted in the field was dependant on the extrinsic and intrinsic camera parameters (e.g. flightpath and focal length). For processing speeds, SfM Surveys 1 to 3 required significantly longer times than the rest of the SfM surveys (Table 4.12). Although the total number of images per SfM survey is known to be correlated to processing times (Schön et al., 2016), SfM Survey 14 required noticeably less processing time despite a higher total number of images than SfM Surveys 1 to 3. However, the most significant factor distinguishing SfM Surveys 1 to 3 from the other surveys was the maximum effective overlap. The effective overlap of 64 was approximately 4 times larger than the effective overlap for SfM Surveys 9 to 14. During the SfM-processing, SfM Surveys 1 to 3 required on average nine times more processing

time than SfM Surveys 9 to 14. Therefore, the most likely explanation for the very long processing times of SfM Surveys 1 to 3 is the high effective overlap, which likely generated computing bottlenecks. Due to the low sample size, an optimal effective overlap could not be estimated.

Difficulties encountered during pre- and post-fieldwork tasks can nearly all be attributed to the research, testing, troubleshooting and workflow optimisation phases for the equipment and data, as it is normally the case for projects of this nature. However, since most of the problems had to be solved only once, subsequent field usage of this technique is expected to be significantly less complex (except for the *Emlid Reach* issues, which have not been resolved yet). Further decreases in complexity are also expected with increased user experience and the optimization of processes. Consequently, the sUAV-SfM survey results are expected to be generated progressively faster as experience increases.

For costs, there is a major benefit of the technique is the minimal operating costs once the equipment, training and licenses have been purchased. This cost structure made calculations such as price per point, or price per area, very challenging to estimate, as they depend on the usage and longevity of the equipment (including the UAV crash rate), which is likely to vary significantly between setups and users. As such, any cost comparisons between techniques would have to consider this particularity.

As for whether the technique could be considered low-cost, for a typical user who has access to high-end GPS receivers and high-end desktop computers, the \$6000 cost estimation for the system used for this thesis is likely to be considered low. As such, sUAV-SfM can be considered a low-cost sea-ice topography surveying technique.

5.4 Comparison to existing techniques

When comparing sUAV-SfM surveys to other techniques, it is important to consider some of the surveying characteristics, such as the relative scale and speed at which surveys are conducted. The centimetre-level ground resolution from a sUAV-SfM survey is so different from hectometre to kilometre-level ground resolution expected from a satellite platform such as CryoSat-2, that they can't be used interchangeably for similar tasks. The long time required to drill a single hole through the sea-ice makes drilling equally uninterchangeable with sUAV-SfM due to the ability of the latter technique to collect hundred of thousands of raw points per second. As such, a comparison between the sUAV-SfM surveying technique and other established techniques is only valuable if conducted between techniques of equivalent outputs. Therefore, I will compare sUAV-SfM with the classic photogrammetry (including stereophotogrammetry), airborne lidar and InSAR techniques.

Classic photogrammetry can be differentiated from SfM (itself a photogrammetric technique) by its requirement to have a well-defined acquisition plan to obtain suitable imagery at appropriate spacing and geometries (Mancini et al., 2013), resulting in higher cost and complexity despite equivalent accuracies (Ely et al., 2016; Thomson and

Copland, 2016; Uysal et al., 2015). Large aerial platforms are required for classic photogrammetry since the flightpath irregularities experienced by sUAVs, especially for low altitude flights, generate processing difficulties (Rango et al., 2009). The only recent use of classic photogrammetry found in the literature for sea-ice surveying was by Divine et al. (2016), which used a dual camera setup (stereophotogrammetry) combined with a laser altimeter and a GPS receiver. With the exception of a 10-parameter camera model developed to account for lens distortion (this is automatically generated by SfM algorithms), workflow very similar to SfM was used to optimize extrinsic camera parameters. Overall, when compared with the results obtained by SfM, there appear to be no single characteristic of classic photogrammetry superior to SfM when applied to sea-ice surveying.

For the comparison with lidar surveying, satellite-based systems and non-scanning (linear) lidars were ignored because of the large differences with sUAV-SfM for footprints size and capture geometry respectively. No cases of sUAV-lidar surveys of sea-ice were found (Bhardwaj et al., 2016a, 2016b), but since the technique is rapidly emerging in the geoscience field (Elaksher et al., 2017) and has the potential to be used for sea-ice topographic mapping it will be incorporated in the analysis. The accuracy of an airborne lidar point cloud depends on the combined accuracies of the lidar, the GPS receiver and the IMUs for every collected point (Elaksher et al., 2017). As such, while the accuracy of the measured distance between a lidar instruments and a surface are generally reported to be around 2 cm, the overall accuracy of an aerial lidar survey will be largely dependant on the GPS and IMUs accuracies (Tulldahl et al., 2015). The tested

accuracy for sUAV-lidar surveys resulted in a vertical RMSE of 5 cm from a UAV elevation above ground of 8 m for Tulldahl et al (2015), while Chiang et al. (2017) reported a 1.07 m RMSE from a UAV elevation of 60 m. The RMSE:range ratios of 1:56 (Chiang et al. 2017) to 1:160 (Tulldahl et al. 2015) compared poorly with sUAV-SfM. For larger aircraft, precision values of 10 cm were reported for the Ice Bridge's Airborne Topographic Mapper (ATM) (Farrell et al., 2011) and CryoVEx's Airborne Laser Scanner (ALS) (Di Bella et al., 2018) from a 500 m altitude, resulting in a high precision over range ratio⁴ (1:5000) which is higher than sUAV-SfM. However, for the speed, density, spatial distribution and footprint of the collected points, the ATM and ALS instruments compare poorly with sUAV-SfM, each collecting points with a 1 m footprint at a 5 to 10 Hz frequency (every 5 m for the ATM, unspecified for the ALS) across a 300 m swath (Farrell et al., 2011; Hvidegaard et al., 2015). Although these specific instruments do not represent the full capabilities of the airborne lidar technique, the typical point density for large aircraft-borne lidar surveys is about 1 point/m², while high density surveys are rarely over 10 point/m² (Kiss et al., 2016)⁵, which is significantly less than the 60 to 6000 point/m² achieved with sUAV-SfM (core point cloud and raw point cloud respectively). For sUAV-lidar surveys, point density values are seldom reported, but equipment with scan rates of 300 000 to 700 000 points per second have been tested (Elaksher et al., 2017), which is relatively equivalent to sUAV-SfM, since only a narrow

⁴ Not an RMSE:range ratio, but it still offers a rough scale of the expected errors.

⁵ Although there are no theoretical limits to how dense an airborne-lidar point cloud can be, flying altitude and laser shot frequency are the general limiting factors (Chu et al., 2014).

angle of all the points fired by these small-form lidar instruments are directed at the ground (Velodyne LiDAR, 2016). However, as demonstrated by Figure 5.2, the distribution of points of these small systems can be very heterogenous, with strong artifacts from the scanning pattern and attitude changes of the sUAV. The cost of lidar payloads ranges from \$5300 for lightweight, short-range (± 100 m) for the *Velodyne VLP-16* (Higgins, 2018), to over \$150 000 for high-end, long-range equipment (Crawford et al., 2018; Shi et al., 2018), but the prices are expected to drop significantly with the emergence of the autonomous automobile and recent breakthroughs with solid-state types of lidar systems (Shi et al., 2018). Arguably the strongest advantage of lidar over sUAV-SfM is the fact that lidar is an active sensor. This insensitivity to lighting conditions enables surveying during low-to-no light conditions, which is prevalent during polar winters. Overall, sUAV-SfM appears to be superior to lidar for small spatial scale sea-ice topographical surveys during daylight, since sUAV-lidar has relatively low accuracies, a heterogenous spatial distribution of points, and higher costs, whereas lidar surveys from larger aircraft use equipment that is significantly more expensive than sUAV-SfM despite lower ground resolution and similar absolute precision values.

To date, few studies have applied InSAR to sea-ice (Berg et al., 2015). They have been collected from large aircraft and satellites (Berg et al., 2015; Dammann et al., 2018; Di Bella et al., 2018; Dierking et al., 2017). sUAV-InSAR surveying has been tested outside of cryospheric research (e.g. Fu et al., 2017) but without sufficient results to enable comparison with sUAV-SfM. Satellite-borne InSAR has ground resolutions as low as 1 m (Niemiec, 2009) with elevation errors of 15 to 50 cm (Di Bella et al., 2018;

Dierking et al., 2017), while airborne InSAR may achieve 20 cm ground resolutions (FSAR) and up to 5 cm precision (Aes-1) (Chen et al., 2014). The topographical change detection threshold depends on the radar wavelength (Dierking et al., 2017), but millimetre-level precision is achievable (Berg et al., 2015). Combined with the ability to operate despite clouds, precipitations and light conditions, it appears to be the most significant advantage of the technique over sUAV-SfM. Another possible advantage of InSAR is its ability to penetrate through solids, which can enable measurements made at the snow to ice interface under some circumstances (Di Bella et al., 2018). This property is desirable for ice thickness estimation as the depth of the snow cover can be ignored (Eicken et al., 2014). But this advantage is often negated by the variable penetration depth of radar waves in ice and snow, which depends on a variety of factors such as salinity, temperature, and radar frequency (Dierking et al., 2017). These factors generally result in inaccurate elevation measurements due to ice penetration (Dierking et al., 2017), or even, if the survey is conducted with wet snow or brine on the ice surface, in an absence of a reflected signal, leading to gaps in measurements (Berg et al., 2015). This prohibits the use of InSAR during melting conditions. Another significant disadvantage of InSAR is the high level of coherence⁶ required for InSAR image production (Berg et al., 2015). Because of this, failures are frequent and the exact cause of failure is often unexplainable (Berg et al., 2015). To avoid failures due to a lack of coherence, the temporal gap must be very short between images, significantly affecting the technique

⁶ Coherence is a measure of correlation affected by, among other factors, the properties of the surface being imaged, the temporal gap between the SAR image pairs used to generate the InSAR, instrument position during SAR image capture and post-processing details, such as image registration and resampling parameters (ESA, 2017)

flexibility. The maximum allowable temporal gap can range from hours (Berg et al., 2015) to days (Chen et al., 2018) between fast ice surveys to seconds for drifting ice (Dierking et al., 2017). Inclement weather such as wind, precipitation or tides may also sufficiently affect coherence and prevent InSAR measurements (Berg et al., 2015). In addition, InSAR is very expensive by sUAV-SfM standards. Airborne instruments are priced well above \$100 000 (SAR Aero, n.d.). For satellite InSAR, commercially available products can range from \$4400 to \$13 000 for InSAR imagery of kilometre-level spatial scale at 1 metre ground resolution (e-geos, 2017), while other products are available free of charge for the end user (ESA, 2015). But for these free InSAR products, the costs still exist, they are simply the burden of another entity (i.e. large organisations or governments). This suggests that, overall, sUAV-SfM is superior to InSAR at small spatial scales for operations in daylight and good weather.

In addition to the previously mentioned advantages of sUAV-SfM over lidar and InSAR, both lidar and InSAR provide only a portion of the information that is available through sUAV-SfM, since sUAV-SfM also generates orthophotos.

An important characteristic that defines the capabilities of a surveying technique is the platform from which the instrument is operated. The possible platforms for the techniques mentioned above are limited to sUAVs, large UAVs, manned aircraft, and satellites (Table 5.1). The advantages of sUAVs over the other platforms include the potential for high ground resolution (due to operation at low altitudes), low costs (purchase and operation), availability, minimal logistical support required and

repairability. Also, sUAVs, due to their limited range, their high portability and their independence from infrastructures such as airports, facilitates the co-location of the surveying instrument and their operators with the surveying target. Under multiple situations, this is an advantage as ground-level measurements and studies can be finely coordinated with aerial surveys, themselves possibly benefiting from GCPs and ice-borne GPS receivers emplaced by the sUAV operator. The disadvantages are the range, spatial scale (due to low altitude), payload mass, regulations, weather impact, reliability and access to remote locations.

Table 5.1. Comparison of the characteristics of platforms used for sea-ice surveys.

Category	sUAVs	Manned aircrafts and large UAVs*	Satellites
Range	Km level in most circumstances Up to 10's of km with SFOC allowing beyond line of sight (BLOS) operations	Up to 1000's km	Global
Altitude	Less than 1 km	100m to 10 km	Low earth orbit
Payload mass	Less than 10 kg	Up to multiple tons	Up to one ton
Platform cost	Up to \$50K	From \$100K's to \$10M's	\$100M's \$ and up
Operating costs	Zero to less than \$10 per hour	\$100 to \$1K's per hour	Variable
Availability	On-demand	Advanced planning required	Advanced planning required Orbit dependant Revisit times Competition with other users
Logistical support required	Carried and operated by ground crew	Specialized crew Takeoff and landing zones	Communication and control ground segment
Regulations	Severe restrictions unless operating under an SFOC exemption	Severe regulations Airspace belongs to manned-aircrafts Payload installation may be difficult	N/A
Weather impact	Severe weather-related restrictions (cold, wind, visibility, etc)	Varies by aircraft, but in general, moderate to no restrictions	No impact
Reliability	Low (fragile)	High	High
Repairability	High	Medium	Minimal Replacements takes years
Other considerations	Co-located with ground personnel (GCPs, sea-level) Remote locations may be costly and/or impossible to survey	Wide-range of aircrafts capability May still require personnel on the ground, negating range advantages	Strategic capabilities - instruments may not fulfill all users requirements Instruments usually state-of-the art with excellent calibration

*Large UAVs share most of the characteristics of manned aircrafts in this table. As such, they were grouped together.

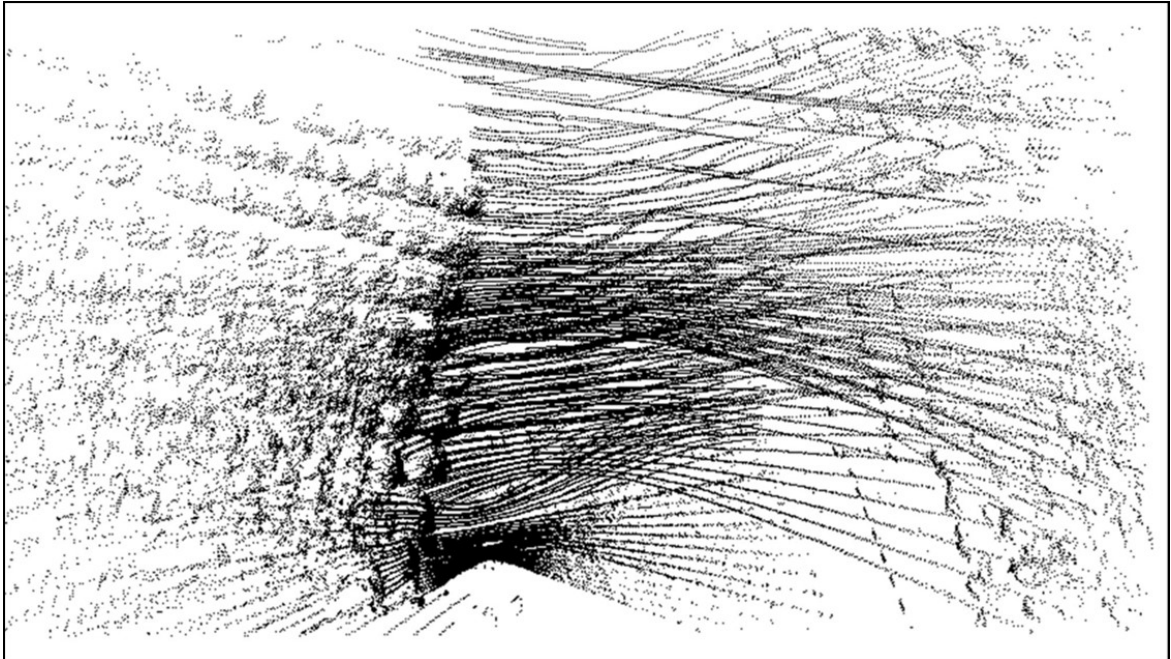


Figure 5.2. Example of the heterogeneous spatial distribution of points from a UAV-borne lidar survey. The surveyed area represented a field and a forest.

Source : Elaksher et al., 2017

Overall, when using SfM Surveys 11, 12 and 13 as examples, the comparison of sUAV-SfM with equivalent established sea-ice topographical surveying techniques clearly demonstrated that sUAV-SfM is an advantageous mapping technique when used within a specific range of conditions and requirements, such as fair weather, daylight operations, accessible locations, kilometre-level (and less) spatial scale surveys and low-cost. Therefore, within the spectrum of sea-ice topographical surveying techniques and required sea-ice topographical products, there are conditions where sUAV-SfM would be an acceptable or the most desirable technique. However, if the overall performance of the *Emlid Reach* during this thesis was representative of all low-cost receivers (discussed

further in section 5.5), the low reliability of these receivers is the main drawback from the technique for users requiring high accuracies. Should this issue remain unsolved, sUAV-SfM would likely lose some of its advantages over established techniques.

5.5 Possible improvements to the technique

The sUAV-SfM surveying and data-processing setup used for this thesis was experimental, and therefore, had practical limitations. This means that the technique has the potential to be significantly improved and streamlined. Possible improvements are discussed here.

Improvements to low-cost GPS receivers capable of carrier-phase measurements, would likely have the greatest effects on increasing the reliability of the technique and on lowering costs. Existing or developing low-cost GPS receivers could have better reliability than the *Emlid Reach* for a similar price point, which could eliminate the need of using costly high-end GPS receivers for the base-station and tide monitoring. Alternatively, multiple low-cost GPS receivers, ideally from different manufacturers, could be mounted on the UAV to increase redundancy and improve the ratio of reliable data. This would also provide additional measurements to the UAV attitude and an ability to assess the positional accuracy of each receiver. A high-end GPS receiver could also be mounted on a survey UAV with a higher payload capacity, but at higher costs.

For further improvement to the accuracy, precision and repeatability, several options are available. As the quality of SfM surveys is influenced by the sensor-to-

surface distance, lower flying altitudes for UAVs would be expected to result in improved data quality (but with less areal coverage). Also, while GCPs were used sparingly for the SfM surveys in this thesis, most SfM surveys would benefit from a higher density of GCPs, as it generally improves the accuracy (Pix4D, n.d.). As well, the camera calibration models, generated during the bundle adjustment step of the SfM workflow, could be improved. For this thesis, the model generated by *Agisoft Photoscan* varied between each SfM survey. This was partially due to the *Sony E PZ* lens used on the camera, which had a power-zoom that automatically retracted the lens when powered down and reset the focal length and focus when the camera was powered on. This feature made it impossible to keep the same lens configuration between SfM surveys. But the lens calibration models are also likely to vary slightly between SfM surveys since the calibration parameters calculated during the bundle adjustment step cannot be exempt from errors. To minimize this source of error, lenses with an exclusive manual control option should be used, and the focal length and focus controls should be fixed (e.g. tape over the control rings). The lenses could also be calibrated (either through an independent calibration process, or through the averaging of multiple SfM surveys) to reduce the number of variables to be solved during bundle adjustment.

Increases to the surveying area size could be made in various ways.

Modifications to the surveying parameters, including reducing sidelap and overlap ratio and increasing altitude (this would require an SFOC from Transport Canada) could be made, albeit with the risk of reduced quality. sUAV-SfM surveys composed of a series of sUAV flights conducted in succession, with a battery swap between flights, could be

conducted, as per SfM Survey 14. The range of sUAVs could be improved with weight optimization (e.g. smaller camera), improved aerodynamics and the use of fixed-wing sUAVs (Laliberté, 2016). Alternate sources of power with higher energy density could also be used. Gasoline-powered UAVs for instance, have the potential to provide flight times of several hours (Pegasus Aeronautics, n.d.). Improvements could also be possible with different airspace regulations and restrictions. An SFOC (Transport Canada, 2018b) could ease some of the restrictions under which the sUAV flights for this thesis were conducted, such as altitude, UAV weight, weather restrictions, distance and line of sight between the UAV pilot and the sUAV and the prohibition of autonomous flights. Since UAV regulations in Canada are evolving (Transport Canada, 2018c), future regulatory changes may ease some of the current requirements (although regulation tightening is also possible). Alternatively, operations in international airspace (12 nautical miles offshore) or by operating in the airspace of a foreign country could be a viable way to circumvent Transport Canada regulations. Swarms of autonomous, long-ranging sUAVs operated simultaneously from various locations and constantly surveying large areas of sea-ice during daylight would likely be the ultimate level of improvements possible with the technique if all the spatial scale improvement points could be simultaneously implemented (Haugen and Imsland, 2014).

While the research site for this thesis was located on fast-ice, most of the world's sea-ice is freely-drifting pack ice. Since pack ice movements includes rotation and translation, to survey this predominant category of sea-ice, these movements would have to be captured to properly georeference images to an ice-floe. It also means that for

surveys conducted far from fixed landforms and structures, a fixed base-station would not be available for GPS accuracy augmentation. As such, an array of 3 or more GPS receivers would be required for each ice floe, and kinematic PPP and/or moving-baseline PPK (i.e., a PPK solution using a non-static base station) would be required to resolve coordinates and movements. Crawford et al. (2018) provides an example of how this could be done, using ice islands as targets and indirect georeferencing using GCPs. Direct georeferencing using L1/L2 receivers, post-corrected with kinematic PPP, may also be a viable alternative (Nolan, 2015). Positional accuracies of ± 10 cm (95% CI) have been reported using this technique and this translates into DEM registration errors on the order of ± 8 cm (95% CI), although these estimates were partly enhanced by ground registration (Nolan, 2015). However, PPK/RTK is still marginally better than kinematic PPP (Yigit and Gurlek, 2017) and, furthermore, this technique requires a UAV (or aeroplane) with enough capacity to lift a dual-frequency GPS..

5.6 Practical applications

As demonstrated through the comparison with existing techniques, sUAV-SfM has unique capabilities. Overall, its main advantage is the ability to generate dense point clouds and orthophotos at low costs over small spatial scales. As demonstrated at Section 5.4, it has the potential to become the surveying technique of choice for a variety of tasks. What is seemingly the most appropriate task for sUAV-SfM in sea-ice applications is the surveying of pressure ridges because the spatial scale of pressure ridges along its thinnest dimension is generally small when compared with the resolving

power of a lot of surveying techniques (Strub-Klein and Sudom, 2012). There are opportunities for other applications as well.

Ridge surveying is most commonly conducted with the labour intensive ground surveys and drilling techniques (Strub-Klein and Sudom, 2012), which could be conducted by sUAV-SfM instead. This thesis clearly demonstrated that sUAV-SfM surveys can easily resolve even low prominence ridges. Therefore, no issues are to be expected from the surveying of ridges of greater prominence by sUAV-SfM, which are common (e.g. Strub-Klein and Sudom's (2012) review of over 300 first-year pressure ridges found that the mean sail dimensions of pressure ridges were 2 m height by 12 m width).

Ridge dimensions, including submerged features which can be estimated from the sail dimensions (Strub-Klein and Sudom, 2012), are essential ice characteristics required for engineering, navigation, modeling and space-borne remote sensing of sea-ice. For engineering purposes, ridge dimensions are required to estimate their strength and the maximum force they can exert on structures. For navigation, the same principles apply to route-finding; stronger ridges will require more effort and time to be breached by icebreakers. Furthermore, for ice-surface transport, steep and rugged ridges can be perilous obstacles for foot and vehicle travel (Dammann et al., 2018). For sea-ice modelling, there is a need for field measurements of the ridging process for the improvement and validation of models. For space-borne remote sensing, field

measurements of ridges are required for the interpretation and validation of the acquired data, for example by InSAR.

Other possible uses of the technique includes sea-ice thickness estimation. Due to the low-cost of the technique, SfM surveys for ice thickness estimations could be conducted by people or organisations with localized needs, such as an Arctic port or icebreaker operators, or as a validation tool for ice thickness estimation instruments operating at a larger spatial scale. Further uses could also be the measurement of snow distribution patterns on sea-ice, surface melt monitoring, lead measurements and monitoring, security surveillance, etc.

6 Conclusion

The aim of this study was to determine the quality of sUAV-SfM topographical surveys of sea-ice as well as the associated challenges and outcomes of processing and collecting the data at a relatively low cost. This aim was achieved. The results demonstrated that sea-ice topography can be surveyed by sUAV-SfM with excellent accuracy, precision, repeatability, spatial resolution and speed at the kilometre-level spatial scale. However, reliability issues with the low-cost GPS receivers decreased the reliability of the technique. It can therefore be concluded that sUAV-SfM is a valuable low-cost sea-ice topography mapping technique provided that GPS reliability issues are addressed.

In this study, three specific objectives were met to answer the overarching research question:

The first objective was to quantify the accuracy, precision and repeatability of sUAV-SfM survey point clouds over sea-ice. Three sUAV-SfM surveys were compared to a reference ground survey to calculate the vertical accuracy and precision. Due to the UAV-borne GPS reliability issues, a different set of sUAV-SfM surveys than those originally planned for this objective were used, which meant there was low areal overlap and topographical changes occurred between the reference ground and SfM surveys. The calculated mean vertical accuracy of 56 ± 14 mm with a precision of 40 mm and the RMSE of 69 mm was likely unrepresentative of the total study area. Instead, a more conservative RMSE value of 87 mm was established for the technique, based on the

nature of topographical changes observed between the SfM and the ground surveys, the spatial distribution patterns for the errors and previous studies. The repeatability was calculated by comparing three sUAV-SfM point clouds with each other. The mean difference in vertical distance was 20 mm with a standard deviation of 77 mm and a RMSE of 80 mm. The point clouds were well-registered originally, as a point cloud post-SfM registration of all three points clouds only improved repeatability values by 1-2 cm. The spatial distribution of the errors indicated that a portion of the repeatability error was systematic, increasing the ability for changes to be detected. Overall, the accuracy, precision and repeatability of sUAV-SfM over sea-ice was quantified, with results at least as good as when the technique is used over static landscapes.

The second objective was to use single and multiple sUAV-SfM surveys to detect, measure and visualize sea-ice features and processes, with a focus on pressure ridges. Elevation maps provided valuable sea-ice topographical information such as the elevation above sea-level and fine relief details. Changes were visualized through transects and point cloud-to-point cloud distance maps. A millimetre-level deformation field, occurring along a narrow corridor running along the pressure ridge, was detected at high-tides with the point cloud-to-point cloud maps, and could be mapped and measured despite its relatively narrow spatial distribution and the small amplitude of the movement. Metre-scale sea-ice deformation processes were visualized with a transect of the three point clouds, revealing a dynamic interaction of the ice with the sea-floor through the tide-cycle. Orthophotos provided alternate means of visualizing the sea-ice surface, that could be used either as a standalone product or combined with point clouds as mutually

beneficial products for improved identification and understanding of sea-ice features. The second objective was fulfilled, with sUAV-SfM products providing very high levels of topographical details for sea-ice features and processes detection, measurement and visualization, especially for pressure ridges.

The third objective was to analyze the advantages and disadvantages of sUAV-SfM as a tool to study sea-ice topography and compare it to other more established techniques. Except for the substantial reliability issues with the low-cost GPS receiver and other minor issues, the operational performance of sUAV-SfM was excellent. The UAV and its components were functional and easy to use in the field and data collection was fast. Field preparation and data-processing required sustained initial efforts, but these were progressively minimized through problem solving and increased user experience. The SfM algorithms performed well with sea-ice. With setup costs of approximately \$6000 for the typical user and negligible operational costs, sUAV-SfM was found to be a low-cost technique. The technique was superior to similar established sea-ice topographical surveying techniques (classic photogrammetry, airborne lidar and InSAR) for kilometre-scale spatial scale surveys in good weather and light conditions when GPS receivers perform reliability, with classic photogrammetry lacking simplicity and flexibility during the image acquisition phase, airborne lidar requiring costly platforms for consistent results while providing low point density, and InSAR being generally costly, complex and very sensible to numerous acquisition factors. Since the use of sUAV-SfM for this thesis was experimental, there are a lot of opportunities for improvement, especially to increase the reliability of GPS receivers, augment the quality

and the spatial scale, and extend sUAV-SfM surveys to free-floating ice. sUAV-SfM could be a technique of choice to conduct surveys of pressure ridges and estimate sea-ice topography, while also being well-suited to several other sea-ice surveying purposes. Overall, there are clear advantages to sUAV-SfM that outweigh its disadvantages.

This thesis provided the first known extensive testing of sUAV-SfM for topographical surveys of sea-ice. The difficulties associated with tidal effects on the georeferencing measurements and the low image contrast were demonstrated to be surmountable. The overall capabilities, drawbacks and potential improvements are now better defined, and it is now known that the technique can be valuable despite its low-cost. These results have a strong potential to be of interest for prospective sUAV-SfM users, from sea-ice scientists and engineers, to local government in Arctic communities and icebreaker operators.

Building on the results of this thesis, further work would be required to calculate with greater fidelity the accuracy and precision of the technique through dedicated SfM and ground surveys of sea-ice conducted in quick succession. The impact of the various surveying parameters also requires characterisation, which would provide valuable information to optimize future surveys. Improved reliability for photo georeferencing is also a top priority to fully benefit from the advantages of sUAV-SfM. Further work could also be considered to investigate the faint downward movement of the ice along the pressure ridge at high tides (or other circumstances, such as during compressive events), as this type of movement does not seem to have previously been described in published

sources. sUAV-SfM would likely be the surveying technique of choice for such an investigation.

7 References

- ACUASI, 2015. Sea Ice Survey and Generating Topological Maps [WWW Document]. Univ. Alsk. Fairbanks. URL <http://acuasi.alaska.edu/missions/seaice> (accessed 5.31.18).
- Agisoft LLC, 2017. Agisoft PhotoScan User Manual Professional Edition, Version 1.3.
- Barnes, P.W., Asbury, J.L., Rearic, D.M., Ross, C.R., 1987. Ice erosion of a sea-floor knickpoint at the inner edge of the stamukhi zone, Beaufort Sea, Alaska. *Mar. Geol.* 76, 207–222. [https://doi.org/10.1016/0025-3227\(87\)90030-2](https://doi.org/10.1016/0025-3227(87)90030-2)
- Berg, A., Dammert, P., Eriksson, L.E.B., 2015. X-Band interferometric SAR observations of Baltic fast ice. *IEEE Trans. Geosci. Remote Sens.* 53, 1248–1256. <https://doi.org/10.1109/TGRS.2014.2336752>
- Bergan, P.G., Cammaert, G., Skeie, G., Tharigopula, V., 2010. On the potential of computational methods and numerical simulation in ice mechanics. *IOP Conf. Ser. Mater. Sci. Eng.* 10, 012102. <https://doi.org/10.1088/1757-899X/10/1/012102>
- Bhardwaj, A., Sam, L., Akanksha, Martín-Torres, F.J., Kumar, R., 2016a. UAVs as remote sensing platform in glaciology: Present applications and future prospects. *Remote Sens. Environ.* 175, 196–204. <https://doi.org/10.1016/j.rse.2015.12.029>
- Bhardwaj, Anshuman, Sam, L., Bhardwaj, Akanksha, Martín-Torres, F.J., 2016b. LiDAR remote sensing of the cryosphere: Present applications and future prospects. *Remote Sens. Environ.* 177, 125–143. <https://doi.org/10.1016/j.rse.2016.02.031>
- Brunier, G., Fleury, J., Anthony, E.J., Gardel, A., Dussouillez, P., 2016. Close-range airborne Structure-from-Motion Photogrammetry for high-resolution beach morphometric surveys: Examples from an embayed rotating beach. *Geomorphology* 261, 76–88. <https://doi.org/10.1016/j.geomorph.2016.02.025>
- Castellani, G., Lüpkes, C., Hendricks, S., Gerdes, R., 2014. Variability of Arctic sea-ice topography and its impact on the atmospheric surface drag. *J. Geophys. Res. Oceans* 119, 6743–6762. <https://doi.org/10.1002/2013JC009712>
- Charron, A., 2005. The Northwest Passage shipping channel: Sovereignty first and foremost and sovereignty to the side. *J. Mil. Strateg. Stud.* 7.
- Chen, L., Xiao, H., Wang, H., Lin, Y., 2014. Research Development of High Precision Real-time Airborne InSAR System. *J. Comput.* 9. <https://doi.org/10.4304/jcp.9.1.189-195>
- Chen, Z., Montpetit, B., Duffe, J., Pasher, J., 2018. Mapping of Sea Ice Route Trafficability with InSAR.
- Chiang, K.-W., Tsai, G.-J., Li, Y.-H., El-Sheimy, N., 2017. Development of LiDAR-based UAV system for environment reconstruction. *IEEE Geosci. Remote Sens. Lett.* 14, 1790–1794. <https://doi.org/10.1109/LGRS.2017.2736013>
- Choi, M., Chung, H., Yamaguchi, H., Nagakawa, K., 2015. Arctic sea route path planning based on an uncertain ice prediction model. *Cold Reg. Sci. Technol.* 109, 61–69. <https://doi.org/10.1016/j.coldregions.2014.10.001>
- Chu, H.-J., Wang, C.-K., Huang, M.-L., Lee, C.-C., Liu, C.-Y., Lin, C.-C., 2014. Effect of point density and interpolation of LiDAR-derived high-resolution DEMs on

- landscape scarp identification. *GIScience Remote Sens.* 51, 731–747.
<https://doi.org/10.1080/15481603.2014.980086>
- Clapuyt, F., Vanacker, V., Van Oost, K., 2016. Reproducibility of UAV-based earth topography reconstructions based on Structure-from-Motion algorithms. *Geomorphology* 260, 4–15. <https://doi.org/10.1016/j.geomorph.2015.05.011>
- CloudCompareWiki, 2015. Cloud-to-Cloud Distance - CloudCompareWiki [WWW Document]. CloudCompare Wiki. URL http://www.cloudcompare.org/doc/wiki/index.php?title=Cloud-to-Cloud_Distance (accessed 5.27.18).
- Crawford, A.J., Mueller, D., Joyal, G., 2018. Surveying drifting icebergs and ice islands: deterioration detection and mass estimation with aerial photogrammetry and laser scanning. *Remote Sens.* 10, 575. <https://doi.org/10.3390/rs10040575>
- Dammann, D.O., Eicken, H., Mahoney, A.R., Saitet, E., Meyer, F.J., George, J.C. “Craig,” 2018. Traversing sea ice - Linking surface roughness and ice trafficability through SAR polarimetry and interferometry. *IEEE J. Sel. Top. Appl. Earth Obs. Remote Sens.* 11, 416–433.
<https://doi.org/10.1109/JSTARS.2017.2764961>
- Di Bella, A., Skourup, H., Bouffard, J., Parrinello, T., 2018. Uncertainty reduction of Arctic sea ice freeboard from CryoSat-2 interferometric mode. *Adv. Space Res.* [serial online] Available from: URL:<http://linkinghub.elsevier.com/retrieve/pii/S0273117718302217>. <https://doi.org/10.1016/j.asr.2018.03.018>
- Dierking, W., Dierking, W., Lang, O., Busche, T., 2017. Sea ice local surface topography from single-pass satellite InSAR measurements: a feasibility study. *The Cryosphere* 11, 1967–1985.
- Dietrich, J.T., 2016. Riverscape mapping with helicopter-based Structure-from-Motion photogrammetry. *Geomorphology, The Natural and Human Structuring of Rivers and other Geomorphic Systems: A Special Issue in Honor of William L. Graf* 252, 144–157. <https://doi.org/10.1016/j.geomorph.2015.05.008>
- Dimitri, 2015. Averaging two clouds. *CloudCompare Forum.* [WWW Document]. URL <http://www.cloudcompare.org/forum/viewtopic.php?t=1226> (accessed 27.05.18).
- Divine, D.V., Pedersen, C.A., Karlsen, T.I., Aas, H.F., A. Granskog, M., R. Hudson, S., Gerland, S., 2016. Photogrammetric retrieval and analysis of small scale sea ice topography during summer melt. *Cold Reg. Sci. Technol.* 129, 77–84.
<https://doi.org/10.1016/j.coldregions.2016.06.006>
- Doble, M.J., Skourup, H., Wadhams, P., Geiger, C.A., 2011. The relation between Arctic sea ice surface elevation and draft: A case study using coincident AUV sonar and

- airborne scanning laser. *J. Geophys. Res.* 116.
<https://doi.org/10.1029/2011JC007076>
- e-geos, 2017. e-geos Price List [WWW Document]. URL <http://www.e-geos.it/index.php> (accessed 7.11.18).
- Eicken, H., Bluhm, B.A., Collins, R.E., Gradinger, R.R., Haas, C., Ingham, M., Mahoney, A., Nicolaus, M., Perovich, D., 2014. *Field Techniques in Sea-Ice Research*.
- Eicken, H., Gradinger, R., Salganek, M., Shirasawa, K., Perovich, D., Lepparanta, M., 2009. *Field Techniques for sea ice research*. University of Alaska Press, University of Alaska, Fairbanks, United States.
- Ekeberg, O.-C., Høyland, K., Hansen, E., 2015. Ice ridge keel geometry and shape derived from one year of upward looking sonar data in the Fram Strait. *Cold Reg. Sci. Technol.* 109, 78–86. <https://doi.org/10.1016/j.coldregions.2014.10.003>
- Elaksher, A.F., Bhandari, S., Carreon-Limones, C.A., Lauf, R., 2017. Potential of UAV lidar systems for geospatial mapping, in: *Lidar Remote Sensing for Environmental Monitoring 2017*. Presented at the Lidar Remote Sensing for Environmental Monitoring 2017, International Society for Optics and Photonics, p. 104060L. <https://doi.org/10.1117/12.2275482>
- Eltner, A., Kaiser, A., Castillo, C., Rock, G., Neugirg, F., Abellán, A., 2016. Image-based surface reconstruction in geomorphometry - merits, limits and developments. *Earth Surf. Dyn.* 4, 359–389. <https://doi.org/10.5194/esurf-4-359-2016>
- Eltoft, T., Doulgeris, A.P., Brekke, C., Solbø, S., Gerland, S., Hanssen, A., 2015. Imaging sea ice structure by remote sensing sensors. Presented at the 23rd International Conference on Port and Ocean Engineering under Arctic Conditions, Trondheim, Norway.
- Ely, J.C., Graham, C., Barr, I.D., Rea, B.R., Spagnolo, M., Evans, J., 2016. Using UAV acquired photography and structure from motion techniques for studying glacier landforms: application to the glacial flutes at Isfallsglaciären. *Earth Surf. Process. Landf.* 42, 853-1008. <https://doi.org/10.1002/esp.4044>
- ESA, 2017. RADAR and SAR Glossary [WWW Document]. Eur. Space Agency. URL <https://earth.esa.int/handbooks/asar/CNTR5-2.html> (accessed 7.28.18).
- ESA, 2015. Sentinel-1 - Data Products - Sentinel Online [WWW Document]. Eur. Space Agency. URL <https://sentinel.esa.int/web/sentinel/missions/sentinel-1/data-products> (accessed 8.3.18).
- ESA, 2014. Essential groundwork / CryoSat / Observing the Earth / Our Activities / ESA [WWW Document]. Eur. Space Agency. URL http://www.esa.int/Our_Activities/Observing_the_Earth/CryoSat/Essential_groundwork (accessed 6.23.18).
- ESA, 2013. CryoSat [WWW Document]. Eur. Space Agency. URL http://www.esa.int/Our_Activities/Observing_the_Earth/CryoSat (accessed 6.22.18).
- ESA, n.d. Navipedia [WWW Document]. Eur. Space Agency. URL http://www.navipedia.net/index.php/Main_Page (accessed 4.5.18).
- Everett, T., 2017. PPK vs RTK: A look at RTKLIB for post-processing solutions. [WWW Document]. Eur. Space Agency. URL

- <https://rtklibexplorer.wordpress.com/2017/08/21/ppk-vs-rtk-a-look-at-rtklib-for-post-processing-solutions/> (accessed 05.04.18).
- Farrell, S.L., Markus, T., Kwok, R., Connor, L., 2011. Laser altimetry sampling strategies over sea ice. *Ann. Glaciol.* 52, 69–76.
<https://doi.org/10.3189/172756411795931660>
- Fonstad, M.A., Dietrich, J.T., Courville, B.C., Jensen, J.L., Carbonneau, P.E., 2013. Topographic structure from motion: a new development in photogrammetric measurement. *Earth Surf. Process. Landf.* 38, 421–430.
<https://doi.org/10.1002/esp.3366>
- Fu, X., Xiang, M., Wang, B., Jiang, S., Wang, J., 2017. Preliminary result of a novel yaw and pitch error estimation method for UAV-based FMCW InSAR, in: 2017 IEEE International Geoscience and Remote Sensing Symposium (IGARSS). Presented at the 2017 IEEE International Geoscience and Remote Sensing Symposium (IGARSS), pp. 463–465. <https://doi.org/10.1109/IGARSS.2017.8126993>
- Girod, L., Nuth, C., Kohler, J., 2017. Terrain changes from images acquired on opportunistic flights by SfM photogrammetry. *The Cryosphere* 11, 827–840.
<https://doi.org/10.5194/tc-11-827-2017>
- Haas, C., 1998. Evaluation of ship-based electromagnetic-inductive thickness measurements of summer sea-ice in the Bellingshausen and Amundsen Seas, Antarctica. *Cold Reg. Sci. Technol.* 27, 1–16. [https://doi.org/10.1016/S0165-232X\(97\)00019-0](https://doi.org/10.1016/S0165-232X(97)00019-0)
- Haas, C., Lobach, J., Hendricks, S., Rabenstein, L., Pfaffling, A., 2009. Helicopter-borne measurements of sea ice thickness, using a small and lightweight, digital EM system. *J. Appl. Geophys., Airborne Geophysics* 67, 234–241.
<https://doi.org/10.1016/j.jappgeo.2008.05.005>
- Hatanaka, Y., 2008. A compression format and tools for GNSS observation data. *Bull. Geogr. Surv. Inst.* 55, 21–30.
- Haugen, J., Imsland, L., 2014. Autonomous aerial ice observation for ice defense. *Model. Identif. Control* 35, 279–291. <https://doi.org/10.4173/mic.2014.4.5>
- Haugen, J., Imsland, L., Løset, S., Skjetne, R., 2011. Ice observer system for ice management operations. Presented at the Twenty-first International Offshore and Polar Engineering Conference, International Society of Offshore and Polar Engineers, Maui, Hawaii, USA.
- Herzfeld, U.C., Hunke, E.C., McDonald, B.W., Wallin, B.F., 2015. Sea ice deformation in Fram Strait — Comparison of CICE simulations with analysis and classification of airborne remote-sensing data. *Cold Reg. Sci. Technol.* 117, 19–33. <https://doi.org/10.1016/j.coldregions.2015.05.001>
- Higgins, S., 2018. Velodyne cuts VLP-16 lidar price to \$4k [WWW Document]. SPAR 3D. URL <https://www.spar3d.com/news/lidar/velodyne-cuts-vlp-16-lidar-price-4k/> (accessed 7.10.18).
- Holt, B., Kanagaratnam, P., Gogineni, S.P., Ramasami, V.C., Mahoney, A., Lytle, V., 2009. Sea ice thickness measurements by ultrawideband penetrating radar: First

- results. *Cold Reg. Sci. Technol.* 55, 33–46.
<https://doi.org/10.1016/j.coldregions.2008.04.007>
- Høyland, K.V., 2002. Consolidation of first-year sea ice ridges. *J. Geophys. Res. Oceans* 107, 15-1-15–16. <https://doi.org/10.1029/2000JC000526>
- Hvidegaard, S.M., Nielsen, J.E., Sørensen, L.S., Simonsen, S.B., Skourup, H., Forsberg, R., Helm, V., Bjerg, T., 2015. ESA CryoVEx 2014 - Airborne ASIRAS radar and laser scanner measurements during 2014 CryoVEx campaign in the Arctic (Report No. 978-87-91694-26-4). Technical University of Denmark (DTU).
- IATA, 2018. Passengers travelling with lithium batteries. [WWW Document]. URL <https://www.iata.org/whatwedo/cargo/dgr/Documents/passenger-lithium-battery.pdf> (accessed 8.1.18).
- IGS, n.d. IGS Products [WWW Document]. URL <http://www.igs.org/products/data> (accessed 7.19.18).
- Ingwer, P., Gassen, F., Püst, S., Duhn, M., Schällicke, M., Müller, K., Ruhm, H., Rettig, J., Hasche, E., Fischer, A., Creutzburg, R., 2015. Practical usefulness of structure from motion (SfM) point clouds obtained from different consumer cameras. Presented at the Mobile Devices and Multimedia: Enabling Technologies, Algorithms, and Applications 2015, International Society for Optics and Photonics, p. 941102. <https://doi.org/10.1117/12.2074892>
- Jackson, J., Saborio, R., Ghazanfar, S.A., Gebre-Egziabher, D., Davis, B., 2018. Evaluation of Low-Cost, Centimeter-Level Accuracy OEM GNSS Receivers (Report). Minnesota Department of Transportation.
- James M. R., Robson S., 2012. Straightforward reconstruction of 3D surfaces and topography with a camera: Accuracy and geoscience application. *J. Geophys. Res. Earth Surf.* 117. <https://doi.org/10.1029/2011JF002289>
- Kiss, K., Malinen, J., Tokola, T., 2016. Comparison of high and low density airborne lidar data for forest road quality assessment. *ISPRS Ann. Photogramm. Remote Sens. Spat. Inf. Sci.* III–8, 167–172. <https://doi.org/10.5194/isprsannals-III-8-167-2016>
- Krzan, G., Dawidowicz, K., Stepniak, K., Świątek, K., 2017. Determining normal heights with the use of Precise Point Positioning. *Surv. Rev.* 49, 259–267.
<https://doi.org/10.1080/00396265.2016.1164939>
- Lague, D., Brodu, N., Leroux, J., 2013. Accurate 3D comparison of complex topography with terrestrial laser scanner: application to the Rangitikei canyon (N-Z). *ArXiv13021183 Phys.*
- Laliberté, J., 2016. UAV Short Course. 10.24.16, Carleton University/Nav Canada
- Lane, S.N., Widdison, P.E., Thomas, R.E., Ashworth, P.J., Best, J.L., Lunt, I.A., Sambrook Smith, G.H., Simpson, C.J., 2010. Quantification of braided river channel change using archival digital image analysis. *Earth Surf. Process. Landf.* 35, 971–985. <https://doi.org/10.1002/esp.2015>
- Larsen, C., n.d. Airborne LiDAR at University of Alaska Fairbanks Geospatial Institute [WWW Document]. URL http://fairweather.alaska.edu/chris/Lidar_new.html (accessed 6.22.18).
- Lean, R., 2012. UAF researchers use drones to evaluate sea ice thickness at Nome and aid incoming tanker | Poker Flat Research Range [WWW Document]. Univ. Alsk.

- Fairbanks Geophys. Inst. URL <http://www.pfrr.alaska.edu/news/uaf-researchers-use-drones-evaluate-sea-ice-thickness-nome-and-aid-incoming-tanker> (accessed 5.25.18).
- Lee, S., Im, J., Kim, J., Kim, M., Shin, M., Kim, H., Quackenbush, L.J., 2016. Arctic sea ice thickness estimation from CryoSat-2 satellite data using machine learning-based lead detection. *Remote Sens.* 8, 698. <https://doi.org/10.3390/rs8090698>
- Leick, A., Rapoport, L., Tatarnikov, D., 2015. *GPS Satellite Surveying*, 4th ed. John Wiley & Sons, Inc, Hoboken, New Jersey.
- Leppäranta, M., Hakala, R., 1992. The structure and strength of first-year ice ridges in the Baltic Sea. *Cold Reg. Sci. Technol.* 20, 295–311. [https://doi.org/10.1016/0165-232X\(92\)90036-T](https://doi.org/10.1016/0165-232X(92)90036-T)
- Leppäranta, P.M., 2011. *The Drift of Sea Ice*, Springer Praxis Books. Springer Berlin Heidelberg. https://doi.org/10.1007/978-3-642-04683-4_2
- Light, J., Parthasarathy, S., McIver, W., 2012. Monitoring winter ice conditions using thermal imaging cameras equipped with infrared microbolometer sensors. *Procedia Comput. Sci.* 10, 1158–1165. <https://doi.org/10.1016/j.procs.2012.06.166>
- Lowe, D.G., 2004. Distinctive image features from scale-invariant keypoints. *Int. J. Comput. Vis.* 60, 91–110. <https://doi.org/10.1023/B:VISI.0000029664.99615.94>
- Lucieer, A., Jong, S.M. de, Turner, D., 2014. Mapping landslide displacements using Structure from Motion (SfM) and image correlation of multi-temporal UAV photography. *Prog. Phys. Geogr.* 38, 97–116. <https://doi.org/10.1177/0309133313515293>
- Mallalieu, J., Carrivick, J.L., Quincey, D.J., Smith, M.W., James, W.H.M., 2017. An integrated Structure-from-Motion and time-lapse technique for quantifying ice-margin dynamics. *J. Glaciol.* 63, 937–949. <https://doi.org/10.1017/jog.2017.48>
- Mancini, F., Dubbini, M., Gattelli, M., Stecchi, F., Fabbri, S., Gabbianelli, G., 2013. Using unmanned aerial vehicles (UAV) for high-resolution reconstruction of topography: the Structure from Motion approach on coastal environments. *Remote Sens.* 5, 6880–6898. <https://doi.org/10.3390/rs5126880>
- Martin, T., 2006. Comparison of different ridge formation models of Arctic sea ice with observations from laser profiling. *Ann. Glaciol.* 44, 403–410. <https://doi.org/10.3189/172756406781811132>
- Melling, H., Johnston, P.H., Riedel, D.A., 1995. Measurements of the underside topography of sea ice by moored subsea sonar. *J. Atmospheric Ocean. Technol.* 12, 589–602. [https://doi.org/10.1175/1520-0426\(1995\)012<0589:MOTUTO>2.0.CO;2](https://doi.org/10.1175/1520-0426(1995)012<0589:MOTUTO>2.0.CO;2)
- Micheletti, N., Chandler, J.H., Lane, S.N., 2015. Investigating the geomorphological potential of freely available and accessible structure-from-motion photogrammetry using a smartphone. *Earth Surf. Process. Landf.* 40, 473–486. <https://doi.org/10.1002/esp.3648>
- Mlambo, R., Woodhouse, I.H., Gerard, F., Anderson, K., 2017. Structure from Motion (SfM) photogrammetry with drone data: A low cost method for monitoring

- greenhouse gas emissions from forests in developing countries. *Forests* 8, 68. <https://doi.org/10.3390/f8030068>
- Mosbrucker, A.R., Major, J.J., Spicer, K.R., Pitlick, J., 2016. Camera system considerations for geomorphic applications of SfM photogrammetry. *Earth Surf. Process. Landf.* 42, 969–986. <https://doi.org/10.1002/esp.4066>
- Multala, J., Hautaniemi, H., Oksama, M., Leppäranta, M., Haapala, J., Herlevi, A., Riska, K., Lensu, M., 1996. An airborne electromagnetic system on a fixed wing aircraft for sea ice thickness mapping. *Cold Reg. Sci. Technol.* 24, 355–373. [https://doi.org/10.1016/S0165-232X\(96\)00006-7](https://doi.org/10.1016/S0165-232X(96)00006-7)
- NASA, 2018a. Land, Vegetation, and Ice Sensor (LVIS) [WWW Document]. URL <https://lvis.gsfc.nasa.gov/Home/index.html> (accessed 6.22.18).
- NASA, 2018b. Icesat-2 [WWW Document]. URL <https://icesat-2.gsfc.nasa.gov/> (accessed 6.22.18).
- NASA, 2017. Airborne Topographic Mapper [WWW Document]. URL <https://atm.wff.nasa.gov/> (accessed 6.22.18).
- Natan, M., Jim, C., Stuart, L., 2014. Investigating the geomorphological potential of freely available and accessible structure-from-motion photogrammetry using a smartphone. *Earth Surf. Process. Landf.* 40, 473–486. <https://doi.org/10.1002/esp.3648>
- Niemiec, M., 2009. POTENTIALS OF HIGH RESOLUTION TERRASAR-X IMAGES IN INSAR PROCESSING FOR EARTH DEFORMATION AND ENVIRONMENTAL STUDIES 6.
- Nolan, M., Larsen, C., Sturm, M., 2015. Mapping snow depth from manned aircraft on landscape scales at centimeter resolution using structure-from-motion photogrammetry. *The Cryosphere* 9, 1445–1463. <https://doi.org/10.5194/tc-9-1445-2015>
- NRCan, 2013. NRCan Tools and Applications [WWW Document]. URL <http://www.nrcan.gc.ca/earth-sciences/geomatics/geodetic-reference-systems/tools-applications/10925#ppp> (accessed 4.5.18).
- NSIDC, 2018. National Snow and Ice Data Center - All About Sea Ice [WWW Document]. NSIDC. URL <https://nsidc.org/cryosphere/seaice/index.html> (accessed 5.25.18).
- Obert, K.M., Brown, T.G., 2011. Ice ridge keel characteristics and distribution in the Northumberland Strait. *Cold Reg. Sci. Technol.* 66, 53–64. <https://doi.org/10.1016/j.coldregions.2011.01.004>
- Parmerter, R.R., Coon, M.D., 1972. Model of pressure ridge formation in sea ice. *J. Geophys. Res.* 77, 6565–6575. <https://doi.org/10.1029/JC077i033p06565>
- Pegasus Aeronautics, n.d. Pegasus Aeronautics [WWW Document]. URL <http://pegasusaero.ca/> (accessed 7.12.18).
- Peterson, I.K., Prinsenberg, S.J., Holladay, J.S., 2008. Observations of sea ice thickness, surface roughness and ice motion in Amundsen Gulf. *J. Geophys. Res. Oceans* 113. <https://doi.org/10.1029/2007JC004456>
- Petty, A.A., Tsamados, M.C., Kurtz, N.T., 2017. Atmospheric form drag coefficients over Arctic sea ice using remotely sensed ice topography data, spring 2009–2015.

- J. Geophys. Res. Earth Surf. 122, 1472–1490.
<https://doi.org/10.1002/2017JF004209>
- Pix4D, n.d. Step 1. Before Starting a Project > 4. Getting GCPs on the field or through other sources (optional but recommended) [WWW Document]. Support. URL <http://support.pix4d.com/hc/en-us/articles/202557489-Step-1-Before-Starting-a-Project-4-Getting-GCPs-on-the-field-or-through-other-sources-optional-but-recommended-> (accessed 7.12.18).
- Rango, A., Laliberte, A., Herrick, J.E., Winters, C., Havstad, K., Steele, C., Browning, D., 2009. Unmanned aerial vehicle-based remote sensing for rangeland assessment, monitoring, and management. *J. Appl. Remote Sens.* 3, 033542. <https://doi.org/10.1117/1.3216822>
- Rigor, I.G., Wallace, J.M., 2004. Variations in the age of Arctic sea-ice and summer sea-ice extent. *Geophys. Res. Lett.* 31. <https://doi.org/10.1029/2004GL019492>
- RINEX Working Group and RTCM-SC104, 2015. RINEX The Receiver Independent Exchange Format Version 3.03. [WWW Document]. URL <ftp://igs.org/pub/data/format/rinex303.pdf> (accessed 4.5.18).
- Rock, G., Ries, J.B., Udelhoven, T., 2012. Sensitivity analysis of UAV-photogrammetry for creating digital elevation models (DEM), in: *International Archives of the Photogrammetry, Remote Sensing and Spatial Information Sciences*. Presented at the International Conference on Unmanned Aerial Vehicle in Geomatics (UAV-g), Copernicus GmbH, Zurich, Switzerland, pp. 69–73. <https://doi.org/10.5194/isprsarchives-XXXVIII-1-C22-69-2011>
- Ryan, J.C., Hubbard, A.L., Box, J.E., Todd, J., Christoffersen, P., Carr, J.R., Holt, T.O., Snooke, N., 2015. UAV photogrammetry and structure from motion to assess calving dynamics at Store Glacier, a large outlet draining the Greenland ice sheet. *The Cryosphere* 9, 1–11. <https://doi.org/10.5194/tc-9-1-2015>
- Saiet, E., Dammann, D.O., Eicken, H., Mahoney, A.R., Rogers, M., Upton, C., 2015. Sea ice trafficability support using unmanned aircraft near Barrow, Alaska, in 6th Symposium on the impacts of an ice-diminishing Arctic on Naval and Maritime Operations, Washington DC, USA.
- Saiet, E., II, 2015. High-resolution sea ice topography mapping using UAS-based sensors and Structure-from-Motion techniques, in: *AGU Fall Meeting Abstracts*. Presented at the American Geophysical Union, Fall Meeting 2015, San Francisco, USA.
- SAR Aero, n.d. SAR Aero [WWW Document]. URL <http://saraero.com/about/> (accessed 7.11.18).
- Schön, S., Ingwer, P., Fischer, A., Schafföner, M., Hasche, E., Creutzburg, R., 2016. 3D reconstruction of buildings and landscapes – Evaluation of quality parameters and optimization of mission planning using RPAS, in: *Mobile Devices and Multimedia: Enabling Technologies, Algorithms, and Applications 2016*. Presented at the IS&T International Symposium on Electronic Imaging 2016, Electronic Imaging, San Francisco, pp. 1–9.
- Shi, S., Wang, L., Johnston, M., Rahman, A.U., Singh, G., Wang, Y., Chiang, P.Y., 2018. Pathway to a compact, fast, and low-cost LiDAR, in: *2018 4th International Conference on Control, Automation and Robotics (ICCAR)*. Presented at the 2018

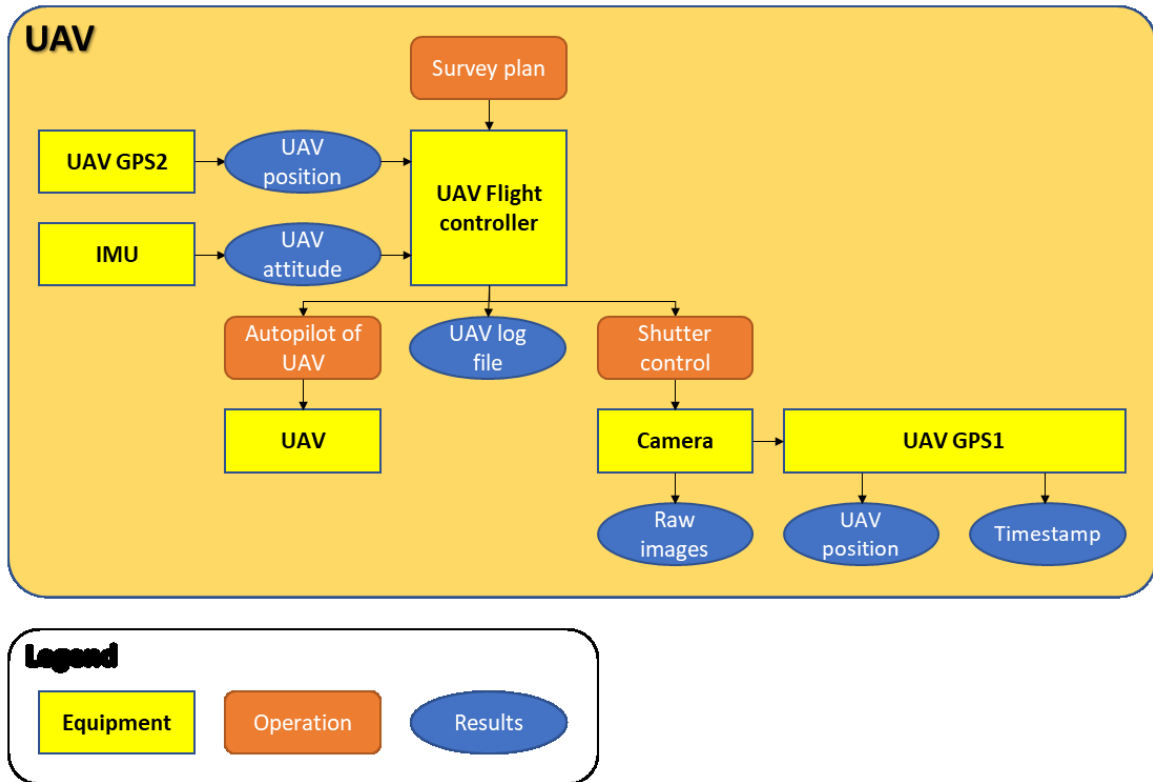
- 4th International Conference on Control, Automation and Robotics (ICCAR), pp. 232–236. <https://doi.org/10.1109/ICCAR.2018.8384676>
- Smith, M., Damià, V., 2015. From experimental plots to experimental landscapes: topography, erosion and deposition in sub-humid badlands from Structure-from-Motion photogrammetry. *Earth Surf. Process. Landf.* 40, 1656–1671. <https://doi.org/10.1002/esp.3747>
- Smith, M.W., Carrivick, J.L., Quincey, D.J., 2016. Structure from motion photogrammetry in physical geography. *Prog. Phys. Geogr.* 40, 247–275. <https://doi.org/10.1177/0309133315615805>
- Steer, A., 2017. Drifting sea ice and 3D photogrammetry. [WWW Document]. URL <https://www.spatialised.net/drifting-sea-ice-and-3d-photogrammetry/> (accessed 12.4.17)
- Steiner, N., Harder, M., Lemke, P., 1999. Sea-ice roughness and drag coefficients in a dynamic–thermodynamic sea-ice model for the Arctic. *Tellus Dyn. Meteorol. Oceanogr.* 51, 964–978. <https://doi.org/10.3402/tellusa.v51i5.14505>
- Strub-Klein, L., Sudom, D., 2012. A comprehensive analysis of the morphology of first-year sea ice ridges. *Cold Reg. Sci. Technol.* 82, 94–109. <https://doi.org/10.1016/j.coldregions.2012.05.014>
- Takasu, T., Yasuda, A., 2009. Development of the low-cost RTK-GPS receiver with an open source program package RTKLIB. Presented at the International Symposium on GPS/GNSS, Jeju, South Korea, p. 6.
- Tan, B., Wang, X., Wang, L., Peng, L., Li, Z., 2016. Statistical optimization with nonlinear constraints and parameter identification for the cutoff height of pressure ridges. *Comput. Appl. Math.* 35, 619–628. <https://doi.org/10.1007/s40314-014-0208-x>
- Taylor, J.R., 1997. An introduction to error analysis - The study of uncertainties in physical measurements, 2nd ed. University Science Books, California, USA.
- Thomson, L., Copland, L., 2016. White Glacier 2014, Axel Heiberg Island, Nunavut: mapped using Structure from Motion methods. *J. Maps* 12, 1063–1071. <https://doi.org/10.1080/17445647.2015.1124057>
- Thorndike, A.S., Rothrock, D.A., Maykut, G.A., Colony, R., 1975. The thickness distribution of sea ice. *J. Geophys. Res.* 80, 4501–4513. <https://doi.org/10.1029/JC080i033p04501>
- Tilly, N., Kelterbaum, D., Zeese, R., 2016. Geomorphological mapping with terrestrial laser scanning and UAV-based imaging. *Int. Arch. Photogramm. Remote Sens. Spat. Inf. Sci.* XLI-B5, 591–597. <https://doi.org/10.5194/isprs-archives-XLI-B5-591-2016>
- Transport Canada, 2018a. Getting permission to fly your drone [WWW Document]. URL <http://www.tc.gc.ca/en/services/aviation/drone-safety/getting-permission-fly-drone.html> (accessed 7.10.18).
- Transport Canada, 2018b. Applying for a Special Flight Operations Certificate [WWW Document]. URL <http://www.tc.gc.ca/en/services/aviation/drone-safety/getting->

- permission-fly-drone/applying-special-flight-operations-certificate.html (accessed 7.12.18).
- Transport Canada, 2018c. Proposed rules for drones in Canada [WWW Document]. URL <http://www.tc.gc.ca/en/services/aviation/drone-safety/proposed-rules-drones-canada.html> (accessed 7.12.18).
- Transport Canada, 2016. Exemption from Paragraph 571.08(1)(b) of the Canadian Aviation Regulations [WWW Document]. URL <http://www.tc.gc.ca/civilaviation/regserv/affairs/exemptions/docs/en/2879.htm> (accessed 3.26.17).
- Triggs, B., McLauchlan, P.F., Hartley, R.I., Fitzgibbon, A.W., 2000. Bundle adjustment — A modern synthesis, in: Triggs, B., Zisserman, A., Szeliski, R. (Eds.), *Vision Algorithms: Theory and Practice*. Springer Berlin Heidelberg, Berlin, Heidelberg, pp. 298–372. https://doi.org/10.1007/3-540-44480-7_21
- Tulldahl, H.M., Bissmarck, F., Larsson, H., Grönwall, C., Tolt, G., 2015. Accuracy evaluation of 3D lidar data from small UAV, in: *Electro-Optical Remote Sensing, Photonic Technologies, and Applications IX*. Presented at the Electro-Optical Remote Sensing, Photonic Technologies, and Applications IX, International Society for Optics and Photonics, p. 964903. <https://doi.org/10.1117/12.2194508>
- Turner, D., Lucieer, A., Wallace, L., 2014. Direct Georeferencing of Ultrahigh-Resolution UAV Imagery. *IEEE Trans. Geosci. Remote Sens.* 52, 2738–2745. <https://doi.org/10.1109/TGRS.2013.2265295>
- Uysal, M., Toprak, A.S., Polat, N., 2015. DEM generation with UAV photogrammetry and accuracy analysis in Sahitler Hill. *Measurement* 73, 539–543. <https://doi.org/10.1016/j.measurement.2015.06.010>
- van Diggelen, F., Enge, P., 2015. The world’s first GPS MOOC and worldwide laboratory using smartphones. Presented at the Proceedings of the 28th International Technical Meeting of The Satellite Division of the Institute of Navigation (ION GNSS+ 2015), Tampa Convention Center, Tampa, Florida, pp. 361–369.
- Vander Jagt, B., Lucieer, A., Wallace, L., Turner, D., Durand, M., 2015. Snow Depth Retrieval with UAS Using Photogrammetric Techniques. *Geosciences* 5, 264–285. <https://doi.org/10.3390/geosciences5030264>
- Velodyne LiDAR, 2016. How to Change the Laser Angle and FoV on a Velodyne VLP-16 – Velodyne LiDAR.
- Vihma, T., 2014. Effects of arctic sea ice decline on weather and climate: A review. *Surv. Geophys.* 35, 1175–1214. <https://doi.org/10.1007/s10712-014-9284-0>
- Weeks, W.F., 2010. *On Sea Ice*. University of Alaska Press, Fairbanks, Alaska, United States.
- Wernecke, A., Kaleschke, L., 2015. Lead detection in Arctic sea ice from CryoSat-2: quality assessment, lead area fraction and width distribution. *The Cryosphere* 9, 1955–1968. <https://doi.org/10.5194/tc-9-1955-2015>
- Westoby, M.J., Brasington, J., Glasser, N.F., Hambrey, M.J., Reynolds, J.M., 2012. ‘Structure-from-Motion’ photogrammetry: A low-cost, effective tool for

- geoscience applications. *Geomorphology* 179, 300–314.
<https://doi.org/10.1016/j.geomorph.2012.08.021>
- Williams, G., Maksym, T., Wilkinson, J., Kunz, C., Murphy, C., Kimball, P., Singh, H., 2015. Thick and deformed Antarctic sea ice mapped with autonomous underwater vehicles. *Nat. Geosci.* 8, 61–67. <https://doi.org/10.1038/ngeo2299>
- Worby, A.P., Griffin, P.W., Lytle, V.I., Massom, R.A., 1999. On the use of electromagnetic induction sounding to determine winter and spring sea ice thickness in the Antarctic. *Cold Reg. Sci. Technol.* 29, 49–58.
[https://doi.org/10.1016/S0165-232X\(99\)00003-8](https://doi.org/10.1016/S0165-232X(99)00003-8)
- Xin Miao, Hongjie Xie, Ackley, S.F., Songfeng Zheng, 2016. Object-based Arctic sea ice ridge detection from high-spatial-resolution imagery. *IEEE Geosci. Remote Sens. Lett.* 13, 787–791. <https://doi.org/10.1109/LGRS.2016.2544861>
- Yi, D., Harbeck, J.P., Manizade, S.S., Kurtz, N.T., Studinger, M., Hofton, M., 2015. Arctic Sea Ice Freeboard Retrieval With Waveform Characteristics for NASA's Airborne Topographic Mapper (ATM) and Land, Vegetation, and Ice Sensor (LVIS). *IEEE Trans. Geosci. Remote Sens.* 53, 1403–1410.
<https://doi.org/10.1109/TGRS.2014.2339737>
- Yigit, C.O., Gurlek, E., 2017. Experimental testing of high-rate GNSS precise point positioning (PPP) method for detecting dynamic vertical displacement response of engineering structures. *Geomat. Nat. Hazards Risk* 8, 893–904.
<https://doi.org/10.1080/19475705.2017.1284160>
- Zakharov, I., Bobby, P., Power, D., Warren, S., 2014. Monitoring extreme ice features using multi-resolution RADARSAT-2 data, in: 2014 IEEE Geoscience and Remote Sensing Symposium. Presented at the 2014 IEEE Geoscience and Remote Sensing Symposium, pp. 3972–3975.
<https://doi.org/10.1109/IGARSS.2014.6947355>
- Zell, H., 2017a. IceBridge Mission Overview [WWW Document]. NASA. URL http://www.nasa.gov/mission_pages/icebridge/mission/index.html (accessed 6.23.18).
- Zell, H., 2017b. Lasers - UTIG LiDARs [WWW Document]. NASA. URL http://www.nasa.gov/mission_pages/icebridge/instruments/utig-lidar.html (accessed 6.22.18).
- Zell, H., 2017c. Radar - Snow Radar [WWW Document]. NASA. URL http://www.nasa.gov/mission_pages/icebridge/instruments/snow.html (accessed 6.22.18).
- Zell, H., 2017d. Radars - Ku-Band Radar Altimeter [WWW Document]. NASA. URL http://www.nasa.gov/mission_pages/icebridge/instruments/kuband.html (accessed 6.22.18).
- Zwally, H.J., 2016. NASA: ICESat [WWW Document]. URL <https://icesat.gsfc.nasa.gov/icesat/index.php> (accessed 6.22.18).

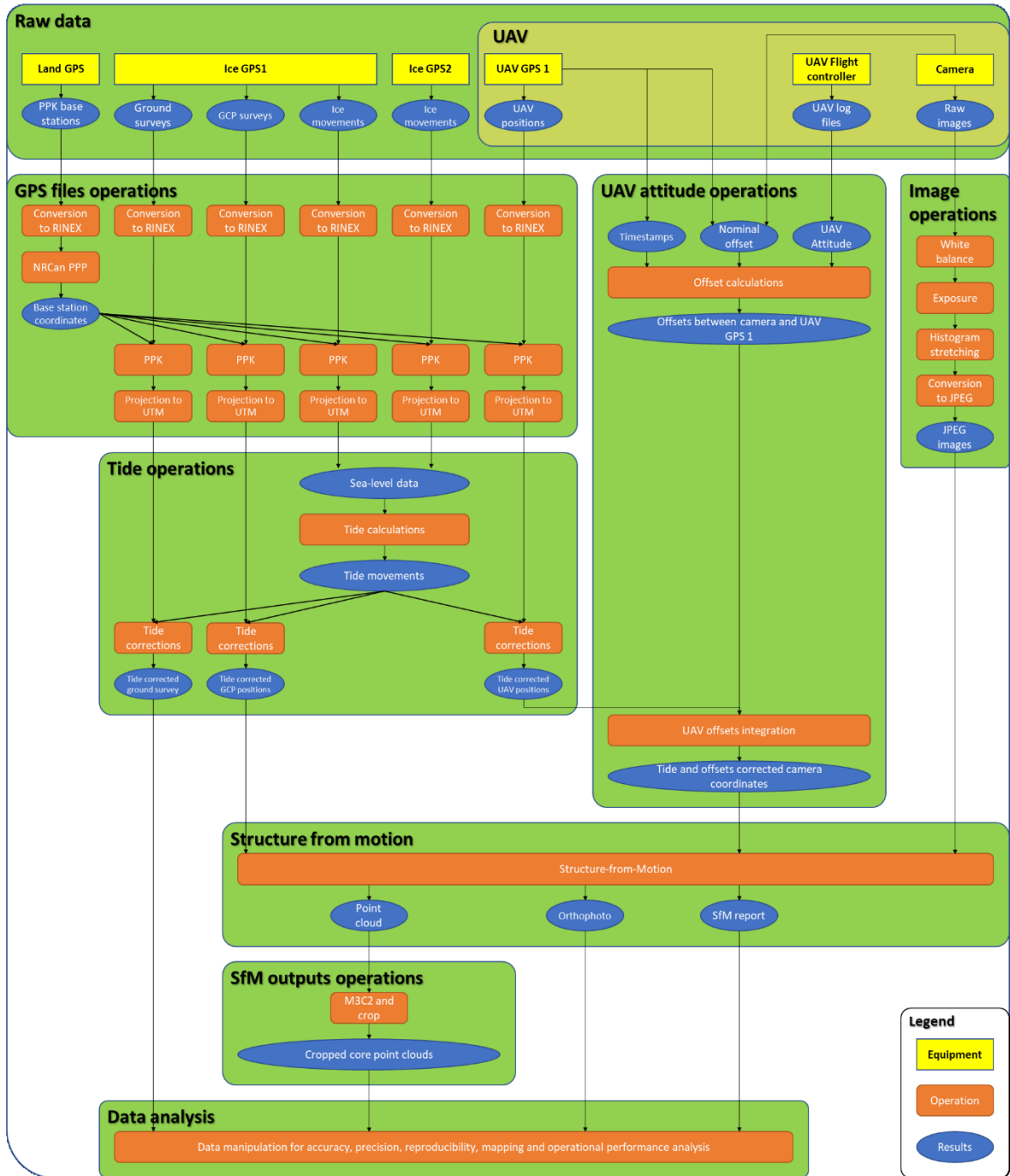
Appendix A. Workflow diagrams

A.1 UAV and payload: control and data workflow



This figure is a workflow schematic describing the functions of each major component of the UAV used to conduct the sUAV-SfM surveys, the relations between these components and the resulting data.

A.2 General data-processing workflow



This figure is a workflow schematic describing the steps of data preparation, SfM processing and post-processing operations for the SfM and ground surveys, from the data collection up to the generation of cropped core point clouds.

Appendix B. Custom R Script to correct UAV GPS1 positions

```
rm(list = ls(all=TRUE))# clean up

# Load libraries ####
#install.packages(c('sp','rgdal', 'tidyverse','lubridate','zoo','splines','KFAS')) #
uncomment and run once
library(sp)
library(rgdal)
library(tidyverse)
library(lubridate)
library(zoo)
library(KFAS)
library(splines)

# Setup ####

# Parameters and other process controls:
options(digits.secs=6) # enables milliseconds in times
zone=19 # UTM zone to use
tinterval = 0.001 # what time interval to interpolate to in s (for matching) --- MUST BE
0.001 !!

pdir = ('~/Dropbox/Research/martin/scripts') # working directory where the script and
metadata are found
metadata="Data_Dump_CSV.V03.csv"
datadir = "/tank/HOME/dmueller/Dropbox/Research/martin/PositionalData"
#datadir = "/tank/HOME/dmueller/ice/projects/Iqaluit2017/Analysis/PositionalData"
outdir = "/tank/HOME/dmueller/Dropbox/Research/martin/results"

# Custom functions ####

d2r = function(degree) {degree * pi/180} # convert degrees to radians
rd2 = function(radian) {radian * 180/pi} # convert radians to degrees

offset_corr = function(cam_off, roll, pitch, yaw) {
  #function rotates points about an origin and converts attitude into
  #cam_off is a vector of offsets in x,y,z
  #roll in degrees (left is neg)
  #pitch in degrees (fwd is neg)
  #yaw in degrees (clkw is pos)

  x1 = rep(cam_off[1], length(roll))
  y1 = cam_off[2]*cos(d2r(roll))+cam_off[3]*sin(d2r(roll))
  z1 = cam_off[2]*sin(d2r(roll))+cam_off[3]*cos(d2r(roll))

  x2 = x1*cos(d2r(pitch))-z1*sin(d2r(pitch))
  y2 = y1
  z2 = -x1*sin(d2r(pitch))+z1*cos(d2r(pitch))

  # calc x,y,z offset from origin
  easting_offset = x2*cos(d2r(yaw))-y2*sin(d2r(yaw))
  northing_offset = x2*sin(d2r(yaw))+y2*cos(d2r(yaw))
  alt_offset = z2

  return(list(easting_offset,northing_offset,alt_offset))
}

readpos = function(posfile, zone=19) {
  # reads an RTKLib pos file and returns a dataframe in a consistent format, with new
  data like utm E,N and dt
  # posfile: the full path to the pos file
  # zone: UTM zone
```

```

pos = read.table(posfile, header=FALSE, strip.white = TRUE, skip=26, stringsAsFactors =
FALSE)
col_names =
c('GPST','time','lat','lon','ht','Q','ns','sdn','sde','sdu','sdne','sdeu','sdun','age','r
atio')
names(pos) = col_names
dt = strptime(paste(pos$GPST,pos$time,sep="_"), '%Y/%m/%d_%H:%M:%OS',tz='GMT')
pos = pos[!(colnames(pos) %in% c("GPST", "time"))] # remove the old columns
pos = cbind(pos,dt)
pos = addutm(pos, zone=19)
return(pos)
}

addutm = function(df, zone=19) {
#take a data frame with lon/lat fields and convert data to utm (zone 19 is the default)
#append fields and return new dataframe
coords = cbind(df$lon, df$lat)
wpts=SpatialPoints(coords, proj4string=CRS('+proj=longlat +ellps=WGS84 +datum=WGS84
+no_defs'))
wpts = spTransform(wpts, CRS(paste0('+proj=utm +zone=',zone,' +ellps=WGS84 +datum=WGS84
+units=m +no_defs')))
utm_e = coordinates(wpts)[,1]
utm_n = coordinates(wpts)[,2]
return(cbind(df,utm_e,utm_n))
}

readlog = function(logfile, msg="gps") {
# reads a uav log file and returns a dataframe
# logfile: the full path to the log file
# msg: the name of the message - either "gps" (default), or "att"

uav_att = readLines(logfile)

if (msg == "gps") {
df = uav_att[grep('^GPS',uav_att)]
msgfields
=c('name','uav_usec','status','gps_msec','gps_week','nsat','hdop','lat','lon','alt','spd'
,'gcrs','vz','u')
}

if (msg == "att") {
df = uav_att[grep('^ATT',uav_att)]
msgfields
=c('name','uav_usec','desroll','roll','despitch','pitch','desyaw','yaw','err_rp','err_yaw'
')
}

df = do.call(rbind.data.frame, unname(sapply(df, function(x) strsplit(x, ', '))))
names(df) = msgfields
df = df[,-1] # remove 'name'
df = data.frame(apply(df, 2, function(x) as.numeric(as.character(x)))) # convert
factors to numeric

return(df)
}

uavgpstime = function(gpsdf) {
# takes a uav log gps data frame and adds a proper timestamp to it.
#convert gps_sec and gps week to UTC
#add gps_msec and att_usec to Jan 6, 1980
gpsT0=strptime("1980-01-06", "%Y-%m-%d", tz='GMT')
gpsT0 + weeks(gpsdf$gps_week[1]) + seconds(gpsdf$gps_msec[1]/1e3)
uavtime = gpsT0 + weeks(gpsdf$gps_week) + seconds(gpsdf$gps_msec/1e3)
return(cbind(gpsdf,uavtime))
}

uavatttime = function(gpsdf,attdf) {
#takes a uav log att data frame and adds a proper timestamp to it.

```

```

# also requires the uav log gps data frame that has a proper timestamp -- see
uavgpstime()

#calculate the mean of all time zeros this represents an offset to be applied to all
the att$uav_usec
uavT0 = mean(gpsdf$uavtime-seconds(gpsdf$uav_usec/1e6)) # take mean of (gps time -
event time)
hist(as.numeric(gpsdf$uavtime-seconds(gpsdf$uav_usec/1e6)-as.numeric(uavT0)),
xlab='Time difference (s)')
uavtime = attdf$uav_usec/1e6 + uavT0
return(cbind(attdf,uavtime))
}

spline_interp<-function(z,int){
# provide a zoo object (z) with variables to be interpolated
# provide a time interval (int) to be interpolated to (in seconds)
# note that it rounds to make a start and end time on the second
expanded.time = with(z,
seq(roundtime(time(z)[1],int),roundtime(time(z)[length(time(z))],int),by=int))
interp <- na.spline(z,xout=expanded.time, method = 'natural') # interpolate; result is
also a zoo object
names(interp) = names(z)
return(interp)
}

roundtime = function(t,int,tz='GMT') {
# will round a time (t) to the nearest interval (int) in seconds
# To round to nearest ms, int is 0.001
# need to specify the timezone (but defaults to GMT)

return( as.POSIXlt(round(as.double(t)*1/int)/(1/int),origin=(as.POSIXlt('1970-01-01',
tz=tz)), tz=tz) )
}

# Open the metadata list and start iterating through it---- #####
setwd(pdir)
#read csv file with the metadata
meta = read.csv(metadata)
# find all the surveys
surveys = meta$SurveyNum
for (s in surveys) { # this is the for loop that would run for each survey (s)

# UAV log operations #####
gpsmsg = readlog(file.path(datadir,meta$UAVLogFileName[s])) #Load the UAV log file - GPS
gpsmsg = addutm(uavgpstime(gpsmsg)) # get proper time stamp and utm data
attmsg = readlog(file.path(datadir,meta$UAVLogFileName[s]), msg='att') #Load the UAV log
file - ATT
attmsg = uavatttime(gpsmsg, attmsg) # get proper time stamp

# Calculate the camera position from offsets #####
offsets = offset_corr(c(meta$XOffset, meta$YOffset, meta$ZOffset), attmsg$roll,
attmsg$pitch, attmsg$yaw)
offsetz = zoo(cbind(offsets[[1]],offsets[[2]],offsets[[3]]), order.by=attmsg$uavtime)
names(offsetz) = c("off_x","off_y","off_z")

# Spline interpolation of the offset data #####
# natural spline - x,y,z wrt time
# this step may be replaced by Kalman filtering eventually
int_offsetz = spline_interp(offsetz,tinterval)

# plot to see the difference #####
par(mfrow=c(3,1))
plot(int_offsetz$off_x, col='red', xlab='Time', ylab='x-offset (m)')
points(int_offsetz$off_x,pch=20,cex=0.1)
plot(int_offsetz$off_y, col='red', xlab='Time', ylab='y-offset (m)')
points(int_offsetz$off_y,pch=20,cex=0.1)
plot(int_offsetz$off_z, col='red', xlab='Time', ylab='z-offset (m)')
points(int_offsetz$off_z,pch=20,cex=0.1)

```

```

par(mfrow=c(1,1))

# Spline the UAV gps data
gpsmsgz = zoo(cbind(gpsmsg$utm_e,gpsmsg$utm_n,gpsmsg$alt), order.by=gpsmsg$uavtime)
names(gpsmsgz) = c("utm_e","utm_n","alt")
int_gpsmsgz = spline_interp(gpsmsgz,tinterval)

# Ice base station ####
ibase_pos = readpos(file.path(datadir,meta$TopconIceFileName[s]))
ibase_pos$ht = ibase_pos$ht - meta$TopconIceDeviceHeight[s] # Get the sea-level height
ibasez = zoo(cbind(ibase_pos$utm_e,ibase_pos$utm_n,ibase_pos$ht), order.by=ibase_pos$dt)
names(ibasez) = c("utm_e","utm_n","alt")
ibasez = window(ibasez,start = time(int_offsetz)[1],
end=time(offsetz[length(time(offsetz))]) ) # this step saves time!
int_ibasez = spline_interp(ibasez,tinterval)

# Cut the data down to the same size
start_time = time(int_offsetz)[1]
if(time(int_offsetz)[1]-time(int_gpsmsgz)[1] < 0) {start_time = time(int_gpsmsgz)[1]}
if(time(int_gpsmsgz)[1]-time(int_ibasez)[1] < 0) {start_time = time(int_ibasez)[1]}

end_time = time(int_offsetz)[length(time(int_offsetz))]
if(time(int_offsetz)[length(time(int_offsetz))] -
time(int_gpsmsgz)[length(time(int_gpsmsgz))] > 0)
  {end_time = time(int_gpsmsgz)[length(time(int_gpsmsgz))]}
if(time(int_gpsmsgz)[length(time(int_gpsmsgz))] -
time(int_ibasez)[length(time(int_ibasez))] > 0)
  {end_time = time(int_ibasez)[length(time(int_ibasez))]}

int_offsetz = window(int_offsetz,start = start_time, end=end_time)
int_ibasez = window(int_ibasez,start = start_time, end=end_time)
int_gpsmsgz = window(int_gpsmsgz,start = start_time, end=end_time)

# test that all is well with the interpolation.
assertthat::are_equal(time(int_offsetz)[1], time(int_gpsmsgz)[1])
assertthat::are_equal(time(int_offsetz)[1], time(int_ibasez)[1])
assertthat::are_equal(length(time(int_offsetz)), length(time(int_gpsmsgz)) )
assertthat::are_equal(length(time(int_offsetz)), length(time(int_ibasez)) )

# Camera Events ####
cam_events = readpos(file.path(datadir,meta$ReachUAVEventsFileName[s]))

# Timestamp matching ####
# need to match as numeric - inflate by a factor of 1000 and round before comparing
event_ind = match( round(as.numeric(cam_events$dt)*1/tinterval),
round(as.numeric(time(int_offsetz))*1/tinterval) )
min(diff(event_ind)) < 0 # must be >>> 0

# Correction of data ###
# ibase data - remove changes related to sea ice
sd(int_ibasez$utm_e) # if these are small enough numbers, the correction can be ignored
sd(int_ibasez$utm_n)
sd(int_ibasez$alt)

# this sets the elevation to height above local sea level
coredata(int_gpsmsgz$alt) = coredata(int_gpsmsgz$alt) - coredata(int_ibasez$alt)
cam_events$ht = cam_events$ht - coredata(int_ibasez$alt[event_ind])

# this corrects the gps for offset to camera
cor_int_gpsmsgz = zoo(coredata(int_gpsmsgz) - coredata(int_offsetz),
order.by=time(int_gpsmsgz) )

x = int_gpsmsgz[,1] - int_offsetz[,1]
cor_cam_events = cam_events #copy
cor_cam_events$utm_e = cam_events$utm_e - int_offsetz[event_ind,1]
cor_cam_events$utm_n = cam_events$utm_n - int_offsetz[event_ind,2]
cor_cam_events$alt = cam_events$alt - int_offsetz[event_ind,3]

```

```

# Sea ice translation calculations?/drift and height correction

# Map ####
# this plot shows the raw UAV GPS data (red) vs the splined data (black)
plot(gpsmsgz$utm_e,gpsmsgz$utm_n, type='b',asp=1, col='red', xlab='Easting (m)',
ylab='Northing (m)')
lines(int_gpsmsgz$utm_e,int_gpsmsgz$utm_n, col='black')

#this plot shows the splined data (red), vs the camera offset (blue), vs the events
(black - taken from reach gps and red taken from event log),
plot(int_gpsmsgz$utm_e,int_gpsmsgz$utm_n, type='l',asp=1, col='red', xlab='Easting (m)',
ylab='Northing (m)')
lines(cor_int_gpsmsgz$utm_e, cor_int_gpsmsgz$utm_n, col='blue')
points(cor_int_gpsmsgz$utm_e[event_ind],cor_int_gpsmsgz$utm_n[event_ind],pch=20,cex=1,col
='black')
points(cor_cam_events$utm_e,cor_cam_events$utm_n,pch=1,cex=.5,col='red')

# Photo ####
photo_start =
as.numeric(strsplit(as.character(meta$FirstImgName[s]),split="DSC")[[1]][2])
photo_list = seq(photo_start, length.out=meta$PhotosNum[s] )
# this doesn't always match the event log.... !!

# Output ####

setwd(outdir)
write.csv(cor_int_gpsmsgz[event_ind],paste0("TriggerEvents_",sprintf("%02i", s),".csv"),
row.names=FALSE)

} # end for loop

```